COHERENT CONTROL OF ELECTRONIC AND VIBRATIONAL WAVE PACKETS USING PHASE-LOCKED OPTICAL PULSES

Elizabeth Durell Boléat

A thesis submitted for the degree of

Doctor of Philosophy

University College London

December 2004

ProQuest LLC
789 East Eisenhower Parkway
P.O. Box 1346
Ann Arbor, MI 48106-1346

For my father – David Paul Boléat

ACKNOWLEDGEMENTS

I would like to thank the following people:

Prof. Helen Fielding, for her enthusiastic, patient and encouraging supervision. I have learnt so much from Helen (*mostly* about science) and the opportunity to work in her lab is something I am very grateful for. The last few years have been challenging and thought-provoking, and are an experience that I wouldn't replace for anything.

Robert Carley, who started off as a lab partner, and rapidly turned into an excellent friend. I will never forget the many chamber dismantling, music downloading, sushi eating and "looking for the signal" hours we have spent in the lab. The oven cleaning incidents will hold a special place in my memory.

Russell Minns and Rakhee Patel, whose tireless efforts in the lab were so helpful in the completion of much of the experimental work presented here. They both provided amusing and uplifting diversions when things weren't working and useful discussions when all was well. I'd also like to thank the rest of the Fielding group, past and present, in particular John Heine, whose 4th year project initiated the Na work.

UCL chemistry's technical support group and workshop, who have got us out of a few fixes.

Peter Fekete, whose confidence in me and determination were instrumental in getting me to university in the first place.

My mother, June, for her never-ending support, and my brothers, Charles, Jonathon and Nicholas, who have provided amusement, encouragement and a dose of reality when needed.

ABSTRACT

Experimental and theoretical work is presented on the control of wave packet dynamics in atomic and molecular systems. Using sequences of phase-locked optical pulses, the link between optical phase and quantum mechanical phase is explored in the Na atom and Na_2^+ dimer, representing a step towards the logical engineering of quantum states in more complicated systems.

A novel apparatus, constructed to study and control the vibrational dynamics of vibrational wave packets on the Na_2^+ ionic potential surface, is described in chapter 3. Theoretical simulations for proposed experiment are presented in chapter 4. Control is achieved by exploiting the phase-evolution of the constituent vibrational quantum states within the wave packet superposition. The phase relationship and the accumulated phase difference between the various components of the wave packet is determined, and a sequence of phase-locked optical pulses is employed to selectively enhance or depopulate specific vibrational states, or sets of vibrational states. The quantum state composition of the resulting wave packet, and the efficiency of the control scheme, is determined by calculating the multi-pulse response of the time-dependent vibrational state populations.

In chapter 5, the quantum interference between Rydberg electron wave packets in the Na atom is investigated using pairs of phase-locked wave packets, allowing manipulation of the total orbital angular momentum of Na Rydberg atoms. Initially the wave packet is composed of a superposition of *s* and *d* Rydberg series. Exploitation of the difference between the quantum defects of the two series allows specific angular momentum compositions within the resultant wave packet to be engineered. Experimentally, this final quantum state distribution is analysed in the frequency domain using state selective field ionisation, and in the time domain using the optical Ramsey method. The theoretical calculations show how the phase difference between pairs of optical pulses is linked to the corresponding Rydberg frequency spectrum, therefore enabling the control of the quantum state composition of the wave packets.

THIS THESIS IS BASED ON THE FOLLOWING PUBLICATIONS

CHAPTER 4

Optical control of the quantum-state distribution of vibrational wave packets using trains of phase-locked pulses
E.D. Boléat and H.H. Fielding
Molecular Physics **103**, 491-499 (2005)

CHAPTER 5

Interfering Rydberg wave packets in Na
R.E. Carley, E.D. Boléat, R.S. Minns, R. Patel and H.H. Fielding
Journal of Physics B – Atomic, Molecular and Optical Physics, **38** 1907-1922 (2005)

Optical control of the quantum state distribution of Rydberg wave packets in Na and NO
E.D. Boléat, R.E. Carley, R.S. Minns, R. Patel and H.H. Fielding
CLF Annual Report, 151-2 (2004)

OTHER PUBLISHED WORK:

The dynamics of Rydberg electron wavepackets in NO
R.A.L. Smith, J.R.R. Verlet, E.D. Boléat, V.G. Stavros and H.H. Fielding
Faraday Discuss. **115**, 63-70 (2000)

CONTENTS

CHAPTER 1

COHERENT CONTROL – AN INTRODUCTION 1

1.1 Coherent control 2

1.2 Coherent control in the frequency domain 3
1.2.1 Multiple path interference control 3
1.2.2 STIRAP control 6

1.3 Coherent control in the time domain 8
1.3.1 Pump-probe and pump-dump methods 8
1.3.2 Wave packet manipulation 10
1.3.3 Optimal field control and learning algorithms 13

1.4 Conclusion 15

1.5 References 16

CHAPTER 2

WAVE PACKET DYNAMICS IN ATOMS AND MOLECULES 23

2.1 Dynamics of a two-level system 24

2.2 Wave packet evolution 27
2.2.1 The autocorrelation function 29
2.2.2 Time-dependence of wave packets 30
2.2.3 Revivals and partial revivals 31

2.3 Wave packet interference 40
2.3.1 Multiple pulse excitation 40
2.3.2 Ramsey fringes 41

2.3 Conclusion 46

2.4 References 46

CHAPTER 3

EXPERIMENTAL TECHNIQUES FOR THE CREATION, OBSERVATION AND CONTROL OF ELECTRONIC AND VIBRATIONAL WAVE PACKETS.....48

3.1 Introduction.....49

3.2 Lasers.....50
3.2.1 Time resolved experiments.....50
Wave packets in Na.....50
Wave packets in Na_2^+.....51

3.2.2 Frequency resolved experiments.....52
Frequency resolved spectra of Na.....53
Frequency resolved spectra of Na_2^+.....54

3.3 Ultrafast amplification.....56

3.4 Timing.....58

3.5 Vacuum apparatus.....60

3.6 The Sodium oven.....63

3.7 The stabilised interferometer.....66

3.8 Wave packet detection.....71
3.8.1 Optical Ramsey method (ORM).....71
3.8.2 State selective field ionisation (SSFI).....76
3.8.3 Proposed method for wave packet detection in Na_2^+.....81

3.9 Data collection and acquisition.....82

3.10 Summary.....83

3.11 References.....83

CHAPTER 4

OPTICAL CONTROL OF THE QUANTUM-STATE DISTRIBUTION OF VIBRATIONAL WAVE PACKETS IN Na_2^+ 86

4.1 Introduction 87

4.2 Dynamics of vibrational wave packets 90

4.3 Theory 94
4.3.1 Spectroscopy of Na_2 95
4.3.2 Vibrational wavefunctions and Franck-Condon factors 97
4.3.3 The control scheme 104

4.4 Results and discussion 105

4.5 Conclusion 115

4.6 References 115

CHAPTER 5

OPTICAL CONTROL OF ORBITAL ANGULAR MOMENTUM IN Na 120

5.1 Introduction 121

5.2 Dynamics of Rydberg electron wave packets 123

5.3 Spectroscopy of Na 126
5.3.1 The quantum defect 126
5.3.2 Energy levels and oscillator strengths 127

5.4 The control scheme 130

5.5 The quantum defect and wave packet dynamics 133

5.6 Experimental details 136

5.7 Results 138
5.7.1 Na frequency spectra 138
5.7.2 Wave packets in Na 139
5.7.3 Wave packets separated by T_{cl} 143
5.7.4 Wave packets separated by $3T_{cl}/2$ 148

5.8 Conclusion 154

5.9 References 155

CHAPTER 6

CONCLUSION AND OUTLOOK 158

6.1 Dynamics of vibrational wave packets in Na_2^+ 159

6.2 Dynamics of electronic wave packets in Na 162

APPENDIX 1

(a) Fortran 90 code for calculation of vibrational and rotational energy levels, transition energies and rotational energy distributions in Na_2 (chapter 4).

(b) Fortran 77 code for calculation of the autocorrelation function for vibrational wave packets, the population distribution of vibrational states within the wave packet and the radial distribution function. Additional subroutines are available for calculation of the populations as a function of time, and the phase-shift required to depopulate the central state in a vibrational wave packet (chapter 4).

(c) Fortran 77 code for calculation of the energy levels in Na and relevant transition energies and corresponding oscillator strengths. Additional subroutines are available to calculate the autocorrelation function for Rydberg electron wave packets, and the population distribution of the *s* and *d* states within the wave packet (chapter 5).

APPENDIX 2

Derivation of equation (2.9) (Chapter 2, p26)

APPENDIX 3

Integration of equation (2.11) (Chapter 2, p26)

APPENDIX 4

Derivation of equations (2.17) and (2.18) (Chapter 2, p.30-31)

APPENDIX 5

Expansion of the E_n around $\bar{n}$ for Rydberg states in a wave packet

(Chapter 2, p.31)

FIGURES

CHAPTER 1

COHERENT CONTROL – AN INTRODUCTION

Figure 1.1	Schematic diagram illustrating the Brumer-Shapiro coherent control scheme.	4
Figure 1.2	Three-level excitation scheme employed in the STIRAP technique.	7
Figure 1.3	Schematic energy level diagram illustrating one method of time-domain coherent control in sodium.	9

CHAPTER 2

WAVE PACKET DYNAMICS IN ATOMS AND MOLECULES

Figure 2.1	Calculated recurrence spectrum of a vibrational wave packet excited around the $v = 9$ vibrational level of the $X^+\ ^2\Sigma_g^+$ state of Na_2^+, with a 30 fs bandwidth limited laser pulse.	36
Figure 2.2	Calculated recurrence spectrum of an electron wave packet in H, excited around n = 40 with a 1 ps, bandwidth limited laser pulse.	38
Figure 2.3	Time dependent probability distribution of a radial electron wave packet excited around n = 40 in H, with a 1 ps, bandwidth limited laser pulse.	39
Figure 2.4	A plot showing the total population of hydrogen Rydberg states after excitation by a sequence of two, identical one-picosecond pulses	42
Figure 2.5	A set spectral profiles obtained from Fourier transforming a pair of bandwidth limited, optical pulses separated by various delays from 0 to $3T_{cl}/2$.	45

CHAPTER 3

EXPERIMENTAL TECHNIQUES FOR THE CREATION, OBSERVATION AND CONTROL OF ELECTRONIC AND VIBRATIONAL WAVE PACKETS

Figure 3.1	Two-photon excitation schemes for excitation and control of (a) Rydberg electron wave packets in Na and (b), vibrational wave packets in Na_2^+.	49
Figure 3.2	A schematic diagram of the laser set-up used excite wave packets in Na	55
Figure 3.3	End-on view of a Bethune cell.	57
Figure 3.4	Schematic diagram detailing the timing triggers for the Na wave packet experiments.	59
Figure 3.5	Vacuum apparatus set-up for experiments in Na and Na_2.	62
Figure 3.6	Cross-section through the sodium oven.	64
Figure 3.7	Graph (a) is a plot of the voltage obtained from heating a double thermocouple (with one end in iced water at 0°C) verses the voltage obtained from heating a single thermocouple (the oven thermocouple). Graph (b) is a plot of tabulated thermocouple data.	66
Figure 3.8	Schematic diagram of a single Michelson interferometer used to create a pulse pair with a well-defined phase difference.	67
Figure 3.9	Layout of the double interferometer is used in the coherent control experiments.	69
Figure 3.10	In (a), a sample of the raw data collected in a typical wave packet experiment is presented. 4 fringes, collected over 40 piezo steps is presented in (b), and (c) is the recurrence spectrum obtained from fitting a sine wave to the raw data in (a).	73
Figure 3.11	Optical Ramsey fringes in the region of $t = 0$ for an electron wave packet excited around n =35 in the sodium atom.	75

Figure 3.12	Schematic diagram showing the Coulombic potential of an electron in (a) the absence of a field and (b) in the presence of a field along the z -axis.	77
Figure 3.13	Schematic diagram showing how modifications were made to the high voltage pulser, to increase the rise time of the pulse to around 2.3 μs. The modifications were necessary in order to carry out SSFI on electron wave packets in Na.	79
Figure 3.14	Raw data from a typical SSFI experiment in Na.	80

CHAPTER 4

OPTICAL CONTROL OF THE QUANTUM-STATE DISTRIBUTION OF VIBRATIONAL PACKETS IN Na_2^+

Figure 4.1	Schematic representation of the two-photon excitation scheme, used in the coherent control calculations in Na_2.	95
Figure 4.2	Vibrational wavefunctions and probability density distributions of the Na_2^+ potential curve, for $v = 0 - 5$ and $v = 10$.	100
Figure 4.3	Franck Condon factors for the $A\,^1\Sigma_u^+(v' = 0-20) \leftarrow X\,^1\Sigma_u^+(v'' = 0)$ transitions in Na_2.	101
Figure 4.4	Franck Condon factors for the Na_2^+ $X^+\,^1\Sigma_g^+(v = 0-20) \leftarrow$ Na $A\,^1\Sigma_u^+(v' = 0-20)$ transitions.	102
Figure 4.5	Vibrational wavefunctions and Franck-Condon factors for the Na_2^+ $X^+(v = 0-10) \leftarrow$ Na $A(v' = 1)$ and Na_2^+ $X^+(v = 5-15) \leftarrow$ Na $A(v' = 9)$ transitions.	103
Figure 4.6	Calculated wave packet recurrence spectrum and corresponding population distributions of a single wave packet excited around $v = 5$ in the $X^+\,^2\Sigma_g^+$ state of Na_2^+.	106

Figure 4.7 Calculated vibrational state population distributions, following excitation with a pair of 40 fs bandwidth limited optical pulses centred around $v = 5$ in the $X^+\ ^2\Sigma_g^+$ state of Na_2^+. Plots (a) – (e) represent varying delays between the two pulses. 108

Figure 4.8 Plot showing the rate of phase accumulation of the $v = 4, 5$ and 6 vibrational states in the $X^+\ ^2\Sigma_g^+$ state of Na_2^+ (crosses, white circles and black circles respectively), after one vibrational period. 111

Figure 4.9 Calculated wave packet recurrence spectra and corresponding population distributions following excitation with a 40 fs bandwidth limited pulse, of a single wave packet (a) and two wave packets separated by $T_{cl}/2$ (b) and (c). 112

Figure 4.10 Cartoon of a control scheme illustrating how the relative populations of individual states in a wave packet, excited around $v = 9$ in the $X^+\ ^2\Sigma_g^+$ state of Na_2^+, can be manipulated. 113

Figure 4.11 Calculated wave packet recurrence spectra following excitation of a single wave packet centred around $v = 9$ (a), and a sequence of 5 phase-locked wave packets (b). 114

CHAPTER 5

OPTICAL CONTROL OF ORBITAL ANGULAR MOMENTUM IN Na

Figure 5.1 Schematic representation illustrating the excitation scheme in Na. The first excitation is from $^1S_{1/2}$ state to the $^2P_{3/2}$ state. A wave packet is created from a superposition of *s* and *d* Rydberg states. 128

Figure 5.2 Calculated recurrence spectra for a wave packet excited around $n = 35$ in Na. The upper and lower traces represent the same wave packet, but the lower is deconvoluted into its *s* and *d* components. 129

Figure 5.3	Calculated wave packet recurrence spectra of a set of theoretical wave packets. Plot (a) is a single series wave packet presented for reference. Plots (b) – (d) are recurrence spectra of wave packets consisting of two series, with the same intensities, but with quantum defect differences between the series of $\Delta\mu = 1/2,\ 1/4$ and $1/3$ respectively.	135
Figure 5.4	Frequency spectrum of Na over the region of n = 24 to the ionisation limit. The positions of the s and d Rydberg series are also plotted. Note: the x-axis is plotted as transition energy in wavenumbers, not the absolute energies of the Rydberg states.	138
Figure 5.5	Frequency spectrum of Na Rydberg states illustrating the region of the spectrum where the wave packet control experiments take place, overlaid with a Gaussian distribution corresponding to a 0.7 ps laser pulse.	139
Figure 5.6	Experimental and calculated wave packet recurrence spectra in Na for wave packets excited around (a) $n = 25$ and (b) $n = 28$, with a 0.7 ps laser pulse.	140
Figure 5.7	Experimental and calculated recurrence spectra of a wave packet excited around $n = 35$ in Na, illustrating a second, third and fourth order partial revival.	141
Figure 5.8	Plot (a): calculated and experimental recurrence spectrum of a wave packet excited around $n = 31$ in Na, overlaid with a cosine wave with period $t_\mu = 12.9$ ps. Plot (b) is a higher resolution portion of the same spectrum, over the region of the full revival. Plot (c) is a calculated population distribution of the *s* and *d* states within the wave packet. As before, the black and white bars represent the *s* and *d* components respectively.	142
Figure 5.9	Plot showing the trend in classical orbit period as the average energy (in terms of principal quantum number) increases. The circles represent experimentally determined orbit periods and the solid line represents the calculated trend.	143

Figure 5.10 Calculated (b) and experimental (c) SSFI traces illustrating the phase evolution of individual *s* and *d* Rydberg states in a wave packet excited around $n = 35$ by a 0.7 ps bandwidth limited laser pulse. The excitation was made with a pair of phase-locked pulses separated by $t = T_{cl} + t_\phi$. The individual Rydberg states which make up the wave packet are shown in (a). 145

Figure 5.11 SSFI data representing the population distributions of the $34d$ and $35s$ Rydberg states in a Na wave packet after excitation with a pair of phase-locked pulses separated by $t = T_{cl} + t_\phi$. A calculated plot showing the population vs. phase evolution is plotted on the left hand side of the figure. 146

Figure 5.12 Calculated population distributions for the *s* and *d* states in a wave packet in Na, created around $n = 35$ with a pair of 0.7 ps, phase-locked laser pulses. Plots (a) – (d) differ in the amount of time the pulses are separated. In all cases, the second laser pulse is delayed by a time $t = T_{cl} + t_\phi$, where ϕ = (a) 0, (b) π, (c) 0.7π, and (d) -0.3π. 147

Figure 5.13 Cartoon plot illustrating the phase differences that arise at the second order partial revival, when two wave packets in Na are excited with a pair of phase-locked pulses separated by $3T_{cl}/2$. At the second order partial revival, both wave packets have split into two, each $\pi/2$ out of phase with the other. 150

Figure 5.14 Cartoon plot illustrating the distribution the *s* and *d* states in a wave packet after excitation of a pair of phase-locked pulses separated by $t = 3T_{cl}/2 + t_\phi$, where $\phi = \pm\pi/2$. 151

Figure 5.15 Experimental (a) and calculated (b) recurrence spectra for a wave packet excited around $n = 35$ in Na with a pair of 0.7 ps phase-locked laser pulses, separated by $t = 3T_{cl}/2 + t_\phi$. The population distributions of the *s* and *d* states in each wave packet are present in (c) 153

CHAPTER 6

CONCLUSION AND OUTLOOK

Figure 6.1	Experimental spectrum of the $A^1\Sigma_u^+ \leftarrow X^1\Sigma_g^+$ transition in Na_2 recorded by 1+2 resonance-enhanced multiphoton ionisation (REMPI) , and calculated line positions showing the intensity profile assuming molecular beam temperatures of 20 K, 50 K and 80 K.	159
Figure 6.2	New arrangement of the oven in the vacuum chamber, illustrating how the top-hat flange replaces the central flange of the chamber.	160

CHAPTER 1:

COHERENT CONTROL – AN INTRODUCTION

The experimental and theoretical work presented in this thesis are examples of coherent control – the process by which the outcome of a chemical reaction is controlled by the application and manipulation of optical fields. To provide a context to the work presented in later chapters, this introduction discusses the techniques employed for coherent control in the frequency and time domains. Emphasis is placed on the time-domain approach of wave packet interferometry and the various techniques within this field are reviewed. Recent experiments involving wave packet control are discussed in detail.

1.1 COHERENT CONTROL

The term *coherent control* describes optical methods in which quantum interference effects are used to control atomic and molecular processes. There are two motivating factors behind the interest in coherent control: first, to create a particular product or state that is unattainable by chemical means and second, to achieve a superior fundamental understanding of atoms and molecules and their interactions with light. One of the most fundamental laws of physics, the wave-particle duality of light and matter, is responsible for all coherent control processes. The fact that the dynamics of electrons, atoms and molecules can be described in terms of wave motion, and can therefore can undergo interference with light, is at the heart of coherent control.

The earliest example of manipulating the phase of light was Young's double slit experiment in 1801 [1]. In this setup, a monochromatic plane wave is incident on two closely spaced slits in a screen. From each slit, a new spherical wave emerges and travels to an observation screen a distance away that is large compared to the space between the slits. Each spherical wave has a fixed phase relation to the incident light wave and therefore, to each other wave emitted from the slit. The observation screen shows an alternating pattern of bright and dark fringes, dependent upon whether the two waves are in or out of phase with one another. Mathematically, the intensity at any point of the screen is proportional to the square of the total electric field **E** at that point, so that $|\mathbf{E}_1 + \mathbf{E}_2|^2 = |\mathbf{E}_1|^2 + |\mathbf{E}_2|^2 + 2|\mathbf{E}_1||\mathbf{E}_2|\cos\phi$, where ϕ is the phase difference. Control of ϕ governs the intensity at any point.

The matter equivalent to Young's two-slit experiment arises when an initial atomic or molecular state can follow two distinct paths, characterised by wave functions Ψ_1 and Ψ_2, to a final state. The probability of being in the final state is proportional to the square of the total wavefunction. The wavefunction amplitudes must be summed before squaring, and the probability of the process contains a cross term involving the phase of the two wavefunctions. It follows that by altering the relative phases of a set of competing paths, it is possible to control the total probability of the transition. The tool

that permits practical exploitation of quantum interference for control of molecular dynamics is the laser. Laser technology now permits the generation of very short pulses of light, shaped pulses, pulses with a well-defined phase relationship, very pure monochromatic light fields, and very high intensity light fields. The possibility that matter may be manipulated using the intrinsic interference effects that occur on interaction with a light field led to the idea of coherent control, and the use of light as the control tool. In the late 1980s, three distinct methods for coherent control were discussed. Two of the approaches focused on control in the frequency domain and one, on control in the time domain. Although these techniques are distinct in their methods of control, it is now appreciated that, when considering the general mechanism of light-controlled quantum interference, they are equivalent. The methods differ due to the vastly diverging approaches to the problem and are discussed separately in the following section. The objective of this chapter is to illustrate how diverse the field of coherent control has become, and to show how the distinct mechanisms of each control scheme achieve their goal of coherent control.

1.2 COHERENT CONTROL IN THE FREQUENCY DOMAIN

1.2.1 MULTIPLE PATH INTERFERENCE CONTROL

In 1986, Brumer and Shapiro proposed the first coherent control scheme by exploiting the interference between two possible reaction pathways to a set of target states [2,3]. The general goal behind this phase-control method was to use two narrow bandwidth pulses to provide two or more excitation pathways from the initial to final states of an atom or molecule, and to use the interference between them as a control parameter. In this way, control of the excited state population is obtained by varying the relative phase of the two fields to modulate the interference pattern of the product wavefunctions. From the target states, various processes such as ionization or dissociation can occur by subsequent absorption of a photon. As illustrated in figure 1.1, the competing pathways

to the final level are a product of excitation by m photons of frequency ω_m and n photons of frequency ω_n, so that $E_{mn} = m\hbar\omega_m = n\hbar\omega_n$. In this scheme, control of the phase difference between the two sets of frequencies is achieved by creating the higher frequency photons from the lower frequency ones by harmonic generation in a non-linear optical medium. The usual choices of m and n are "1 and 3" and "1 and 2".

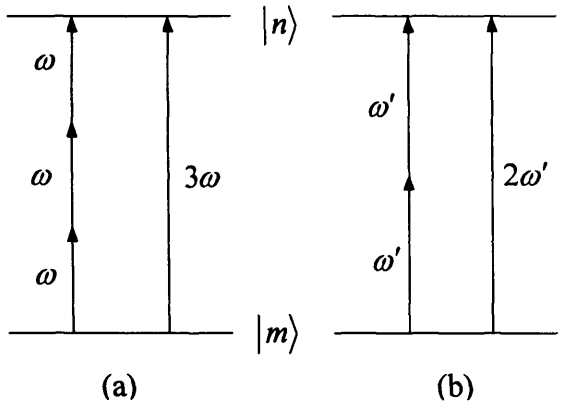

Figure 1.1 Schematic diagram representing the Brumer and Shapiro coherent control scheme for (a) (1+3) photon excitation and (b) (1+2) photon excitation between levels $|m\rangle$ and $|n\rangle$.

The most widely used scheme employing the Brumer-Shapiro method of coherent control is the (1+3), or $(\omega + 3\omega)$, excitation [4]. In this method the interference between a dipole-allowed three-photon transition induced by laser radiation (frequency ω) and a one-photon transition induced by its third harmonic (3ω), is used to control the relative excited state population arising from the two competing pathways. This approach was successfully demonstrated first by Chen *et al.* [5] for atoms, and Park *et al.* [6] for molecules. The two light fields couple the initial and several energetically degenerate final states at an energy separation of $3\hbar\omega$. The probability amplitudes of the two reaction pathways are controlled by varying the relative phase $\Delta\phi = \phi_\omega - \phi_{3\omega}$ between the two light sources. The $\omega + \omega_3$ scheme has since been successfully used to ionise atoms [5,7-9], diatomic molecules [10-12] and polyatomic molecules [13-15]. This scheme has further achieved control of the branching ratio in a number of

photodissociation reactions [12,16,17]. A particularly clear example of the $\omega + \omega_3$ scheme was demonstrated in 1991 by Gordon *et al.* with an experiment controlling autoionisation versus predissociation in HI and DI molecules [18,19]. In their experiment, a beam of DI molecules was excited with one photon of 117.90 nm and three photons of 353.69 nm. The excited molecules decayed either by autoionisation to produce DI^+ or by predissociation to produce a ground state D atom and an electronically excited I atom, which subsequently absorbed additional photons to produce I^+. As the phase between the two laser beams was increased from 0 to 2π, the ion signals varied sinusoidally. It was appreciated that by varying the phase difference between the two laser beams, one could control the ratio of I^+ to D^+ and when this phase difference was equal to π, maximum contrast between the two interfering pathways was achieved. The key to this experiment was the observation of a constant phase difference, known as the phase lag, that offset the two oscillatory signals. It is known that the value of the phase lag depends on the detuning of the incident beam with respect to a particular resonance, but there is no trivial explanation of the origin of this phase lag. Attempts to provide an intuitive picture of this process are often misleading and are currently still in the domain of numerical calculations [20-22]. However, there has been a great deal of interest in the applications of the phase lag and Gordon *et al.* [23] have demonstrated that phase-lag spectroscopy is a sensitive technique for studying the properties of molecular continua.

An alternative use of the Brumer-Shapiro scheme exploits the interference effects between a one-photon transition induced by second harmonic light and two-photon transition induced by fundamental light (the $\omega + \omega_2$ scheme). In this method the final states differ in their parity due to the different selection rules governing one- and two-photon transitions. Consequently the interference between the two transitions can only be observed in the photofragment angular distributions [24]. This scheme has been applied to photoelectrons in the ionisation of atoms [25], molecular photodissociation [26-28] and above threshold ionisation [29-31].

The majority of calculations performed using the Brumer-Shapiro method show nearly 100% efficiency of population transfer. This efficiency is however, not realised experimentally. For example, in the case of the DI experiment, the depth of the population modulation was found to be only approximately 20%. To experimentally implement the Brumer-Shapiro method, narrow bandwidth excitation (long pulses or CW beams) is needed to provide two or more excitation pathways from the initial to final states. Although control has been demonstrated in a variety of systems, clearly showing that interference is a core process in achieving coherent control, the corresponding theoretical predictions need to be extended to take into account all relevant quantum states of the system and the various degrees of freedom, in order to more accurately determine what is experimentally attainable.

1.2.2 STIRAP CONTROL

As mentioned in section 1.1, one of the major goals of coherent control is to achieve 100% transfer of population between specified quantum states. In a two-level system, Rabi oscillations induced by the light field, cycle population between the initial and final states at the optical frequency (discussed in more detail in chapter 2). With radio frequency π pulses, routinely generated in NMR, it is possible to achieve 100% population transfer. However, difficulties arise in optical and UV spectroscopy [32]. In the visible and ultraviolet range, where the majority of molecular transitions occur, the fast Rabi oscillations prevent 100% excitation and restrict the transferred population to about 50% per Rabi period resulting in a highly congested or broadened spectrum. For multiple pulse experiments, if each laser pulse can only achieve 50% population transfer, then after two pulses, one can only expect a 25% yield. This limitation was overcome with an adiabatic technique involving the coherent interaction between two laser pulses and a three level system. It is essentially an extension of the Brumer-Shapiro approach but rather than using two pathways that lead to the same final states, this method uses a single route from the initial to the target states, along with an

additional field that is used to couple the target states to a previously unoccupied state. This frequency domain method, a stimulated transition induced by Raman adiabatic passage (STIRAP), depends on a Raman-type transition stimulated by a pair of pulses [33]. The goal is to transfer as much population as possible from level $|1\rangle$ to level $|3\rangle$ (see figure 1.2). The "pump" laser couples initial state $|1\rangle$ to intermediate state $|2\rangle$, whilst the "Stokes" laser couples $|2\rangle$ to final state $|3\rangle$. The initial and final states must be long-lived, whereas the intermediate state will undergo spontaneous emission, not only to states $|1\rangle$ and $|3\rangle$, but also to other states. The objective is to transfer all of the population from $|1\rangle$ to $|3\rangle$, without any loss from state $|2\rangle$, essentially minimising the population in $|2\rangle$ throughout the experiment. Although coupling is strongest when the two laser pulses are tuned to their respective resonant frequencies, in this technique, it is only necessary for the *combination* of pump and Stokes frequencies be resonant with the two-photon Raman transition. This is achieved with a counterintuitive pulse sequence, in which the Stokes laser precedes, but overlaps, the pump laser. In essence, the presence of both fields directly couples the ground state and the final state adiabatically.

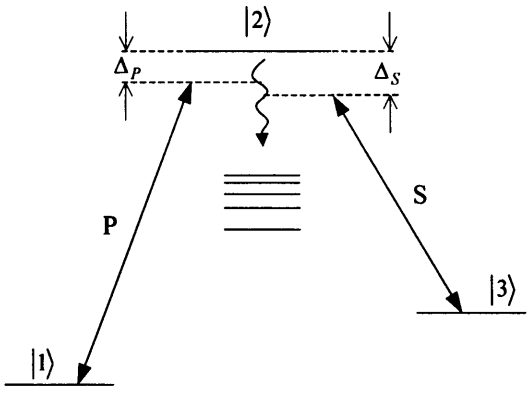

Figure 1.2 Three level excitation scheme employed in STIRAP. The initially populated state $|1\rangle$ and the final state $|3\rangle$ are coupled by the Stokes laser S and the pump laser P via an intermediate state $|2\rangle$. The intermediate state may decay to other levels by spontaneous emission. Δ_P and Δ_S are the detuning of the pump and Stokes laser frequencies from the transition frequency.

This scheme has been used to achieve population transfer with various rates of efficiency in atoms, diatomic and polyatomic molecules [34-40]. More recently, an extension of the STIRAP method has been introduced, in which the pump and stokes laser pulses are replaced by a single chirped pulse. In this method, also known as CHIRAP, the higher frequencies arrive before the lower ones, achieving the STIRAP effect with a single laser pulse [41-43]. It appears that the STIRAP concept is very powerful, its only limitation being the requirement of sharp resonances in the sample to be controlled – an obvious drawback when one considers extensions to more complex systems.

1.3 COHERENT CONTROL IN THE TIME DOMAIN

1.3.1 PUMP-PROBE AND PUMP-DUMP METHODS

In 1980, Zewail proposed that the control of chemical reactions by selective bond excitation would require the use of short laser pulses, to compete with intramolecular vibrational energy redistribution [44]. Short pulse excitation leads to the formation of wave packets, coherent superpositions of energy eigenstates, whose motion can remain relatively localised for as long as picoseconds (in the gas phase). The excitation of wave packets and their subsequent evolution is discussed in detail in chapter 2. Zewail *et al.* went on to exploit this localisation for probing chemical reaction dynamics [45-49], the so-called 'pump-probe' technique. At approximately the same time, the concept of pump-dump was formulated by Tannor, Kosloff and Rice [50,51]. Their calculations showed that it was possible to control the relative yields of products in a branching chemical reaction using short light pulses by varying the interval between an initial "pump" pulse of radiation that transfers amplitude from the ground state to an excited state, and a later "dump" pulse that transfers the amplitude in the opposite direction.

Experimental demonstrations of this time-domain control scheme are found in many pump-probe time-resolved experiments. Whilst many pump-probe and pump-

dump techniques use the time-dependent motion of a wave packet to control the dynamics of the system, only a few examples actually use the time-delay between the pump and probe/dump pulse for control. A classic experimental demonstration involved the work of Baumert and Gerber [52,53], who used a pair of femtosecond laser pulses to produce either Na^+ or Na_2^+ as a function of the time delay between pump and probe pulses. The excitation schemes and competing processes are illustrated in figure 1.3.

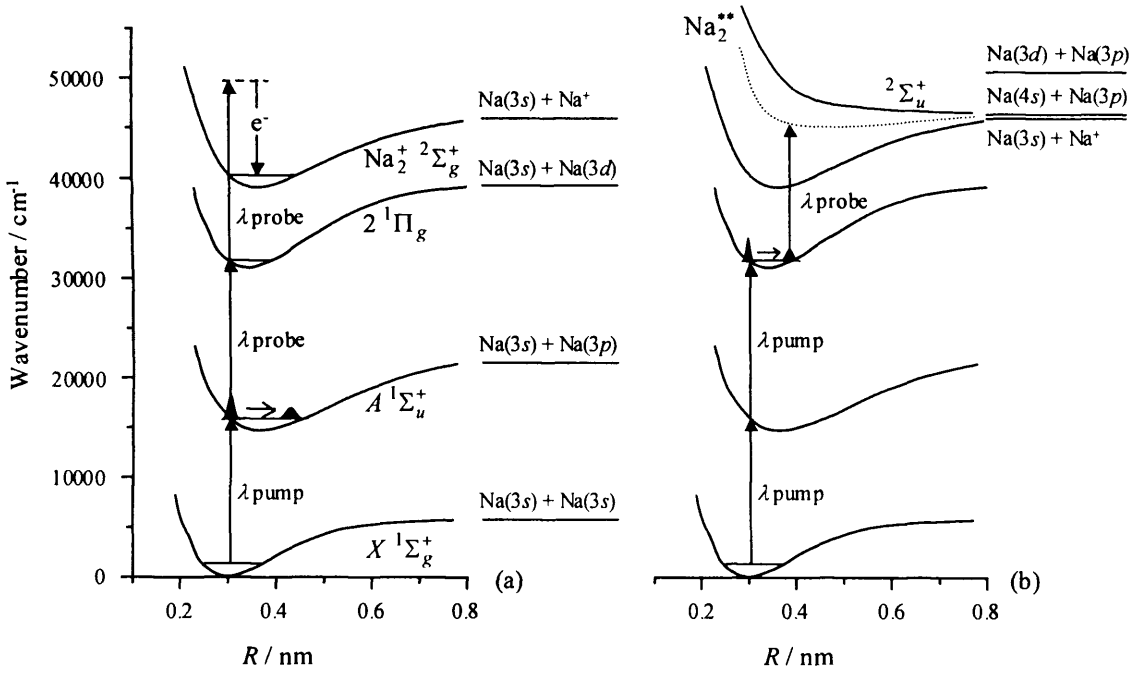

Figure 1.3 Schematic energy level diagram illustrating how coherent control of the Na^+ / Na_2^+ ratio is achieved. In process (a), a wave packet is prepared in the A-state of Na_2 at the inner turning point, from where a two-photon probe process transfers the wave packet into the ionization continuum via the $2\,^1\Pi_g$ state. In process (b), two pump photons prepare a wave packet in the $2\,^1\Pi_g$, leading to excitation of Na_2^{**}.

In the first reaction channel, a single pump photon excites a vibrational wave packet in the $A\ ^1\Sigma_u^+$ state of Na_2. At the inner turning point, the wave packet absorbs two probe photons resulting in ionisation into the ionic ground state $^2\Sigma_g^+$ and the production of Na_2^+ ions. In the competing process, two pump photons prepare a vibrational wave packet in the $^1\Pi_g$ state where it absorbs a single probe photon at the

outer turning point. This probe photon excites the wave packet to a bound, doubly excited autoionising Na_2^{**} state where dissociation occurs to form Na(3s) + Na^+. The ratio of molecular to atomic ion products was found to oscillate with the delay between the laser pulses, with a period determined by the motion of the wave packet.

1.3.2 WAVE PACKET MANIPULATION

In a pump-probe experiment, when the pump and probe beams are of different wavelengths with no spectral overlap, the relative phase between the pump and probe pulses plays no role in the control process. However, if the two laser beams have the same wavelength and hence overlap spectrally, interference effects can be induced between the pump and probe beams by introducing a time delay between the pulses. This technique, known as *wave packet interferometry* allows a more sophisticated variant of the Tannor-Rice scheme to be realised, exploiting both amplitude and phase control by introducing a second pulse whose phase is locked to the first one [54]. Experimentally, phase-locking requires precise control of the phase-difference between the two optical pulses, achieved using a stabilised interferometer. This type of interferometer is described in detail in chapter 3 and is used for the experiments described in chapter 5.

The first demonstration of this type of experiment for coherent control was carried out by Scherer *et al.* in I_2 [55,56]. The experiment proceeded as follows: the first pulse of a two pulse sequence transfers probability amplitude from the electronic ground state to an excited state potential energy surface, generating a coherent superposition of vibrational states (a wave packet). This wave packet is allowed to propagate along the vibrational coordinate. Some time later, on the order of the classical oscillation period of the system, a second identical pulse generates a wave packet on the same potential surface. As the phase between the two pulses is locked, this wave packet forms a superposition with the initial, propagated wave packet, providing a situation where interference between the wave packets can occur. This superposition of

amplitudes leads to constructive or destructive interference, giving rise to reduced or enhanced excited state population. The degree of interference depends on the delay between the optical pulses, and the nature of the wave packet evolution. The average excited state population was determined after the second pulse by measuring the total fluorescence. The situation described is essentially a double slit experiment in a molecule; the excited state amplitude in each molecule is the sum of the excitation amplitudes generated by two routes which are not distinguished from each other by measurement. Prior *et al.*, Shapiro *et al.* and Kauffmann *et al.* independently demonstrated that results similar to Scherer's could be obtained when they purposely introduced random phase fluctuations into the optical delay between the laser pulses [57-60]. It was later realised that femtosecond lasers are not needed for these types of experiments, now known as "coherence observation by interference noise" or COIN spectroscopy, and a broad bandwidth laser source could achieve the same result.

A major experimental advance that has had a major impact on controlling wave packet evolution is the tailoring of ultrashort laser pulses. In most experimental tailoring schemes, the laser pulse is first spatially and temporally dispersed with a diffraction grating and then focused with a lens or mirror [61,62]. The phases and amplitudes of the Fourier components of the pulse are filtered, then the dispersed colours are recompressed with a second focusing element and diffraction grating. Upon recompression, the pulse may be positively or negatively chirped so that either the low or high frequency components of the pulse reach the target first.

The above approach was first implemented by Kohler *et al.* [63,64], who used chirped pulses to prepare wave packets in I_2, which were then monitored using laser-induced fluorescence. They found that when the pulse was negatively chirped, the higher energy components of the wave packet were populated first. The states that were lower in energy and therefore excited later, caught up rapidly with the higher energy states at a predetermined time, producing a narrower, more localised wave packet. In contrast, a positively chirped pulse resulted in a delocalised wave packet.

Vibrational wave packets created and manipulated by chirped pulses have been studied in a variety of systems, for example I_2 [65-67], NaI [68] and Rb [69-71]. Gerber *et al.* showed how the multi-photon ionisation of the Na_2 dimer was strongly dependent on the chirp of the laser pulse [72]. Their experiments revealed that the ionisation efficiency of Na atoms using 618 nm laser pulses was influenced by the phase modulation of the laser pulses. They showed that the Na^+ signal was enhanced with negatively chirped pulses. However, with positively chirped pulses, no Na^+ ions were observed. Their explanation is as follows: in a negatively chirped pulse, the high-energy photons precede the lower-energy photons, and hence the atomic $3s \rightarrow 3p$ transition is induced by absorption of a photon at 589 nm (from the leading edge of a pulse negatively chirped pulse at 618 nm). Further absorption of a 616 nm photon leads to excitation of the Na(5*s*) state, from which photoionisation takes place. Conversely, in the case of a positively chirped pulse, the $3s \rightarrow 3p$ transition takes place when most of the laser intensity has already passed, therefore the probability of photoionisation from the 5*s* state is much lower and the atom remains in its 3*p* state.

As the field progressed, more sophisticated phase modulation techniques were introduced in the form of pulse shapers [73]. In simple terms, the role of the pulse shaper is to advance or retard individual frequencies within a laser pulse. For example, in a bandwidth limited laser pulse, all the frequencies are locked and the spectral phase is flat. The pulse shaper can be used on this type of pulse to make some frequencies arrive before others. Pulse shaping is generally performed by starting with an ultrafast laser pulse that is spectrally decomposed, followed by phase and amplitude modulation of the discrete frequency components. This modulation is usually carried out with acousto-optic [74] or liquid crystal techniques [75]. Bucksbaum *et al.* have employed phase-shaping methods to generate Rydberg wave packets with specific characteristics [76]. Leone *et al.* observed both rotational and vibrational recurrences of the E $^1\Sigma_g^+$ shelf state of Li_2 and demonstrated how the components of the vibrational wave packet could be altered [77]. Their first method involved selecting different vibrational states which were then projected onto the wave packet and second, using a mask to produce a

notch in the laser spectrum. This method was subsequently extended to achieve relative control over the phase of rotational and vibrational levels in a diatomic molecule [78-80].

Since quantum systems and their wave functions are three-dimensional objects, it has recently been realised that the use of polarization as an active agent could tremendously increase the degree of attainable control. In view of this, Brixner *et al.* [81,82] extended the pulse-shaping technique by modification of the conventional phase-only pulse shaper, to allow control of the spectral polarization of an ultrashort pulse. They found that the extra degrees of freedom enabled a substantial improvement on the controllability of the quantum system and succeeded in creating shaped pulses with frequency-dependent polarization [83].

In contrast with the previous examples, a different method of coherent control has been rapidly developing, which requires understanding of the phase-evolution of the individual components of a wave packet. This weak-field approach demands a superior understanding of the fundamental dynamics of the system, and consequently enables the design of intuitive coherent control strategies. There has been a great deal of interest in this type of control scheme in the context of Rydberg wave packets. For example, Noel and Stroud [84,85] demonstrated that a sequence of two laser pulses with a well-defined phase-difference modifies the state distribution compared to that of a single wave packet, leaving superpositions of only odd or even Rydberg states. More recently, Fielding *et al.* have exploited the phase evolution of angular momentum character in various Rydberg wave packet systems to control the orbital angular momentum in an atom [86], rotational angular momentum in a molecule [87], and the autoionisation/predissociation ratio [88].

1.3.3 Optimal field control and learning algorithms

It was soon proposed that given the complexity of the potential energy surfaces of reacting molecules, the use of a time-dependent field or a simple pulse sequence would

not be sufficient to achieve the most efficient control of product formation. As a result, optimal control theory was developed which enabled theoreticians to calculate the field required to achieve a specified goal. Tannor and Rice first touched upon optimal control theory when they demonstrated how to calculate the optimal dump pulse shape, for fixed pump pulse shape within the framework of perturbation theory [51]. However, it was Rabitz *et al.* [89,90] and independently, Kosloff *et al.* [91], who utilised the power of optimal control theory to calculate the temporal shape and spectral content of the pulse that maximises the yield of the desired product.

The Tannor-Rice-Kosloff-Rabitz method encompasses the original Tannor-Rice scheme with the condition that to generate a significant yield of a particular product, most of the wave packet amplitude on the excited state potential must be uniformly and compactly distributed over the product exit channel to the ground state potential. A problem is encountered here, as the time evolution of a wave packet results in interference between the constituent eigenstates. This phasing and de-phasing of the wave packet produces a complicated amplitude distribution on the excited state potential and therefore, a simple dump pulse cannot efficiently transfer amplitude to the exit channel.

This problem led to the development of optimal pulse shaping, by determining what initial amplitude distribution on the excited state potential surface will evolve to give the maximum amplitude over the product exit channel. This was achieved by integrating the Schrödinger equation backwards with the desired final amplitude as an initial condition. However, the result of the calculation produces an initial amplitude distribution so complicated that it cannot be created by a Franck-Condon transition from the ground state. This was circumvented by the use of a continuously applied temporally and spectrally shaped field, which enables amplitude to be transferred back and forth between the two potential energy surfaces as the wave packets are evolving.

A modification of this approach is the feedback-controlled shaping of ultrashort pulses proposed by Judson and Rabitz [92], which has since become a general scheme for coherent control [93]. In 1997 Wilson *et al.* implemented an experimental setup

which used an amplified femtosecond laser system, coupled to a pulse shaper under the control of an evolutionary learning (or genetic) algorithm, to optimise the phase and amplitude of femtosecond pulses [94]. The experiment had the simple goal of optimising the amount of two-photon induced fluorescence observed by the detector. For the first time, a computer program using a genetic algorithm was used to change individual phase and amplitude parameters to optimize the excitation of a molecule, without being guided by theory. The computer program was guided only by the signal amplitude, which it used to determine its progress.

Not long after this experiment was performed, additional examples of such optimisations using genetic algorithms were reported by Assion *et al.* [95], Meshulach *et al.* [96] and Weinacht *et al.* [97] who reported on the dissociation of a complex organometallic compound, ultrashort optical pulse compression and quantum holography respectively. More advanced programs adapt their search plan as the program evolves towards the optimum solution. Bucksbaum and coworkers have implemented an adaptive program in which the operators that control the generation of new individuals change as the program converges towards the final solution [98]. Since then, there has been a great deal of activity and success in employing learning algorithms to control various photochemical and photophysical processes, reflected by the number of recent reviews in the field [99-104].

1.4 CONCLUSION

In this chapter, an overview of coherent control has been presented. The field has led to the development of new equipment and techniques and has also improved the understanding of matter-light interactions. Whilst some coherent control schemes, pulse shaping for example, rely on technological means to extend the efficiency of the control, the work presented in this thesis relies heavily on an understanding of the system.

In chapter 4, it is shown how the evolution, and subsequent control, of vibrational wave packets is dependent on knowledge of the phase relationship between the eigenstates in the superposition. In chapter 5, we exploit the phase evolution of electronic wave packets to control the angular momentum character of a wave packet in atomic sodium. Both control schemes take place in the time domain using phase-locked pulse sequences.

Our methods show that once the system is understood, controlling the dynamics can take place on a fundamental level. Whilst these coherent control methods are relatively limited in terms of the amount of population transfer, they provide a promising weak-field alternative to other less tractable schemes, and are far more conducive to the inevitable extension to more complex systems.

1.5 REFERENCES

1. E. Hecht, *Optics*. Addison-Wesley, 1987.
2. P. Brumer and M. Shapiro, *Chem. Phys. Lett.* **126** (6), 541 (1986).
3. M. Shapiro and P. Brumer, *J. Chem. Phys.* **84** (7), 4103 (1986).
4. M. Shapiro, J. W. Hepburn, and P. Brumer, *Chem. Phys. Lett.* **149** (5-6), 451 (1988).
5. C. Chen, Y. Y. Yin, and D. S. Elliott, *Phys. Rev. Lett.* **64** (5), 507 (1990).
6. S. M. Park, S. P. Lu, and R. J. Gordon, *J. Chem. Phys.* **94** (12), 8622 (1991).
7. C. Chen and D. S. Elliott, *Phys. Rev. A* **53** (1), 272 (1996).
8. C. Chen and D. S. Elliott, *Phys. Rev. Lett.* **65** (14), 1737 (1990).
9. D. Xenakis, N. E. Karapanagioti, O. Faucher, E. Hertz, and D. Charalambidis, *J. Phys. B-At. Mol. Opt. Phys.* **32** (2), 341 (1999).
10. R. J. Gordon, S. P. Lu, S. M. Park, K. Trentelman, Y. J. Xie, L. C. Zhu, A. Kumar, and W. J. Meath, *J. Chem. Phys.* **98** (12), 9481 (1993).

11. V. D. Kleiman, L. C. Zhu, X. N. Li, and R. J. Gordon, *J. Chem. Phys.* **102** (14), 5863 (1995).
12. S. P. Lu, S. M. Park, Y. G. Xie, and R. J. Gordon, *J. Chem. Phys.* **96** (9), 6613 (1992).
13. H. Nagai, H. Ohmura, F. Ito, and T. Nakanaga, *Chem. Phys. Lett.* **383** (3-4), 240 (2004).
14. X. B. Wang, R. Bersohn, K. Takahashi, M. Kawasaki, and H. L. Kim, *J. Chem. Phys.* **105** (8), 2992 (1996).
15. G. Q. Xing, X. B. Wang, X. Huang, R. Bersohn, and B. Katz, *J. Chem. Phys.* **104** (3), 826 (1996).
16. V. D. Kleiman, L. C. Zhu, J. Allen, and R. J. Gordon, *J. Chem. Phys.* **103** (24), 10800 (1995).
17. J. A. Fiss, L. C. Zhu, K. Suto, G. Z. He, and R. J. Gordon, *Chem. Phys.* **233** (2-3), 335 (1998).
18. L. Zhu, K. Suto, J. A. Fiss, R. Wada, T. Seideman, and R. J. Gordon, *Phys. Rev. Lett.* **79** (21), 4108 (1997).
19. L. C. Zhu, V. Kleiman, X. N. Li, S. P. Lu, K. Trentelman, and R. J. Gordon, *Science* **270** (5233), 77 (1995).
20. T. Seideman, *J. Chem. Phys.* **108** (5), 1915 (1998).
21. S. Lee, *J. Chem. Phys.* **108** (10), 3903 (1998).
22. H. Lefebvre-Brion, *J. Chem. Phys.* **106** (6), 2544 (1997).
23. A. Khachatrian, R. Billotto, L. C. Zhu, R. J. Gordon, and T. Seideman, *J. Chem. Phys.* **116** (21), 9326 (2002).
24. H. L. Kim and R. Bersohn, *J. Chem. Phys.* **107** (12), 4546 (1997).
25. Y. Y. Yin, C. Chen, D. S. Elliott, and A. V. Smith, *Phys. Rev. Lett.* **69** (16), 2353 (1992).
26. B. Sheehy, B. Walker, and L. F. Dimauro, *Phys. Rev. Lett.* **74** (24), 4799 (1995).
27. H. Ohmura, T. Nakanaga, H. Arakawa, and M. Tachiya, *Chem. Phys. Lett.* **363** (5-6), 559 (2002).

28. H. Ohmura and T. Nakanaga, *J. Photochem. Photobiol. A-Chem.* **158** (2-3), 69 (2003).

29. D. W. Schumacher and P. H. Bucksbaum, *Phys. Rev. A* **54** (5), 4271 (1996).

30. D. W. Schumacher, F. Weihe, H. G. Muller, and P. H. Bucksbaum, *Phys. Rev. Lett.* **73** (10), 1344 (1994).

31. H. G. Muller, P. H. Bucksbaum, D. W. Schumacher, and A. Zavriyev, *J. Phys. B-At. Mol. Opt. Phys.* **23** (16), 2761 (1990).

32. C. P. Lin, J. Bates, J. T. Mayer, and W. S. Warren, *J. Chem. Phys.* **86** (8), 3750 (1987).

33. K. Bergmann, H. Theuer, and B. W. Shore, *Rev. Mod. Phys.* **70** (3), 1003 (1998).

34. A. Kuhn, S. Steuerwald, and K. Bergmann, *Eur. Phys. J. D* **1** (1), 57 (1998).

35. J. Martin, B. W. Shore, and K. Bergmann, *Phys. Rev. A* **54** (2), 1556 (1996).

36. T. Halfmann and K. Bergmann, *J. Chem. Phys.* **104** (18), 7068 (1996).

37. R. Sussmann, R. Neuhauser, and H. J. Neusser, *J. Chem. Phys.* **100** (7), 4784 (1994).

38. S. Schiemann, A. Kuhn, S. Steuerwald, and K. Bergmann, *Phys. Rev. Lett.* **71** (22), 3637 (1993).

39. J. S. Melinger, S. R. Gandhi, A. Hariharan, D. Goswami, and W. S. Warren, *J. Chem. Phys.* **101** (8), 6439 (1994).

40. B. Broers, H. B. V. Vandenheuvell, and L. D. Noordam, *Phys. Rev. Lett.* **69** (14), 2062 (1992).

41. D. J. Maas, D. I. Duncan, R. B. Vrijen, W. J. van der Zande, and L. D. Noordam, *Chem. Phys. Lett.* **290** (1-3), 75 (1998).

42. D. J. Maas, C. W. Rella, P. Antoine, E. S. Toma, and L. D. Noordam, *Phys. Rev. A* **59** (2), 1374 (1999).

43. R. B. Vrijen, D. I. Duncan, and L. D. Noordam, *Phys. Rev. A* **56** (3), 2205 (1997).

44. A. H. Zewail, *J. Photochem.* **17** (3-4), 269 (1981).

45. A. H. Zewail, *Femtochemistry: Ultrafast Dynamics of the Chemical Bond, Vol. 2*. World Scientific, 1994.

46. A. H. Zewail, *Femtochemistry: Ultrafast Dynamics of the Chemical Bond, Vol. 1*. World Scientific, 1994.

47. M. J. Rosker, M. Dantus, and A. H. Zewail, *J. Chem. Phys.* **89** (10), 6113 (1988).

48. M. Dantus, M. J. Rosker, and A. H. Zewail, *J. Chem. Phys.* **89** (10), 6128 (1988).

49. M. Dantus, M. J. Rosker, and A. H. Zewail, *J. Chem. Phys.* **87** (4), 2395 (1987).

50. D. J. Tannor, R. Kosloff, and S. A. Rice, *J. Chem. Phys.* **85** (10), 5805 (1986).

51. D. J. Tannor and S. A. Rice, *J. Chem. Phys.* **83** (10), 5013 (1985).

52. T. Baumert, B. Buhler, M. Grosser, R. Thalweiser, V. Weiss, E. Wiedenmann, and G. Gerber, *J. Phys. Chem.* **95** (21), 8103 (1991).

53. T. Baumert, M. Grosser, R. Thalweiser, and G. Gerber, *Phys. Rev. Lett.* **67** (27), 3753 (1991).

54. N. F. Scherer, A. J. Ruggiero, M. Du, and G. R. Fleming, *J. Chem. Phys.* **93** (1), 856 (1990).

55. N. F. Scherer, R. J. Carlson, A. Matro, M. Du, A. J. Ruggiero, V. Romerorochin, J. A. Cina, G. R. Fleming, and S. A. Rice, *J. Chem. Phys.* **95** (3), 1487 (1991).

56. N. F. Scherer, A. Matro, L. D. Ziegler, M. Du, R. J. Carlson, J. A. Cina, and G. R. Fleming, *J. Chem. Phys.* **96** (6), 4180 (1992).

57. C. Warmuth, A. Tortschanoff, F. Milota, M. Leibscher, M. Shapiro, Y. Prior, I. S. Averbukh, W. Schleich, W. Jakubetz, and H. F. Kauffmann, *J. Chem. Phys.* **114** (22), 9901 (2001).

58. O. Kinrot, I. S. Averbukh, and Y. Prior, *Phys. Rev. Lett.* **75** (21), 3822 (1995).

59. C. Leichtle, W. P. Schleich, I. S. Averbukh, and M. Shapiro, *J. Chem. Phys.* **108** (15), 6057 (1998).

60. C. Warmuth, A. Tortschanoff, F. Milota, M. Shapiro, Y. Prior, I. S. Averbukh, W. Schleich, W. Jakubetz, and H. F. Kauffmann, *J. Chem. Phys.* **112** (11), 5060 (2000).

61. R. L. Fork, O. E. Martinez, and J. P. Gordon, *Opt. Lett.* **9** (5), 150 (1984).

62. C. H. B. Cruz, P. C. Becker, R. L. Fork, and C. V. Shank, *Opt. Lett.* **13** (2), 123 (1988).

63. B. Kohler, J. L. Krause, F. Raksi, K. R. Wilson, V. V. Yakovlev, R. M. Whitnell, and Y. J. Yan, *Accounts Chem. Res.* **28** (3), 133 (1995).

64. B. Kohler, V. V. Yakovlev, J. W. Che, J. L. Krause, M. Messina, K. R. Wilson, N. Schwentner, R. M. Whitnell, and Y. J. Yan, *Phys. Rev. Lett.* **74** (17), 3360 (1995).

65. C. J. Bardeen, J. W. Che, K. R. Wilson, V. V. Yakovlev, V. A. Apkarian, C. C. Martens, R. Zadoyan, B. Kohler, and M. Messina, *J. Chem. Phys.* **106** (20), 8486 (1997).

66. V. V. Lozovoy, S. A. Antipin, F. E. Gostev, A. A. Titov, D. G. Tovbin, O. M. Sarkisov, A. S. Vetchinkin, and S. Y. Umanskii, *Chem. Phys. Lett.* **284** (3-4), 221 (1998).

67. I. Pastirk, E. J. Brown, Q. G. Zhang, and M. Dantus, *J. Chem. Phys.* **108** (11), 4375 (1998).

68. C. J. Bardeen, J. W. Che, K. R. Wilson, V. V. Yakovlev, P. J. Cong, B. Kohler, J. L. Krause, and M. Messina, *J. Phys. Chem. A* **101** (20), 3815 (1997).

69. S. Zamith, J. Degert, S. Stock, B. de Beauvoir, V. Blanchet, M. A. Bouchene, and B. Girard, *Phys. Rev. Lett.* **8703** (3), 033001 (2001).

70. P. Balling, D. J. Maas, and L. D. Noordam, *Phys. Rev. A* **50** (54276), 4276 (1994).

71. B. Broers, H. B. V. Vandenheuvell, and L. D. Noordam, *Opt. Commun.* **91** (1-2), 57 (1992).

72. A. Assion, T. Baumert, J. Helbing, V. Seyfried, and G. Gerber, *Chem. Phys. Lett.* **259** (5,6), 488 (1996).

73. A. M. Weiner, *Rev. Sci. Instrum.* **71** (5), 1929 (2000).

74. M. A. Dugan, J. X. Tull, and W. S. Warren, *J. Opt. Soc. Am. B-Opt. Phys.* **14** (9), 2348 (1997).

75. H. Kawashima, M. M. Wefers, and K. A. Nelson, *Annu. Rev. Phys. Chem.* **46**, 627 (1995).

76. H. Wen, C. Rangan, and P. H. Bucksbaum, *Phys. Rev. A* **68** (5), 053405 (2003).

77. J. M. Papanikolas, R. M. Williams, and S. R. Leone, *J. Chem. Phys.* **107** (11), 4172 (1997).

78. J. B. Ballard, H. U. Stauffer, E. Mirowski, and S. R. Leone, *Phys. Rev. A* **66** (4), 043402 (2002).

79. Z. Amitay, J. B. Ballard, H. U. Stauffer, and S. R. Leone, *Chem. Phys.* **267** (1-3), 141 (2001).

80. H. U. Stauffer, J. B. Ballard, Z. Amitay, and S. R. Leone, *J. Chem. Phys.* **116** (3), 946 (2002).

81. T. Brixner, G. Krampert, P. Niklaus, and G. Gerber, *Appl. Phys. B-Lasers Opt.* **74**, S133 (2002).

82. T. Brixner, N. H. Damrauer, G. Krampert, P. Niklaus, and G. Gerber, *J. Opt. Soc. Am. B-Opt. Phys.* **20** (5), 878 (2003).

83. T. Brixner, G. Krampert, T. Pfeifer, R. Selle, G. Gerber, M. Wollenhaupt, O. Graefe, C. Horn, D. Liese, and T. Baumert, *Phys. Rev. Lett.* **92** (20), 208301 (2004).

84. M. W. Noel and C. R. Stroud, *Phys. Rev. Lett.* **75** (7), 1252 (1995).

85. M. W. Noel and C. R. Stroud, *Phys. Rev. Lett.* **77** (10), 1913 (1996).

86. J. R. R. Verlet, V. G. Stavros, R. S. Minns, and H. H. Fielding, *Phys. Rev. Lett.* **89** (26), 263004 (2002).

87. R. S. Minns, R. Patel, J. R. R. Verlet, and H. H. Fielding, *Phys. Rev. Lett.* **91** (24), 243601 (2003).

88. R. S. Minns, J. R. R. Verlet, L. J. Watkins, and H. H. Fielding, *J. Chem. Phys.* **119** (12), 5842 (2003).

89. A. P. Peirce, M. A. Dahleh, and H. Rabitz, *Phys. Rev. A* **37** (12), 4950 (1988).

90. S. H. Shi, A. Woody, and H. Rabitz, *J. Chem. Phys.* **88** (11), 6870 (1988).

91. R. Kosloff, S. A. Rice, P. Gaspard, S. Tersigni, and D. J. Tannor, *Chem. Phys. Lett.* **139** (1), 201 (1989).

92. R. S. Judson and H. Rabitz, *Phys. Rev. Lett.* **68** (10), 1500 (1992).

93. H. Rabitz, R. de Vivie-Riedle, M. Motzkus, and K. Kompa, *Science* **288** (5467), 824 (2000).

94. C. J. Bardeen, V. V. Yakovlev, K. R. Wilson, S. D. Carpenter, P. M. Weber, and W. S. Warren, *Chem. Phys. Lett.* **280** (1-2), 151 (1997).

95. A. Assion, T. Baumert, M. Bergt, T. Brixner, B. Kiefer, V. Seyfried, M. Strehle, and G. Gerber, *Science* **282** (5390), 919 (1998).

96. D. Meshulach, D. Yelin, and Y. Silberberg, *Opt. Commun.* **138** (4-6), 345 (1997).

97. T. C. Weinacht, J. Ahn, and P. H. Bucksbaum, *Nature* **397** (6716), 233 (1999).

98. T. C. Weinacht and P. H. Bucksbaum, *J. Opt. B-Quantum Semicl. Opt.* **4** (3), R35 (2002).

99. T. Brixner and G. Gerber, *ChemPhysChem* **4** (5), 418 (2003).

100. M. Dantus and V. V. Lozovoy, *Chem. Rev.* **104** (4), 1813 (2004).

101. M. Shapiro and P. Brumer, *Rep. Prog. Phys.* **66** (6), 859 (2003).

102. I. Walmsley and E. Rabitz, *Phys. Today* **56** (8), 43 (2003).

103. H. Rabitz, *Science* **299** (5606), 525 (2003).

104. J. B. Ballard, H. U. Stauffer, Z. Amitay, and S. R. Leone, *J. Chem. Phys.* **116** (4), 1350 (2002).

CHAPTER 2:

WAVE PACKET DYNAMICS IN ATOMS AND MOLECULES

This chapter begins by introducing the dynamics of a two-level system within the framework of time-dependent perturbation theory. The following section describes the dynamics of two interfering wave packets from both the time- and frequency-domain perspective, providing the basis from which to explain the wave packet observation techniques employed in this thesis. Finally, a discussion of wave packet dynamics is presented with a brief analysis of quantum wave packet revivals in atomic and molecular systems.

2.1 THE DYNAMICS OF A TWO LEVEL SYSTEM

The interaction of light with an atom or molecule is of fundamental importance in the study and control of wave packet dynamics. An understanding of the light field and its interactions facilitates the design of logical coherent control schemes, allowing control over various dynamical processes. To illustrate these concepts a simple two-level system is considered, with an initial state $|m\rangle$ and final, excited state $|n\rangle$ coupled by a pulsed electric field:

$$E(t) = E_0 \cos(\omega t) f(t) \tag{2.1}$$

where ω is the laser frequency and $f(t) = \exp\left(-2\ln 2(t/\tau_p)^2\right)$ is the temporal profile of the laser pulse. The pulses are assumed to be Gaussian with a full-width half-maximum equal to τ_p. For this type of system, the total Hamiltonian H may be expressed as

$$H = H_0 + H'(t) \tag{2.2}$$

where the unperturbed Hamiltonian H_0 is time-independent and $H'(t)$ is a weak time-dependent perturbation. It is assumed that the perturbation is a periodic function of time, turned on at $t = 0$, and that it is harmonic, with angular frequency ω. It is also assumed that the electric field is polarized in the z direction, so that $E_0 = E_z$, and $E_x + E_y = 0$. As the force exerted on an electron by this field is given by $-e \cdot E(t)$, the resulting potential energy responsible for the perturbation can be written as $V = eE(t)z$.

The following section assumes that the eigenvalues of the unperturbed Hamiltonian H_0, are known and the corresponding eigenfunctions ψ_0, are orthogonal and form a complete set. Since it is known that the only transition that will occur is between two levels m and n, the solution of the time-dependent Schrödinger equation for the two level system described can be expressed as a superposition of wavefunctions

$$\Psi(r,t) = a_m(t)\psi_m(r)e^{-i\omega_m t} + a_n(t)\psi_n(r)e^{-i\omega_n t}, \tag{2.3}$$

where a_m and a_n are the time-dependent population amplitudes for states $|m\rangle$ and $|n\rangle$ respectively, and ω_m and ω_n are the corresponding angular frequencies. The general solution to the time-dependent Schrödinger equation is given by

$$H\Psi = i\hbar\frac{\partial\Psi}{\partial t}. \tag{2.4}$$

In order to determine the unknown coefficients a_n, (2.3) is substituted into (2.4), multiplied by the complex conjugate $\psi_n(r)^*$ and integrated over all space. Using the fact that $H_0\psi = E_0\psi$, the equation for the coefficient a_n is found to be

$$\dot{a}_n(t) = \frac{1}{i\hbar}eE(t)\langle n|z|m\rangle e^{i(\omega_n-\omega_m)t}a_m(t) \tag{2.5}$$

This is the well-known result of first order time-dependent perturbation theory [1]. By expanding the expression for the light field using (2.1), equation (2.5) can be simplified by defining the Rabi coupling for the system:

$$\Omega_n = \frac{1}{\hbar}eE_0\langle n|z|m\rangle \tag{2.6}$$

This expression gives the probability of the system being in state *n*, and with further simplification, (2.5) can be written as

$$\dot{a}_n = -\frac{i}{2}\Omega_n f(t)\left[e^{i(\omega_n-\omega_m+\omega)t} + e^{i(\omega_n-\omega_m-\omega)}\right] \tag{2.7}$$

In order to solve (2.7), it is assumed that the intensity of the perturbing light field is so weak that the population amplitude of the initial state remains virtually unchanged by the perturbation – this approximation is referred to as the *weak field* limit. A further

assumption is made regarding the angular frequency of the light field, and is incorporated by introducing the 'detuning' angular frequency, Δ_n, where

$$\Delta_n = \omega_n - \omega_m - \omega \tag{2.8}$$

Equation (2.7) can not be solved exactly, but if it is assumed that $\Delta_n << \omega$, which has the result of forcing the angular frequency to remain close to its resonant value, the terms in $\exp[\pm i(\Delta_n)t]$ will be much more important that those in $\exp[\pm i(\omega + \omega_n - \omega_m)t]$. This condition is valid as the latter terms oscillate much more rapidly, and on average make negligible contribution to $\dot{a}_n$. Consequently, it is reasonable to neglect these higher frequency terms. This is known as the *rotating wave approximation* [2], as the only terms which are kept in the expression are those which occur when the time dependence of the system and the perturbation are in phase. These assumptions allow (2.7) to be reduced to

$$\dot{a}_n = -\frac{i}{2}\Omega_n f(t) e^{i\Delta_n t} \tag{2.9}$$

The full derivation is given in appendix 2. Using the same reasoning applied to (2.9), the following expression is obtained for state *m*:

$$\dot{a}_m = -\frac{i}{2}\Omega_n f(t) e^{-i\Delta_m t} \tag{2.10}$$

In the study and control of wave packet dynamics, we are primarily concerned with the population of the excited state. (2.9) is therefore the relevant expression in all the work described in this thesis and it will be the focus of the following discussion. Once the perturbation has been switched off, the probability amplitude for state *n* can be obtained by integrating (2.9):

$$a_n(t) = -\frac{i}{2}\Omega_n g(\omega) \tag{2.11}$$

where

$$g(\omega) = e^{-\left[(\Delta_n \tau_p)^2 / 8\ln 2\right]} \tag{2.12}$$

is the Fourier transform of $f(t)$[3] (see appendix 3 for derivation). The relevance of this derivation to wave packet dynamics and control is apparent when one views the perturbing field as the laser pulse. In this case, the lower level *m* represents a ground or intermediate state of an atom or molecule and the upper state *n* represents the Rydberg state(s), in the case of an electronic wave packet or the vibrational state(s) in the case of vibrational wave packet. The broad bandwidth of a short laser pulse excites a superposition of electronic or vibrational states in an atom or molecule thereby creating the wave packet. As the above derivation showed, the probability amplitude of the relevant state is fixed once the perturbation has been switched off. Therefore the distribution of states in a wave packet is determined by the duration and profile of the laser pulse and is fixed before the wave packet starts to evolve.

2.2 WAVE PACKET EVOLUTION

A wave packet is formed when a short laser pulse creates a superposition of a number of highly excited states of an atom or molecule. The constituent wave functions are eigenstates of the system and are therefore stationary states; however the superposition itself is not a solution of the Schrödinger equation and can therefore be described as non-stationary state[1]. In the case of Rydberg wave packets, the wave packet moves along a classical trajectory until it reaches its outer turning point, where it gets reflected back by the strong Coulombic potential in this region. The wave packet then continues its classical behaviour by oscillating in the radial coordinate, passing through the core

[1] For a discussion of stationary states of the Hamiltonian, see *Quantum Mechanics* by Cohen-Tannoudji, (volume 1, p. 246 [1]).

region at multiples of the classical orbit period (denoted T_{cl}) in analogy to a classical electron in a Coulomb potential. Similarly, a wave packet formed by a superposition of vibrational states oscillates at the classical vibrational frequency of the system.

The long-term evolution of a wave packet is more complex. If the energy levels that make up a wave packet were equally spaced in energy, its localisation and motion would remain unchanged – this type of coherent state is analogous to the coherent state of a harmonic oscillator. This wave packet would have many properties of a classical system and would retain them. Energy levels in atoms or molecules, whether they are electronic, vibrational or rotational, exhibit anharmonicity to varying degrees. This causes the wave packet evolution to deviate from classical behaviour at longer times, although it retains its classical periodicity at short times. The beating frequency between the most widely spaced pair of energy levels oscillates with the highest frequency. Smaller spaced pairs beat at lower frequencies. This results in spreading of the wave packet. The wave packet then enters a so-called "collapsed phase" [4] where the probability is spread non-uniformly around the classical trajectory. On a much longer timescale, the wave packet relocalises in the form of a quantum revival (denoted T_{rev}), in which the spreading is reversed and the classical periodicity of the wave packet motion is once more apparent. The structures that occur between T_{cl} and T_{rev}, with periodicities equal to fractions of T_{cl}, are found at times equal to rational fractions of the revival time, $(p/q)T_{rev}$. These have been interpreted as the temporary formation of mini-packets and are termed *partial revivals*; they have $(1/q)$ of the total probability of the initial wave packet, and exhibit local periodicities of T_{cl}/q.

The following section describes the origin of wave packet revivals and partial revivals. The fact that wave packets exhibit this blend of quantum and classical behaviour is central to many mechanisms of temporal coherent control. In chapter 4, vibrational wave packets in the sodium dimer are investigated. The near harmonic energy levels spacings of the excited states of Na_2 make it an ideal candidate for the exploration of coherent control strategies using the fundamental motions of a molecule. By exploiting the near-classical motion during the first vibrational period, it is shown

how the vibrational motion, in conjunction with cleverly designed pulse sequences, can be used to modify the wave packet composition and hence control the dynamics. Conversely, the significantly greater anharmonicity exhibited by the Rydberg states of Na provides an opportunity to exploit the quick formation of the revivals and partial revivals in an effort to control the Rydberg state population and the corresponding dynamics. With this approach to coherent control in mind, the dynamical behaviour of a generic wave packet in a bound one-dimensional anharmonic potential is discussed.

2.2.1 THE AUTOCORRELATION FUNCTION

The study of the time evolution of wave packets, in this thesis and elsewhere, makes use of the concept of the overlap $(\langle\psi_t|\psi_0\rangle)$ of the time-dependent quantum state ψ_t with the initial state ψ_0. This overlap is referred to as the autocorrelation function and can be evaluated in either position- or momentum- space to give

$$A(t) \equiv \langle\psi_t|\psi_0\rangle = \int_{-\infty}^{+\infty} \psi^*(x,t)\psi(x,t)\,dx = \int_{-\infty}^{+\infty} \phi^*(p,t)\phi(p,t)\,dp \tag{2.13}$$

This expression clearly shows that in order for $|A(t)|$ to be large, the wavefunction at later times must have significant overlap with the initial state in both position and momentum space.

For a generic, one-dimensional system a wave packet can be expressed as the sum of the individual energy eigenfunctions $\psi_n(x)$, with corresponding eigenvalues E_n, weighted by the laser pulse profile and transition probabilities, given by a_n:

$$\Psi(x,t) = \sum_{n=0}^{\infty} a_n \psi_n(x) e^{-iE_n t/\hbar} \tag{2.14}$$

The autocorrelation function can now be expressed as

$$A(t) = \sum_{n=0}^{\infty} |a_n|^2 e^{iE_n t/\hbar} \tag{2.15}$$

The autocorrelation function is of obvious theoretical value in the analysis of time-dependent systems, as it is a relatively simple and intuitive way of analysing wave packet dynamics. From the point of view of the work presented in this thesis, it is highly relevant; the calculations presented in chapter 4 rely on the autocorrelation function to provide an accurate description of the controlled vibrational wave packet dynamics in the sodium dimer. The autocorrelation function is also directly related to the observable ionisation signal in the experiments presented in chapter 5, where the optical Ramsey method [5] is used to monitor Rydberg wave packet dynamics in atomic sodium.

2.2.2 TIME DEPENDENCE OF WAVE PACKETS

If a localised wave packet is excited with an energy spectrum which is tightly spread around a large central value of the quantum number $\bar{n}$, so that $\bar{n} >> \Delta n >> 1$, it is appropriate to expand the individual energy eigenvalues in the exponential of (2.14) around this value:

$$E(n) \approx E(\bar{n}) + E'(\bar{n})k + \frac{E''(\bar{n})}{2}k^2 + \ldots \tag{2.16}$$

where $k = (n - \bar{n})$. If we let $E = \hbar\omega$, where $\omega = (2\pi/T_{cl})$ and substitute back into the exponential of (2.14):

$$e^{-iE_n t/\hbar} = \exp\left[-\frac{it}{\hbar}\left(E(\bar{n}) + \hbar\frac{2\pi}{T_{cl}}k + \frac{\hbar^2}{2}\frac{2\pi}{T_{cl}}\left(\frac{\partial\omega}{\partial E_n}\right)k^2 + \ldots\right)\right]$$

$$\equiv \exp\left[-2\pi i\left(\frac{t}{T_{cl}} + \frac{kt}{T_{cl}} + \frac{k^2 t}{T_{rev}} + \ldots\right)\right] \tag{2.17}$$

Here, each term in the expansion, apart from the first, defines an important point in the wave packet evolution:

$$T_{cl} = \frac{2\pi\hbar}{|E(\bar{n})|}, \quad T_{rev} = \frac{2\pi\hbar}{|E''(\bar{n})|/2} \tag{2.18}$$

See appendix 4 for a detailed derivation of (2.17) and (2.18). The distribution of $E(\bar{n})$ is dependent on the system. For example, the series expansion of the energy around $\bar{n}$ for Rydberg states (where $E_n = 1/2n^2$) has the effect of firstly shifting and then removing the symmetry of the harmonic energy level spacings [6]. This is explored in more detail in appendix 5.

The first term in (2.17) is an *n*-independent overall phase. It represents the average oscillation frequency of the population amplitude of the wave packet and as it is common to all terms in the expansion, it does not induce interference between them. The second term in the expansion is linear in *k* and is associated with the classical period of motion. It represents the harmonic dephasing and rephasing of the individual amplitude components and corresponds to the classical oscillation period of the system. The third term in the expansion is quadratic in *k*. This expression, associated with the quantum revival timescale. It is responsible for the long term $(t >> T_{cl})$ spreading of the wave packet and interestingly, for times of the order of T_{rev}, the additional $\exp(2\pi i \delta n^2 t/T_{rev})$ phase terms all equal 1, approximating a return to classical behaviour.

2.2.3 REVIVALS AND PARTIAL REVIVALS

The following section will describe the behaviour of the wave packet at the significant times in its trajectory, namely at short times equivalent to $T_{cl} \leq t << T_{rev}$, at long times equivalent to $T_{cl} << t \leq T_{rev}$ and at significant intermediate times. To examine the temporal behaviour of wave packets from T_{cl} to T_{rev}, the wavefunction can be restricted to the first two derivative terms in the expansion given in (2.17) giving

$$\Psi(x,t)=\sum_k a_k \psi_k(x) e^{-2\pi i\left(kt/T_{cl}+k^2 t/T_{rev}\right)} \tag{2.19}$$

Firstly, at short times where $T_{cl} \le t << T_{rev}$, the terms proportional to k^2 in the exponent in (2.19) can be neglected since the timescale T_{rev} will not be manifested. Therefore $\Psi(x,t+T_{cl})=\Psi(x,t)$ and after a time equal to the classical period, the wave packet will return to its earlier position in an unchanged form. This essentially means that the wave packet evolves according to the correspondence principle[2]. At later times the dephasing of the individual terms in the superposition become apparent due to the terms quadratic in *k*. This dephasing leads to a decay of the wave packet after a number of classical periods (the timescale of which depends explicitly on the strength of the anharmonicity of the system). However, in a finite system with a discrete energy spectrum, this dephasing is reversible. Actually, for $t = T_{rev}$ the additional phases due to the terms quadratic in *k* are integral multiples of 2π, so that the wave packet is in fact completely restored and the wave packet exhibits classical oscillations. This phenomenon has been called the "revival" of the wave packet [7].

The next step is to investigate the structure of the wave packet at intermediate times $T_{cl} < t < T_{rev}$. As can be seen in fig 2.3, before the full revival occurs, there appears to be a general pattern of well defined revivals, characterised by temporally localised structures in $A(t)$. As previously mentioned, these structures have a local periodicity of T_{cl}/q with magnitude $|A(t)|^2 = 1/q$ and occur at various rational multiples of the revival time, given by $t = pT_{rev}/q$. Averbukh and Perelman [8] were the first to analyse in detail the mathematical structure of the additional phase factors arising from the $\exp(-2\pi i k^2 t/T_{rev})$ terms in the energy expansion. The coherent control schemes employed in this thesis rely heavily on the intricacies of wave packet evolution. Consequently, the original arguments in [8] are reproduced, in part, in the following section. A good starting point is to consider the form of (2.19) when

[2] The correspondence principle states that in the limit of large numbers, or as $\hbar \to 0$, the predictions of quantum theory must coincide with the predictions of classical mechanics.

$$\frac{t}{T_{rev}} = \frac{p}{q} \tag{2.20}$$

where p and q are integers and p/q is an irreducible fraction of integers. The condition (2.20) is chosen because the additional phase shifts due to terms proportional to k^2 are equal to $2\pi\Theta_k$ where $\Theta_k = (p/q)k^2$, so that

$$\exp\left(-2\pi i k^2 t/T_{rev}\right) = e\left(-2\pi i (p/q)k^2\right) \equiv e\left(-2\pi i \Theta_k\right) \tag{2.21}$$

It can be shown that the quantities Θ_k form periodic sequences in k with period l. Key features of the wave packet structure, such as the revivals, are closely tied to the periodicity of the Θ_k phase term in the vicinity of these relevant times. So, near $t \approx (p/q)T_{rev}$ the terms quadratic in k in (2.19) lead to additional phase factors which are l periodic in k. It is now assumed that the phase factors with the same periodicity in k appear in the expansion of the wave packet when all non-linear phases are ignored, and are shifted in time by an integer multiple of T_{cl}/l with respect to the initial wave packet. This assumption allows the wavefunction, at time $t = (p/q)T_{rev}$, to be expressed in the form

$$\Psi(x,t) = \sum_{s=0}^{l-1} a_s \Psi_{cl}\left(x, t + (s/l)T_{cl}\right) \tag{2.22}$$

where

$$\Psi_{cl}(x,t) = \sum_{k=0}^{\infty} a_k \psi_k(x) \exp\left(-2\pi i k t/T_{cl}\right) \tag{2.23}$$

describes the classical evolution of the wave packet. This is allowed since the second order effect is small for times shortly after excitation, therefore a wave packet in its first period of evolution can be approximated as a classical wave packet. In (2.23), the amplitudes a_s, which all have the same value, are given by

$$a_s = \frac{1}{l}\sum_{k=0}^{l-1} \exp\left(\mp 2\pi i k\Theta_k + 2\pi i k \frac{s}{l} \right). \tag{2.24}$$

In effect, (2.24) describes the entire evolution of the wave packet as a superposition of a few classical packets; the precise number of classical packets is dependent on which stage the wave packet is at in its evolution. An analytical expression for a_s exists, and can be found in ref. [9]. The remainder of this section will show some examples of the different structures that occur at different points in the wave packet evolution. Ref. [4] provides a very detailed account of the mathematics of wave packet revivals as do the original papers [8,10], so the objective of this section is to highlight examples of typical structures observed in the evolution of a wave packet, that are relevant to the work discussed in chapters 4 and 5 of this thesis.

To examine specific structures, a good starting point is the simplest case, which occurs when $t \approx T_{rev}/2$:

$$\Psi(x,t) = \psi_{cl}\left(x, t + \frac{1}{2}T_{cl} \right) \tag{2.25}$$

This is simply the original wave packet shifted in time by half a classical period. At this time the wave packet appears to have fully revived. This structure is often referred to as the full revival as it resembles the initial wave packet, and has an oscillation period of T_{cl}, but as this analysis shows, it is not technically a full revival as the odd eigenstates are π out of phase with the even eigenstates [8]. The first observation of this type of revival in an atomic system was presented in [7].

The next logical step is to consider the case where $t \approx T_{rev}/3$, as this is the first case where q is odd ($p = 1$ and $q = l = 3$). Using the expansion in (2.24) we can determine the amplitude coefficient:

$$a_0 = \frac{1}{3}\sum_{k=0}^{2} \exp\left(-2\pi i k^2/3\right) = -\frac{i}{\sqrt{3}} \tag{2.26}$$

Therefore, near $t \approx T_{rev}/3$ it is found that

$$\Psi(x,t) = -\frac{i}{\sqrt{3}}\left[\psi_{cl}(x,t) + e^{2\pi/3}\left\{\psi_{cl}\left(x, t+\frac{T_{cl}}{3}\right) + \psi_{cl}\left(x, t+\frac{2T_{cl}}{3}\right)\right\}\right] \tag{2.27}$$

Expression (2.27) describes an essentially non-classical object, consisting of a superposition of three correlated localised wave packets, shifted in time from one another by $T_{cl}/3$. This type of structure also occurs for $t/T_{rev} = 1/6$, $2/3$ and $5/6$. In common notation, the structure at $t/T_{rev} = 1/6$ is referred to as a *third order partial revival*, as it is the first time that the wave packet is split into three parts.

In a similar way, the next relevant example is the first case where q is a multiple of 4, which occurs at $t = T_{rev}/4$:

$$\Psi(x,t) = \frac{1}{\sqrt{2}}\left[\exp(-i\pi/4)\psi_{cl}(x,t) + \exp(i\pi/4)\psi_{cl}x, t+\frac{T_{cl}}{2}\right] \tag{2.28}$$

This expression shows that there are two replicas of the original wave packet, separated in time by half the classical period. The arguments for even q differ slightly depending on whether q is a multiple of 4. The results however, are similar in that one finds $r = q/2$ copies of the original wave packet, separated by multiples of T_{cl}/r. Although in the terminology of Averbukh and Perelman, the example described above is a revival of the fourth order, in most wave packet studies, including the ones presented in this thesis, this is referred to as a *second order* partial revival. In the same way as the structures observed at $t = T_{rev}/6$ are referred to as thirds order partial revivals, this structure is a second order partial revival as it is the first time the wave packet is split into two parts. Examples of wave packet revival structures are illustrated in figures 2.1 and 2.2.

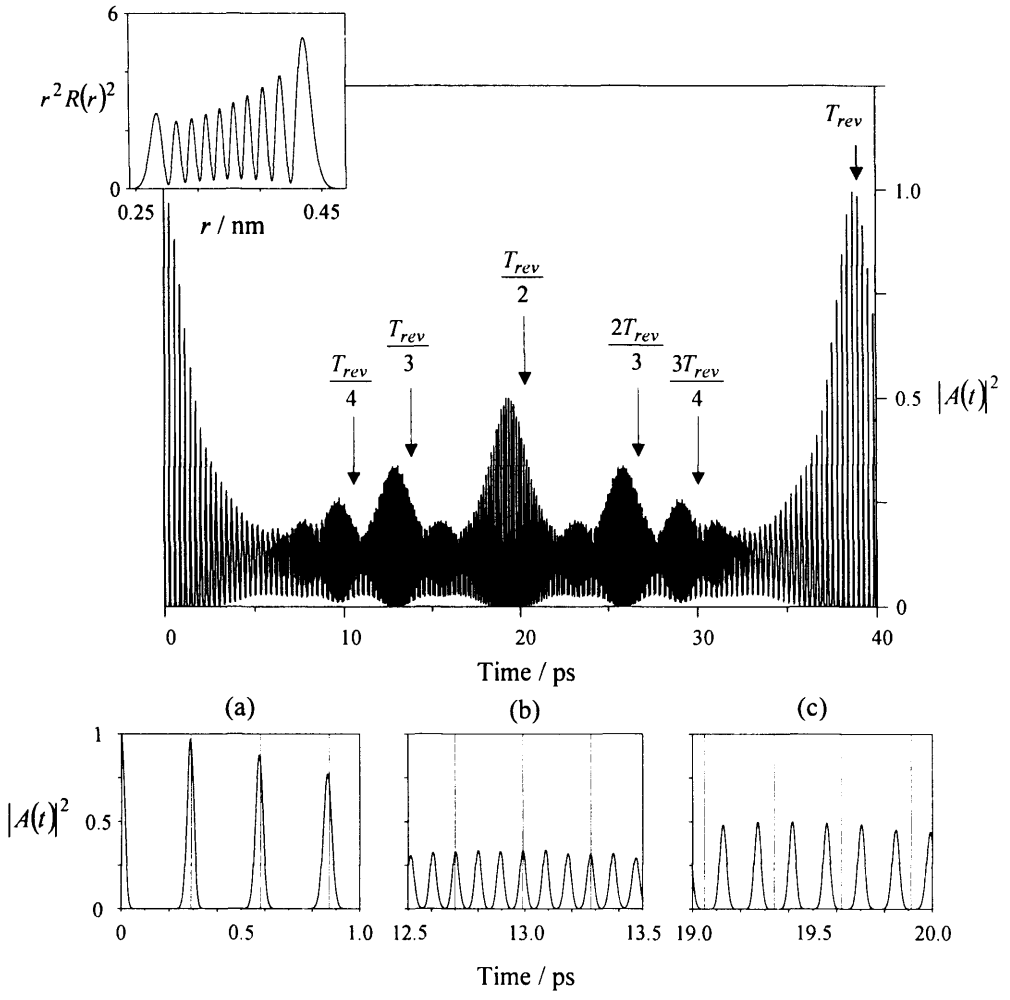

Figure 2.1 Main figure: recurrence spectrum of a vibrational wave packet excited around the $v = 9$ level of the $X^{+2}\Sigma_g^+$ state of Na_2^+, with a 30 fs bandwidth limited laser pulse. The full revival, as well as second, third and fourth order partial revivals are clearly visible. The inset shows the radial distribution function of the wave packet immediately after its creation. Plots (a), (b) and (c) show enlarged sections of the main figure at times $t = 0$, $t \approx 13.5$ ps and $t \approx 19$ ps respectively. The horizontal lines represent the classical oscillation period of the wave packet. At $t = 0$ (plot (a)), the wave packet is oscillating at the classical vibrational frequency. Plot (b) is an enlarged section of the third order partial revival, and the wave packet is oscillating at three times the classical frequency and has one third of the population of the wave packet at $t = 0$. Similarly, at the second order partial revival, shown in plot (c), the wave packet is oscillating at twice the classical frequency and has half the population of the wave packet at $t = 0$. All wave packet spectra are normalised to the wave packet at $t = 0$, and are plotted on the same vertical scale with arbitrary intensity units.

Figure 2.1 shows the autocorrelation function $|A(t)|^2$, of a vibrational wave packet excited around $v = 9$ in the $X^{+1}\Sigma_g^+$ state of Na_2^+ with a 30 fs bandwidth limited laser pulse[3]. The radial distribution function for the $v = 9$ state is also plotted to show the structure of the states that make up the superposition. This particular example was chosen as the excited electronic states of diatomic molecules are ideally suited for the demonstration of partial revivals, due to fact that the vibrational spectrum is closely quadratic – required by the Averbukh and Perelman theory [8]. As can be seen in figure 2.1, the full revival occurs at $t \approx 38$ ps, and is the same intensity as the wave packet at $t = 0$. The second order partial revival occurs at around $t \approx 19$ ps and is half the intensity of that at the full revival. Also clearly present, are the third and fourth order partial revivals.

In this thesis, both electronic and vibrational wave packets are studied. Therefore, to highlight the subtle differences between these two types of wave packet, the recurrence spectrum of a Rydberg electron wave packet is presented in figure 2.2. This plot illustrates a wave packet excited from the ground $1s$ state to the $40p$ state of atomic hydrogen, with a one picosecond, bandwidth limited laser pulse. The differences in the electron and vibrational wave packet spectra are predominantly due to the differing forms of the potentials in which the energy levels lie. An electronic wave packet is made up of a superposition of Rydberg states – the high lying electronic states in atoms and molecules, characterised by high principal quantum number n. A characteristic feature of an atom or molecule with a single excited Rydberg electron is that the electronic motion is dominated by a pure Coulomb force at large distances from the positively charged ionic core [11]. In contrast, vibrational energy levels lie in the Morse potential (discussed in more detail in chapter 4). Therefore, the distinct appearance of the wave packets in figures 2.1 and 2.2 is largely due to the potential in which the energy levels lie, which effectively determines the level of dispersion, and hence the overall character of the wave packet. The other important factor is the

[3] The purpose of this plot is to show the positions of various revival structures and the corresponding intensities of a typical vibrational wave packet excited in a diatomic molecule. For this reason, the Franck-Condon factors for this excitation are all set to 1, so that the revival structures are not distorted.

structure of the radial distribution functions, presented as insets in figures 2.1 and 2.2. The vastly differing probability distributions over the electronic orbit, in the case of electron wave packets, and the vibrational coordinate, in the case of vibrational wave packets are important factors in determining the initial wave packet probability distribution.

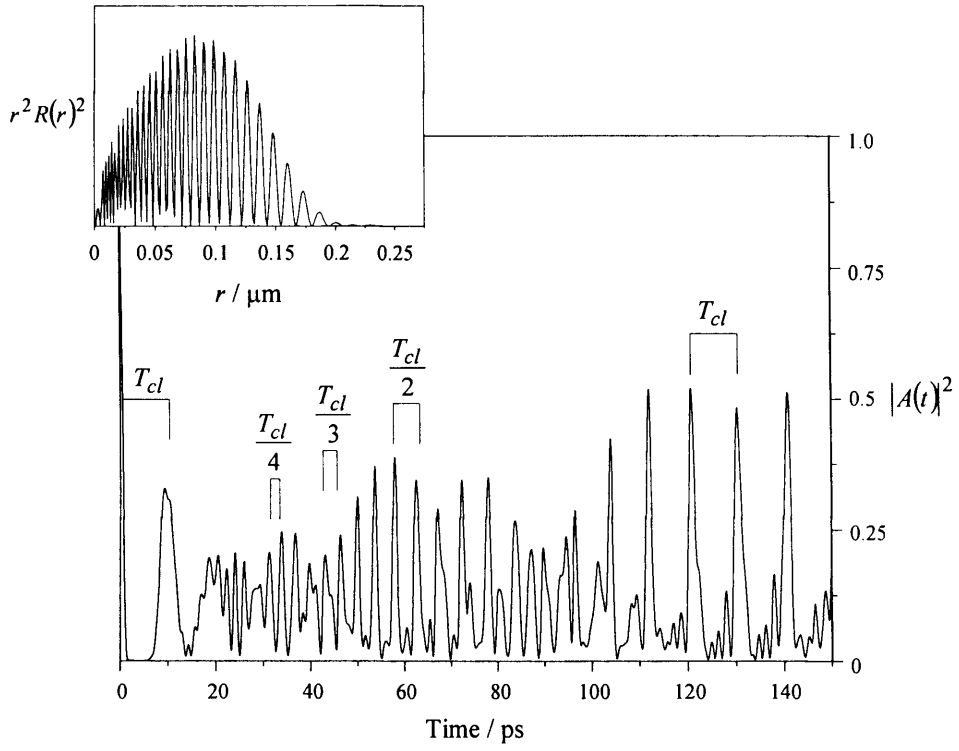

Figure 2.2 Main figure: recurrence spectrum of a Rydberg electron wave packet in the hydrogen atom, excited around $n = 40$ with a 1 ps bandwidth limited laser pulse. In a similar way to the vibrational wave packet, the periodicity of the wave packet is fully visible at the full revival, as well as second, third and fourth order partial revivals. In contrast to the vibrational wave packet, after just one classical oscillation, the electronic wave packet has started to disperse and after just two classical oscillations, a 5^{th} order partial revival is visible. The inset shows the radial distribution function of the of the electronic wave packet immediately after its creation. Unlike the radial distribution function of the vibrational wave packet which is spread out over the vibrational coordinate, it is localised at the inner turning point. Once created, the wave packet travels to the outer turning point of the Coulombic potential, where it will reach its maximum potential energy before being drawn back to the core.

To further illustrate the dynamics of a Rydberg wave packet, figure 2.3 shows the probability density of a radial wave packet

$$|\Psi(r,t)|^2 = r^2\left|\sum_n a_n R_{nl}(r)e^{-i\omega_n t}\right|^2, \tag{2.29}$$

plotted as a function of time t and radial coordinate r, where a_n and ω_n are the amplitudes and angular frequencies of the Rydberg states in the superposition.

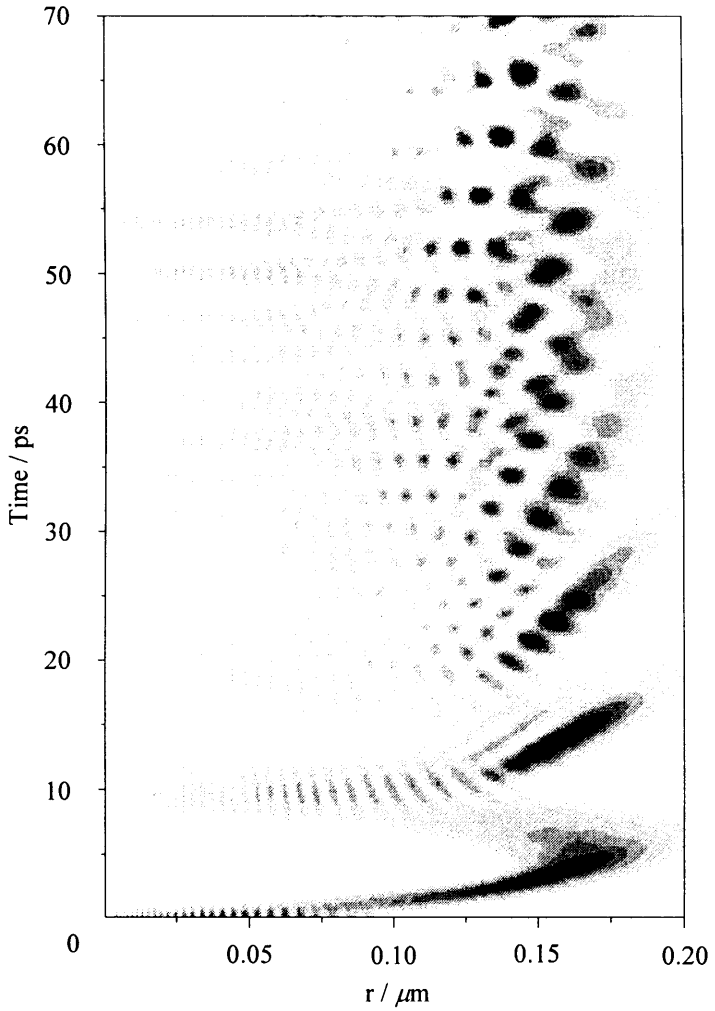

Figure 2.3 Time dependent radial distribution function of a radial electron wave packet excited around n = 40 in the hydrogen atom, with a bandwidth limited 1 ps pulse. The dark sections indicate a high probability amplitude. At short times, the classical evolution of the wave packet is apparent, as it is seen to oscillate between the core and the outer turning point at the classical period. At longer times, quantum mechanical behaviour manifests itself as the wave packet spreads and begins to exhibit non-classical behaviour.

The excitation parameters are the same as in the previous examples i.e. the wave packet is excited from the ground $1s$ state to the $40p$ state of atomic hydrogen, with a one picosecond, bandwidth limited laser pulse.

The wave packet is formed initially at the inner turning point, where it is localised in the radial coordinate. It then travels rapidly away from the positively charged nucleus towards the outer turning point of the Coulomb potential. At this point, the kinetic energy of the wave packet decreases and it becomes fairly localised at the edge of the potential. The wave packet then travels rapidly back to the ionic core with a total round trip of approximately 10 ps. It is apparent that after just one oscillation, the wave packet probability distribution has begun to broaden, a result of the anharmonicity of the Coulomb potential. After approximately 20 ps the wave packet has dispersed over the whole of the radial coordinate and the partial revivals begin to become apparent.

2.3 WAVE PACKET INTERFERENCE

2.3.1 MULTIPLE PULSE EXCITATION

The above description of wave packet excitation allows a straightforward extension to show the effect of multiple pulses on the final state probability amplitudes. Assuming a sequence of k identical laser pulses, launched at times t_k after the first pulse, the total electric field for the excitation is extended from (2.1) to:

$$E(t) = E_0 \cos(\omega t) f(t) + \sum_k E_0 \cos[\omega(t - t_k)] f(t - t_k) \tag{2.30}$$

and the corresponding population amplitudes after the pulse sequence is

$$a_n(t) = -\frac{i}{2}\Omega_n g(\omega)\left[1 + \sum_k \exp(i\Delta_n t_k)\exp(i\omega t_k)\right] \tag{2.31}$$

For each individual excited state n, the term in square brackets in (2.31) oscillates rapidly at the angular frequency $\omega_n - \omega_m$, which is the same frequency as the angular component of the electric field by which that specific state was excited. From this argument, it is apparent how the slightly differing angular frequencies of the various states in a wave packet superposition will oscillate in and out of phase with one another, causing constructive and destructive interference in wave packet amplitude. These interference effects within the wave packet amplitude are discussed further in the following section.

2.2.2 RAMSEY FRINGES

Both the experimental and theoretical work presented in this thesis rely on the ability to monitor the excited state population, with the ultimate aim of gaining complete control over the final state composition of the wave packet, and the resulting dynamics. When considering wave packet interference, the last term in (2.31) is the most important. The square of this term is proportional to the excited state population and oscillates between 0 and 4. The term in the first exponential in (2.31) is a rapidly oscillating term (ωt_k), which is the product of the laser frequency and the delay between the pulses. This term is associated with the phase difference between the wave packets. The second term $(\Delta_n t_k)$, where $\Delta_n = \omega_n - \omega_m - \omega$ is the 'detuning' angular frequency, represents a much slower oscillation responsible for the period of wave packet evolution and is associated with the overlap of the wave packets. See reference [12] for a detailed derivation of these terms. This is represented graphically in figure 2.4, which is a plot of the total excited state population $\left|\sum_n a_n(t)\right|^2$, versus the delay time between the two pulses. In this example, taken from [13], a sequence of two identical bandwidth limited pulses excites a superposition of p Rydberg states from the ground $1s$ level in the hydrogen atom. The pulses are one picosecond long (τ_p = 1 ps) and have a central frequency corresponding to excitation of the n = 40 level in hydrogen. The Ramsey fringes

depicted in figure 2.4 have been calculated with a scaled down optical frequency, so that both the oscillations at the optical frequency and the wave packet envelope are clear. In this particular example, the optical frequency was scaled by a factor of 2000. In reality, there are around 3000 optical cycles per picosecond. The overall envelope in figure 2.4 shows the oscillation of the radial wave packet. At $t = 0$, excitation from the 1s state creates a wave packet localised in the core region. The wave packet travels up the Coulombic potential and reaches its maximum potential energy at the outer turning point, at ~5 ps, before being drawn back to the core with high kinetic energy. The first complete evolution of the wave packet, T_{cl}, lasts for ~10ps. The energy difference between adjacent Rydberg states scales as n^{-3}, therefore the higher energy electronic states oscillate more rapidly than the lower energy states and the wave packet distribution spreads, as can be seen in the broadening of the wave packet envelope.

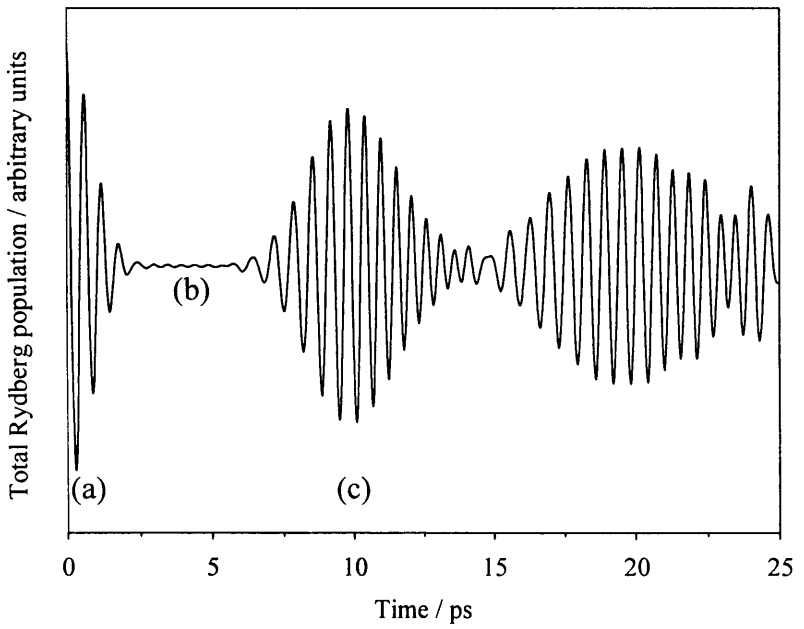

Figure 2.4 A plot of the total population of hydrogen atom Rydberg states after excitation by a sequence of two identical, one picosecond pulses. The wave packet is created at $t = 0$, (a) and reaches the outer turning point of its motion at approximately 5 ps, (b). The first evolution of the wave packet, T_{cl}, takes approximately 10 ps, (c). In reality, there are many more oscillations at the optical frequency than depicted – to make the figure clearer, the optical frequency has been scaled down by a factor of 2000.

The rapidly oscillating terms can be explained in terms of the delay, t_k, between the two pulses. For $t = 0$, the pulses overlap and the excited state distribution will be at a maximum. If the second pulse is delayed by a time $t = t_k + t_\phi$, where $t_\phi << \tau_p$ and $t_\phi = \phi/\omega$ corresponds to an optical phase shift ϕ with reference to the optical frequency ω, there will be interference between the two light pulses as they are still overlapped spatially. First, consider the case when $\phi = \pi$, which corresponds to a delay of half an oscillation of the optical field. This delay causes the two pulses to be π out of phase with one another, and as the atom is not exposed to any field at this point, there will be no population in the excited state. Conversely if $\phi = 2\pi$, there will be constructive interference between the light pulses resulting in maximum excitation of the atom. Therefore in this region close to $t = 0$, point (a) on figure 2.4, constructive and destructive interference between the two light pulses determine the final excited state population and correspondingly peaks and dips, or "fringes" are observed in the total excited state population, $\sum_n a_n^2(t)$, at the optical frequency.

Now consider the case where the two optical pulses are temporally separated by a time $t \approx T_{cl}/2$, where $T_{cl} = 2\pi/\omega$ - the classical oscillation period of the system.. The first pulse creates a wave packet which travels to the outer turning point, at which point the second wave packet is excited. In the current example, $T_{cl}/2 \approx 5$ ps. The two wave packets do not overlap spatially and therefore cannot interfere with one another; in this case the total Rydberg population around this time is simply the incoherent sum of the contributions from each pulse. This is illustrated in region (b) in figure 2.4.

The final scenario to consider is when the two pulses are temporally separated by one orbit period, $t = T_{cl} \approx 10$ ps, (c) in figure 2.4. This can be explained by likening the behaviour of the atom to that of an interferometer: The first pulse creates a wave packet. This wave packet travels to the outer turning point and returns to the core, at which point a second pulse launches a second wave packet in the core region. These two wave packets interfere constructively or destructively depending on the optical phase difference between the two excitation pathways. Consequently, just as at t = 0, interference fringes are observed in the final Rydberg state population at the optical

frequency. These fast oscillations are referred to as Ramsey fringes [12]: the first pulse creates some excited state population, whilst the phase of the second delayed pulse determines whether this excited state population in enhanced or diminished.

An alternative, and perhaps simpler, perspective on this type of wave packet interference is obtained by Fourier transforming the two pulses. If we consider one pulse with a Gaussian profile, the Fourier transform would yield a Gaussian frequency spectrum. The Fourier transform of two Gaussian pulses, separated by a delay of the order of a wave packet oscillation, gives the same frequency spectrum, but with a modulation superimposed on it. These modulations shift as a function of the delay between the pulses so if the peaks overlap in frequency with the eigenfrequencies of the states in the excitation, those particular states will become populated. If the delay between the two pulses is equal to T_{cl}, the spacing of the peaks in the frequency domain spectrum correspond to the spacing between the states in the original excitation, so that the peaks coincide with the excitation frequencies of the Rydberg states. If the delay between the pulses is equal to $T_{cl}+\pi$, this has the effect of flipping the phase of the second optical pulse by π and hence, phase shifting the modulation in the frequency spectrum by π. In this case, the *dips* in the frequency spectrum correspond to the excitation frequencies of the Rydberg states and no Rydberg population is excited. The spectral profiles obtained by Fourier transforming a pulse pair, with delays corresponding to (a) 0, (c) T_{cl} , (d) $T_{cl}+\pi$ are illustrated in figure 2.5. In this example the excitation is made from the $40p \leftarrow 1s$ transition in the Hydrogen atom by a pair of identical, bandwidth limited, one picosecond optical pulses. For reference, the positions of the Hydrogen Rydberg levels are also presented along the top of the plot.

An interesting scenario occurs when the pulses are separated by $T_{cl}/2$, illustrated in figure 2.5(b). In this case the peaks in the frequency spectrum coincide with the excitation frequencies of alternate states in the superposition, enabling the creation of a wave packet that consists of only odd or even states. Even more interesting is the situation that arises then the pulses are separated by $3T_{cl}/2$, illustrated in figure 2.5(e). This situation is similar to the case where the pulses are separated by $T_{cl}/2$, in

that alternate Rydberg states are excited, but the frequency profile is in fact very different.

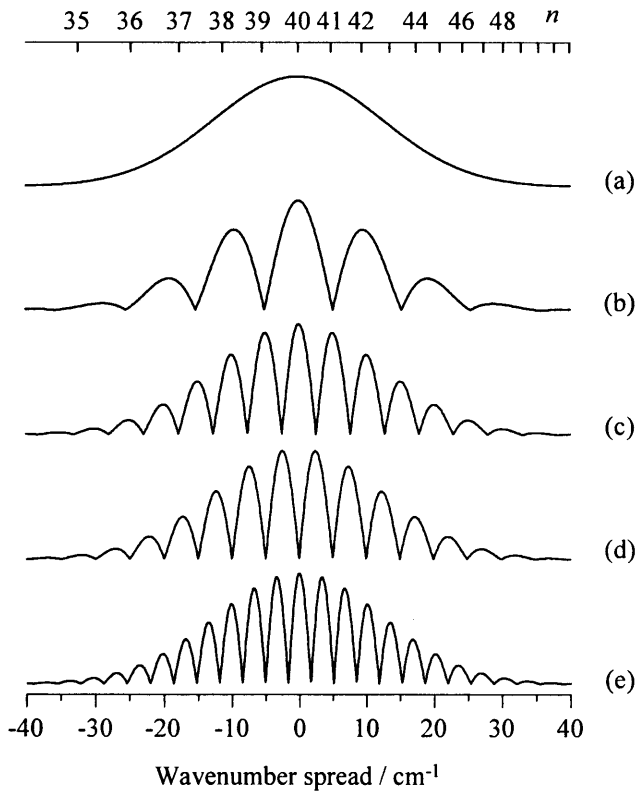

Figure 2.5 A plot of the spectral profiles obtained from Fourier transforming of pair of bandwidth limited, optical pulses separated by (a) 0, (b) $T_{cl}/2$, (c) T_{cl}, (d) $T_{cl}+\pi$ and (e) $3T_{cl}/2$. The pulses are one picosecond long and have a central frequency corresponding to the $40p \leftarrow 1s$ transition in atomic Hydrogen. The frequency spectra are all plotted on the same intensity scale. The Hydrogen Rydberg states are plotted at the top of the figure for reference.

As can be seen in figure 2.5(b), Fourier transforming a pair of pulses separated by $T_{cl}/2$ results in a frequency spectrum where *every* peak and dip occurs at a Rydberg state frequency. In contrast, the Fourier transform of a pair of pulses separated by $3T_{cl}/2$ results in a frequency spectrum where every third peak and every third dip corresponds to a Rydberg state frequency. This has implications for the coherent control of wave packets composed of interleaved series, as the peaks and dips can be made to coincide with the frequencies of specific series. This type of control is employed in the

experiments discussed in chapter 5, where a pair of bandwidth limited laser pulses with carefully designed delays are used to control the angular momentum composition of an electron wave packet in atomic sodium, by modifying the population of *s* and *d* Rydberg states.

2.3 CONCLUSION

This chapter has provided an introduction to the formation and dynamics of atomic and vibrational wave packets. Through the optical Ramsey method and the corresponding frequency domain analysis, a description of the phase evolution of the wave packet is presented. Knowledge of the evolution of wave packets has allowed the formation of intuitive coherent control schemes and provided a basis for the theory and experiments presented in chapters 4 and 5.

2.4 REFERENCES

1. C. Cohen-Tannoudji, B. Diu, and F. Laloe, *Quantum Mechanics*. Wiley, 1977.
2. B. H. Bransden and C. J. Joachain, *Physics of Atoms and Molecules*, 2nd ed. Prentice Hall, 2003.
3. X. Chen and J. A. Yeazell, *Phys. Rev. A* **56** (3), 2316 (1997).
4. R. W. Robinett, *Phys. Rep.* **392**, 1 (2004).
5. G. Alber, H. Ritsch, and P. Zoller, *Phys. Rev. A* **34** (2), 34 (1986).
6. J. Wals, H. H. Fielding, and H. B. V. van den Heuvell, *Physica Scripta* **T58**, 62 (1995).
7. J. Parker and C. R. Stroud, *Phys. Rev. Lett.* **56** (7), 716 (1986).
8. I. S. Averbukh and N. F. Perelman, *Phys. Lett. A* **139** (9), 449 (1989).
9. J. H. Hanney and M. V. Berry, *Physica D* **1**, 267 (1980).

10. I. S. Averbukh and N. F. Perelman, *Sov. Phys. Usp.* **34** (7), 572 (1991).

11. G. Alber and P. Zoller, *Phys. Reps.* **199** (5), 231 (1991).

12. L. D. Noordam, D. I. Duncan, and T. F. Gallagher, *Phys. Rev. A* **45** (7), 4734 (1992).

13. H. H. Fielding, *Ann. Rev. Phys. Chem.* **56**, 91 (2004).

CHAPTER 3:

EXPERIMENTAL TECHNIQUES FOR THE CREATION, OBSERVATION AND CONTROL OF ELECTRONIC AND VIBRATIONAL WAVE PACKETS

This chapter describes the experimental methods and equipment used to excite, monitor and control the dynamics of electronic and vibrational wave packets. The coherent control technique employs sequences of optical pulses, which are phase-locked using a stabilised Michelson interferometer. The wave packet dynamics are monitored using the optical Ramsey method, and the population amplitudes are determined using state selective field ionisation. A new vacuum chamber and sodium oven are described, as well as a novel detection technique for observing vibrational wave packets in an ion state potential.

3.1 INTRODUCTION

This chapter begins by describing the various laser systems employed for the coherent control studies presented in chapters 4 and 5. In chapters 4 and 6, the theory and preliminary results for an experiment controlling vibrational wave packets in the sodium dimer are discussed. Chapter 5 details the coherent control scheme and subsequent results for an experiment controlling the angular momentum composition of Rydberg electron wave packets in the sodium atom. In both cases, a two-photon excitation scheme is employed, illustrated in figure 3.1(a) for Na and 3.1(b) for Na_2.

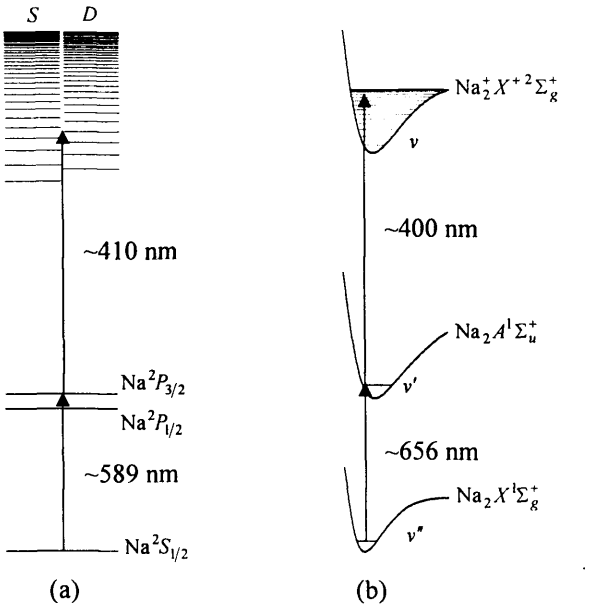

Figure 3.1 Two-photon excitation schemes for excitation and control of (a) Rydberg electron wave packets in Na and (b), vibrational wave packets in Na_2^+. In both cases, a narrow-bandwidth laser accesses an intermediate state. In Na, a picosecond laser creates electron wave packets whilst in Na_2^+, a femtosecond laser excites Rydberg and vibrational states.

In both schemes, the first photon is provided by a narrow-bandwidth nanosecond laser, which accesses the intermediate $^2P_{3/2}$ state in Na and the $A^1\Sigma_u^+$ state in Na_2. The second photon is responsible for wave packet creation. In Na, a picosecond laser excites a

superposition of Rydberg states to create a radial wave packet. In Na_2, we propose a scheme in which very high-lying Rydberg states, each converging to several vibrational limits of the ion, are excited by a femtosecond laser. It is anticipated that the motion of the vibrational wave packet can be filtered out of the radial motion of the Rydberg wave packet (this proposed detection scheme is discussed in detail in section 3.8).

3.2 LASERS

3.2.1 TIME-RESOLVED EXPERIMENTS

Wave packets in Na

The laser set-up for the wave packet experiments in Na is illustrated in figure 3.2, and as mentioned in section 3.1, a two-photon excitation scheme is employed. The first step is to access the $^2P_{3/2}$ state in Na, which acts as a 'launch' state from which the wave packets are excited. To excite the $^2P_{3/2}$ state, a Nd:YAG laser acts as the pump for a narrow-bandwidth nanosecond dye laser, which produces the necessary wavelength to access the $^2P_{3/2}$ state in sodium. The pump laser is a Q-switched Nd:YAG laser (Continuum Powerlite 8010), with a repetition rate of 10 Hz. This laser produces 8 ns pulses with a fundamental wavelength of 1064 nm, which is discarded, and a second harmonic wavelength at 532 nm. The second harmonic beam is typically 5 W, which is equivalent to 500 mJ pulse^{-1} at 10 Hz. Approximately 40% of this second harmonic output of the Nd:YAG laser is used to pump a narrow-bandwidth nanosecond dye laser (Continuum ND6000), containing the dye Rhodamine 610 dissolved in methanol (0.11 g L^{-1}). This dye is capable of producing a wavelength range 578 – 610 nm, with a maximum lasing wavelength of 590 nm, so it is suitable for accessing the $^2P_{3/2} \leftarrow {}^1S_{1/2}$ transition in atomic sodium, at 589.15 nm. The output pulses have a bandwidth of 0.08 cm^{-1}, and at 589.15 nm, the output power is typically 2.5 μJ pulse^{-1}. The wavelength is

measured, to two decimal places, with a wavelength meter (Angstrom WS-7), which is calibrated periodically using a stabilised HeNe laser of known wavelength (632.8 nm).

A separate laser set-up is required to create electronic wave packets in Na: a Nd:YAG laser is used to pump a broad-bandwidth, picosecond dye laser. The pump laser is a modelocked Nd:YAG laser (Coherent Antares), which produces 532 nm, 50 ps pulses at a repetition rate of 76 MHz. The output power is typically 2.0 – 2.5 W. The output of the picosecond Nd:YAG laser is used to pump a picosecond dye laser (Coherent 701). To access the n = 30 - 40 Rydberg states in Na at λ = 409.5 – 411.0 nm, the output of this laser is amplified using a sequence of Bethune cells (discussed in the following section) and then doubled by passing though a doubling crystal. To achieve this wavelength range, the dye Styryl 9 is used (1 g L^{-1} in a 4:6 mixture of propylene carbonate and ethylene glycol), which lases over the wavelength range 805 – 840 nm. The temporal profile of the output pulses from the picosecond dye laser is monitored using an autocorrelator (Coherent FR – 03), and the resulting pulse length is typically 1 ps. However, the pulses are not bandwidth limited and the corresponding bandwidth is actually closer to 21 cm^{-1} – equivalent to a 0.7 ps pulse. This bandwidth was determined by comparison of the resulting wave packet recurrence spectra with a range of calculated spectra obtained with different bandwidths. The output pulses are typically around 100 mW (equivalent to 1.3 nJ $pulse^{-1}$). The wavelength is tuned with a 2-plate birefringent filter situated inside the laser cavity and measured with the wavelength meter as described above.

Wave packets in Na_2^+

The set-up for wave packet excitation in Na_2^+ involves a very similar set-up to that described above. The intermediate $A\,^1\Sigma_u^+$ state of Na_2 is also accessed with a nanosecond laser set-up: a narrow-bandwidth nanosecond laser (Sirah Precisionscan) pumped by the second harmonic of a Nd:YAG laser (Continuum Powerlite 8010). As above, the Nd:YAG operates at 10 Hz, with a second harmonic output power of 5 W

(equivalent to 500 mJ pulse^{-1}). 40 % of output of the Nd:YAG is used to pump the nanosecond dye laser, containing the dye DCM dissolved in DMSO (0.18 g L^{-1}). This dye has a lasing wavelength range of 634 – 686 nm, with a central wavelength of 650 nm. The vibrational levels of the A state from which we wish to launch the wave packet, range from $v' = 5$ to $v' = 9$ resulting in $A(v') \leftarrow X(v'' = 0)$ transition energies ranging from 637.6 nm to 656.21 nm – well within the limits of the dye. The output pulses are 8 ns, with a bandwidth of 0.001 cm^{-1}. At the maximum lasing wavelength of the dye, the power output is 6 mJ pulse^{-1}.

Vibrational wave packets are excited from the intermediate A state with the output of a modelocked, ultrafast Ti:Sapphire laser (Coherent Mira Seed). The output pulses are ultrashort, broad bandwidth, femtosecond pulses with a repetition rate of 76 MHz. The CW power is typically 600 – 800 mW, with a corresponding modelocked power of 450 – 600 mW (6-8 nJpulse^{-1}). A birefringent filter enables the Mira Seed to be tuneable from 780 - 840 nm. The laser is specified to produce pulses of 40 fs at 800 nm. The wavelength and bandwidth of the pulses are measured on a laser spectrum analyser (Ist-Rees E200 series). At 400 nm, we can typically achieve a bandwidth of 154 cm^{-1}, which corresponds to a pulsewidth of 48 fs assuming the pulse is Gaussian. The time-bandwidth product for a Gaussian pulse is 0.411 [1].

3.2.2 FREQUENCY-RESOLVED EXPERIMENTS

The preliminary studies for wave packet experiments involve the recording of frequency spectra. In Na, our first step was to access, and record a frequency spectrum of the ^2P states, one of which would act as our intermediate state. The next step was to obtain a frequency spectrum of the Rydberg states ranging from around $n = 20$ to the ionisation limit. This allowed us to visualise the states that would make up the Na wave packets. In Na_2, we obtained frequency spectra of several relevant vibrational levels of the intermediate A state. By selecting a specific vibrational level, we can determine the

composition of a wave packet excited from it. In both the Na and Na_2 experiments, the frequency resolved spectra are obtained with similar nanosecond laser set-ups.

Frequency resolved spectra of Na

The intermediate states (the $^2P_{3/2}$ state in Na and the $A\,^1\Sigma_u^+$ state in Na_2) are accessed in exactly the same way as they are accessed in wave packet experiments i.e. with a narrow bandwidth nanosecond dye laser (either the Continuum ND-6000 or the Sirah Precisionscan) which is pumped by the second harmonic of a Q-switched nanosecond Nd:YAG laser (Continuum Powerlite 8010). In the case of atomic sodium, approximately 40% of the Nd:YAG laser is used to pump the Continuum ND-6000 dye laser equipped with the dye Rhodamine 610 dissolved in methanol (0.11 g L^{-1}). This wavelength range of this dye is 578 – 610 nm, with a maximum lasing wavelength of 590 nm; suitable for accessing the $^2P_{3/2} \leftarrow^1 S_{1/2}$ transition in atomic sodium at 589.15 nm. To take a frequency spectrum of the Rydberg states of atomic sodium, the frequency tripled output of the nanosecond Nd:YAG (1 W, 100 mJ $pulse^{-1}$) is used to pump a second nanosecond dye laser (Sirah Precisionscan). The ionisation limit for sodium is 41 449.451 cm^{-1} and the transition energy from the $^2P_{3/2}$ state is 24 476.08 cm^{-1} (408.56 nm). Therefore, to obtain a frequency spectrum a dye is required that has a lasing range of approximately 405 – 415 nm (Exalite 411 (0.13 g L^{-1} in para-dioxane) was used which has a lasing wavelength range of approximately 401 - 422 nm. The output pulse power was 10 μJ $pulse^{-1}$ at 410 nm. At this wavelength, we can scan the laser over 3 – 4 nm with 0.002 nm resolution, to cover a range of principal quantum numbers ranging from n = 20 to the ionisation limit. The resulting Rydberg spectra are presented in chapter 5.

Frequency resolved spectra of Na_2^+

To obtain a frequency spectrum of the intermediate A state in Na_2, the same laser set-up was used as the one described in section 3.2.1. Frequency spectra were recorded by 1 + 2 resonance-enhanced multiphoton ionisation (REMPI) using the narrow-bandwidth nanosecond laser (Sirah Precisionscan) pumped by the second harmonic of a Nd:YAG laser (Continuum Powerlite 8010). As described above, the dye laser contains the dye DCM dissolved in DMSO (0.18 g L^{-1}). The output pulses are typically 8 – 10 mJ $pulse^{-1}$ when pumped by 100% of the Nd:YAG. The spectra were recorded by directing approximately 8% of the output of the dye laser into a wavelength meter (Angstrom WS-7), through a home-built, UV compatible fibre-optic patch cable. As the wavelength is scanned, it is continually measured by the wave meter, and written to a file alongside the ion signal intensity. Some preliminary frequency spectra have been obtained of, what we believe, is the $A(v'=9) \leftarrow X(v''=0)$ transition in Na_2. However, there is a discrepancy of approximately 15 cm^{-1} in the line positions when compared to known experimental values [2]. This work is ongoing, with the aim of providing a preliminary characterisation of the molecular beam temperature, through comparison of the intensity profile of the P and R branches with calculated line spectra.

The schematic layout of the laser table presented in figure 3.2. This particular set up is specific to the detection and control of electron wave packets in Na, and is illustrated as these experiments are responsible for the majority of the experimental results presented in this thesis. However, the set-up is generic for the majority of the experiments discussed. For the frequency resolved experiments in both Na and Na_2, the picosecond Nd:YAG laser was replaced with a second narrow bandwidth nanosecond laser, and the interferometer was not present. For the time resolved experiments, the interferometer is crucial, and a single interferometer is illustrated. If wave packets are detected using the optical Ramsey method (discussed in section 3.8) the single interferometer is modified to a double nested interferometer, described in detail in section 3.7. The schematic layout of the ultrafast amplification set-up, again, unique to

the time-resolved experiments, is also illustrated. The details of the amplification are described in detail in section 3.3

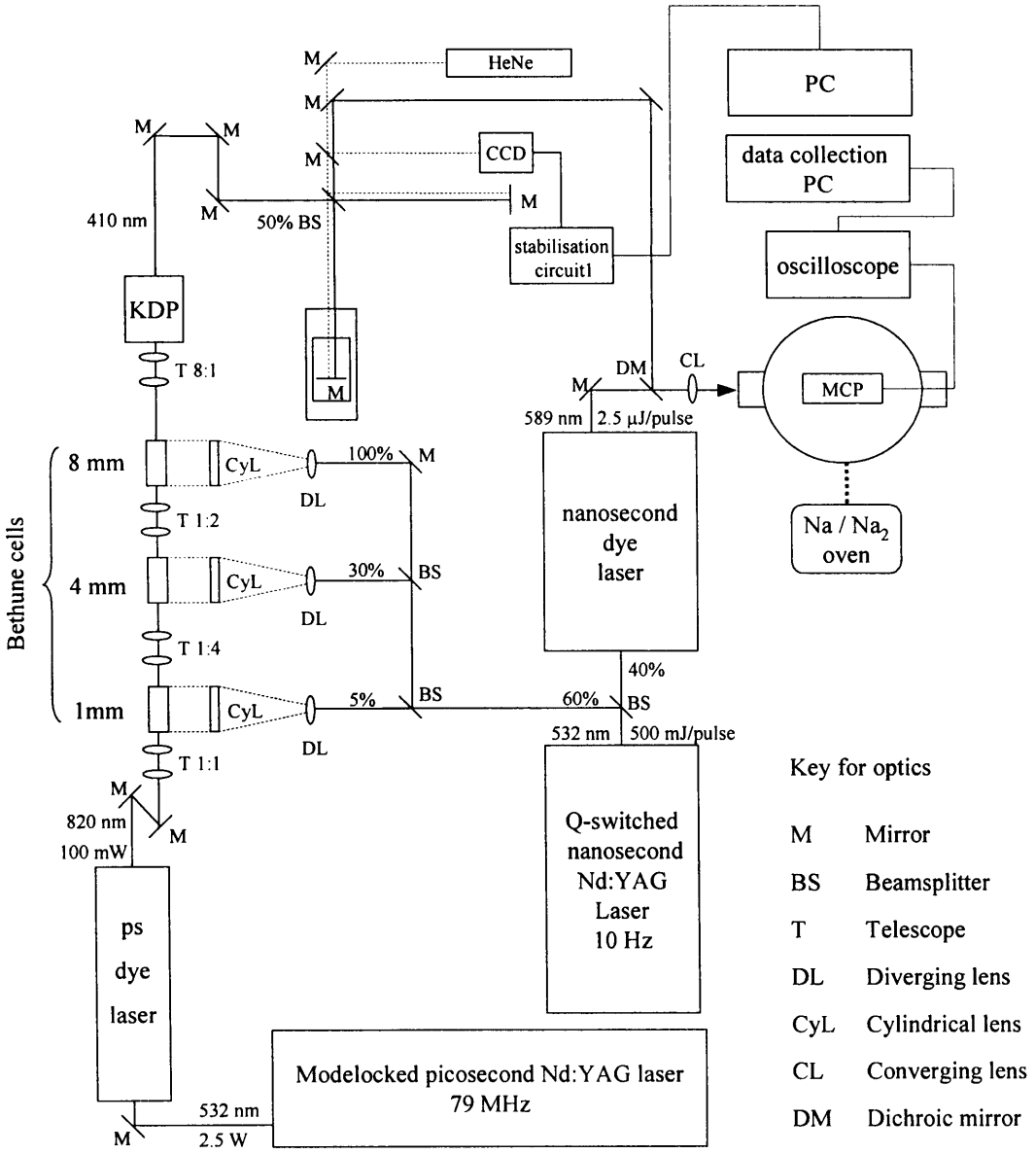

Figure 3.2 A schematic diagram of the laser set-up used excite wave packets in Na. Similar set-ups are used for the other experiments described in this thesis. A nanosecond Nd:YAG is used to pump a narrow bandwidth nanosecond dye laser and to amplify the picosecond light through the Bethune cells. The picosecond pulses are generated in an ultrafast dye laser pumped by a modelocked Nd:YAG laser. Pairs of phase-locked picosecond pulses are generated in a stabilised Michelson interferometer, combined with the nanosecond light and focused into the sodium atomic beam in the vacuum apparatus.

3.3 ULTRAFAST AMPLIFICATION

In our experiments, the intermediate state is accessed with a 10 Hz system. Therefore the output of the 76 MHz picosecond or femtosecond pulse train produced by the ultrafast lasers needs to be synchronised and amplified at 10 Hz. To increase the power per pulse, the 76 MHz pulse train from either the femtosecond Ti:sapphire or the picosecond dye laser is sent through a home-built, three-stage dye amplifier, consisting of three different sized dye cells. The dye cells are Bethune cells [3], which are specifically designed to maintain beam quality through uniform pumping of the dye. In the experiments described in this thesis, the Bethune cells are typically pumped with 60% of the 500 mJ pulse^{-1}, 532 nm, 10 Hz output of a nanosecond Nd:YAG laser. The Bethune cell set-up is illustrated in figure 3.2. The first Bethune cell is 1 mm in diameter and is pumped by ~15 mJ pulse^{-1} of 10 Hz Nd:YAG laser. This first cell is capable of amplifying the ultrafast pulses from approximately 1 – 5 nJ pulse^{-1} to about 2 – 4 μJ pulse^{-1}. The diameter of the beam is expanded by a 1:4 telescope before entering the second Bethune cell, which is 4 mm in diameter. This cell is pumped by ~85 mJ pulse^{-1} of the 10 Hz Nd:YAG laser and amplifies the ultrafast pulses to approximately 60 μJ pulse^{-1}. At the third stage, the beam diameter is doubled by a 1:2 telescope for entry into a 8 mm Bethune cell. This third cell is pumped by approximately ~200 mJ pulse^{-1} of the 10 Hz Nd:YAG laser resulting in ultrafast pulse energies of up to 300 μJ pulse^{-1}.

The basic design of a Bethune cell, illustrated in figure 3.3, is based on a 45° right-angled, fused silica prism with a small hole drilled just below the centre through which the dye solution flows. If the pump beam is four times the diameter of the hole in the prism, total internal reflection from the inside faces of the prism uniformly and efficiently pumps the dye from all sides.

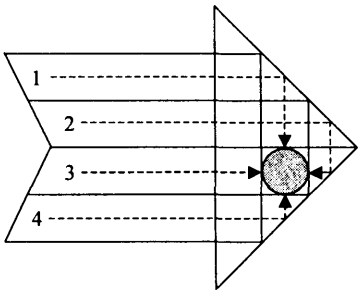

Figure 3.3 End view of a Bethune cell. Pump light enters from the left and due to total internal reflection, equal portions (1-4) pump the top, back, front and bottom of the dye solution (the grey circle).

The amplification is maximised if the dye concentration is adjusted so that $\alpha r = 1$, where α is the absorption coefficient for the pump light and r is the radius of the hole. The smaller the hole radius, the more efficient the Bethune cell is at amplifying. However, the efficiency is therefore limited by the total energy per unit area, or fluence, that can be extracted from a cell. Consequently, to achieve higher pulse energies, larger Bethune cells must be used, despite their inferior amplification efficiency. In practice, the specific concentrations required for each Bethune cell are determined by optimising the power of the pulses after each cell whilst concentrating or diluting the dye solution. A stock solution of 50 mg L^{-1} of the relevant dye and solvent is made, which also provides the solution for the first cell. The stock solution is diluted by the same proportion as the size of the Bethune cells increases i.e. the first Bethune cell is 1 mm in diameter and the second one is 4 mm, so the concentration is diluted by a factor of 4, to 12.5 mg L^{-1}. In the same way, the concentration of the dye solution in the 8 mm Bethune cell is $1/8^{th}$ of the concentration of the stock solution, giving 6.25 g L^{-1}. These initial concentrations are then optimised according to the amplification power of the pulses from each Bethune cell. Care must be taken when maximising the amplification by increasing the concentration, that the observed power is due to amplification and not amplified spontaneous emission (ASE). ASE occurs when excited dye molecules decay by spontaneous emission before they encounter an incoming photon from the ultrafast pulse train. Consequently a photon is emitted with random phase and direction. A small number of these photons will inevitably end up in the 10

Hz pulse train. To avoid ASE, the concentration is increased very slowly (1 mL portions of the stock solution) and the power measured each time the solution is concentrated. When the ASE reaches 10%, maximising the amplification power any further will compromise the spectral profile of the pulses. The ASE arising from the nanosecond dye laser is marginal but can be minimised, if needed, by adjusting the concentration of the dye as described above.

3.4 TIMING

The timing between all the electronic components of the experimental set-up is critical to the running of the experiments discussed in this thesis. Of particular importance is the timing between the 10 Hz nanosecond Nd:YAG laser used to amplify the output of the ultrafast laser, via the Bethune cells. A pulse generator provides the external trigger for both experiments by generating a 10 Hz TTL pulse[1], effectively setting up the repetition rate for the experiment and providing the reference trigger for all subsequent events. Figure 3.4 is a schematic diagram detailing all the timing triggers in the sodium atom wave packet experiments.

The first step involves mixing the 10 Hz trigger from a Thandar pulse generator with the 38 MHz signal from the picosecond Nd:YAG laser modelocker, in a commercial frequency mixing box (Hatfield 1750). The result is a 10 Hz output signal which is synchronised to the output of the picosecond Nd:YAG laser. This 10 Hz signal triggers the first of a pair of digital delay generators (Stanford Research Systems, DG535). The first DG535 provides a trigger for the 10 Hz nanosecond Nd:YAG laser and also for the second DG535. The second DG535 triggers the pulsed electric field, approximately 70 - 150 ns after excitation, and the digital oscilloscope. It has the added

[1] TTL stands for *Transistor Transistor Logic*, and is used to describe the 5 V square pulse triggers in the experiments.

function of defining the pulsed field length. This pulsed electric is responsible for field ionising all the Rydberg states in the wave packets.

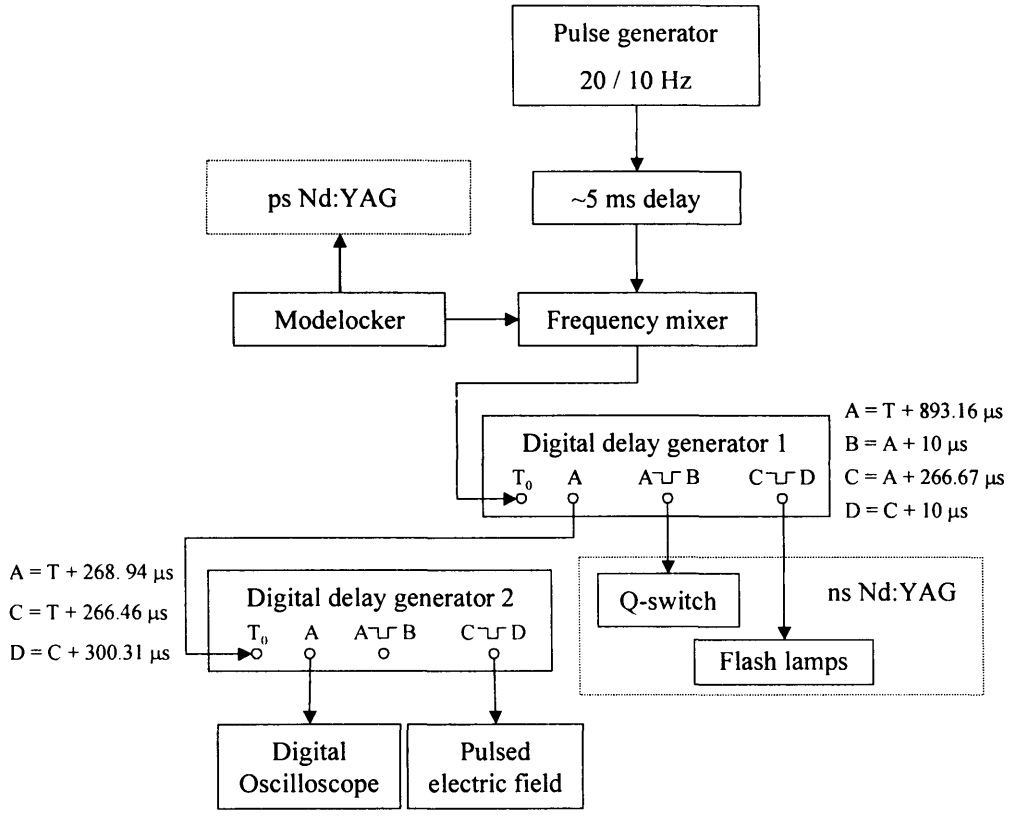

Figure 3.4 Schematic diagram detailing the timing triggers for the Na wave packet experiments. All timing originates from, and is locked to the initial pulse generator. The directions of the arrows indicate which pieces of equipment are acting as triggers, and which are being triggered.

The timing procedure for wave packet experiments in Na_2^+ is still undergoing refinements, although the components of both set-ups are basically the same. The main difference is the replacement of the picosecond Nd:YAG laser and modelocker set-up with the femtosecond Mira Seed laser and a Coherent Pulse Picker (model 9200). The 76 MHz photodiode output signal from the Mira is used as an input signal to the pulse picker, which is capable of producing variable repetition rate pulses by integer division

(from 8 to 520) of the fundamental 76 MHz repetition rate of the Mira. The output from the pulse picker is set to 38 MHz, and this TTL is then combined with a 10 Hz TTL from a Hewlett-Packard function generator, again in a frequency mixing box (Mini Circuits).

3.5 VACUUM APPARATUS

The vacuum chamber employed in all the experiments described in this thesis consists of two sections joined together by a central flange, illustrated in figure 3.5. The section shown on left of figure 3.5 contains the sodium molecular beam source (a sodium oven with a nozzle), and is pumped by a Leybold DIP 3000 L s^{-1} oil diffusion stack pump. The diffusion pump is backed with a Leybold D40B rotary vein pump, and is capable of achieving pressures down to 5×10^{-6} mbar. A Leybold Astrotaurus baffle is mounted above the diffusion pump to prevent oil vapour from the pump entering the vacuum chamber. The end-on view of this part of the chamber is shown in figure 3.5(b). The end flange accommodates two electrical feed-throughs to heat up the sodium oven and the nozzle, and two thermocouple feed-throughs to record the corresponding temperatures. A venting valve is also present, as well as an argon gas feed-through to provide seed gas to the sodium oven. The end flange of this section is illustrated in figure 3.5(c). An additional venting valve is attached to the smaller port so that venting is available to both sides of the chamber if needed. A gate valve (VAT) is positioned between the diffusion pump and the vacuum chamber. It is manually operated, and is used to isolate the diffusion pump from the vacuum chamber.

The "detection-side" of the chamber, shown on the right of figure 3.5, contains a time-of-flight spectrometer and either an electron- or ion multi-channel plate detector. This section is pumped by a Leybold Turbovac 1000 L s^{-1} turbomolecular pump, which is also backed by a Leybold D40B rotary vein pump. An additional, manually operated gate valve (VAT) is positioned between the turbo pump and the vacuum chamber. When the system is cold, the detection-side of the chamber is maintained at around

3×10^{-7} mbar, and the source-side at around 3×10^{-4} mbar. The rotary pumps backing both the diffusion and turbo pumps, maintain pressures of 5×10^{-4} mbar (measured with a Leybold Pirani gauge). When the system is hot (i.e. the temperature of the sodium oven is in the range 250 – 600°C) the rotary pump backing the diffusion pump operates at 2×10^{-2} mbar. The pressure in the detection-side of the chamber is maintained at 5×10^{-7} – 7×10^{-7} mbar and the rotary pump backing the turbo pump operates at 1×10^{-1} mbar. We are unable to accurately measure the pressure in the source-side of the chamber when the sodium oven is hot, due to the corrosive effects of the sodium on the pressure gauge. To protect the turbo pump from the corrosive effects of the sodium, a constant flow of Nitrogen, at approximately 0.5 bar, acts as a purge gas to protect the bearings. The purge gas is regulated so that the pressure at the exhaust of the turbo is approximately 0.1 mbar. An additional protection feature is a cylindrical cold trap, 150 mm in diameter and 200 mm long, positioned in the path of the molecular beam. The trap is suspended from a top flange by two hollow tubes, and is periodically filled with liquid Nitrogen whenever the oven is heated. The surface of the cold trap condenses any sodium in the detection side of the chamber.

Currently, the sodium oven (discussed in detail in section 3.6) is mounted on an *xyz*-translation stage between the two sections of chamber (see figure 3.5(a)). Initially the oven was fitted with a 0.5 mm nozzle and was fixed in the source-side of the chamber, 100 mm from a 10 mm diameter skimmer, which in turn was 180 mm from the interaction region. The oven was surrounded by a stainless steel, water-cooled jacket. This set-up caused endless problems, including oven alignment difficulties, excessive amounts of sodium in the detection chamber and space problems with the water jacket. These were alleviated by moving the water-cooling to the outside of the chamber (in the form of a rubber garden hose), and reducing the nozzle diameter to 100 μm. In addition, the 10 mm diameter skimmer was replaced with a commercial nickel skimmer with a 1 mm aperture. In the present set-up, the nozzle is 5 mm away from the skimmer, which in turn is 93 mm away from the interaction region. The external water-

cooling was found to be perfectly adequate so the temporary garden hose has been replaced with permanent copper tubing.

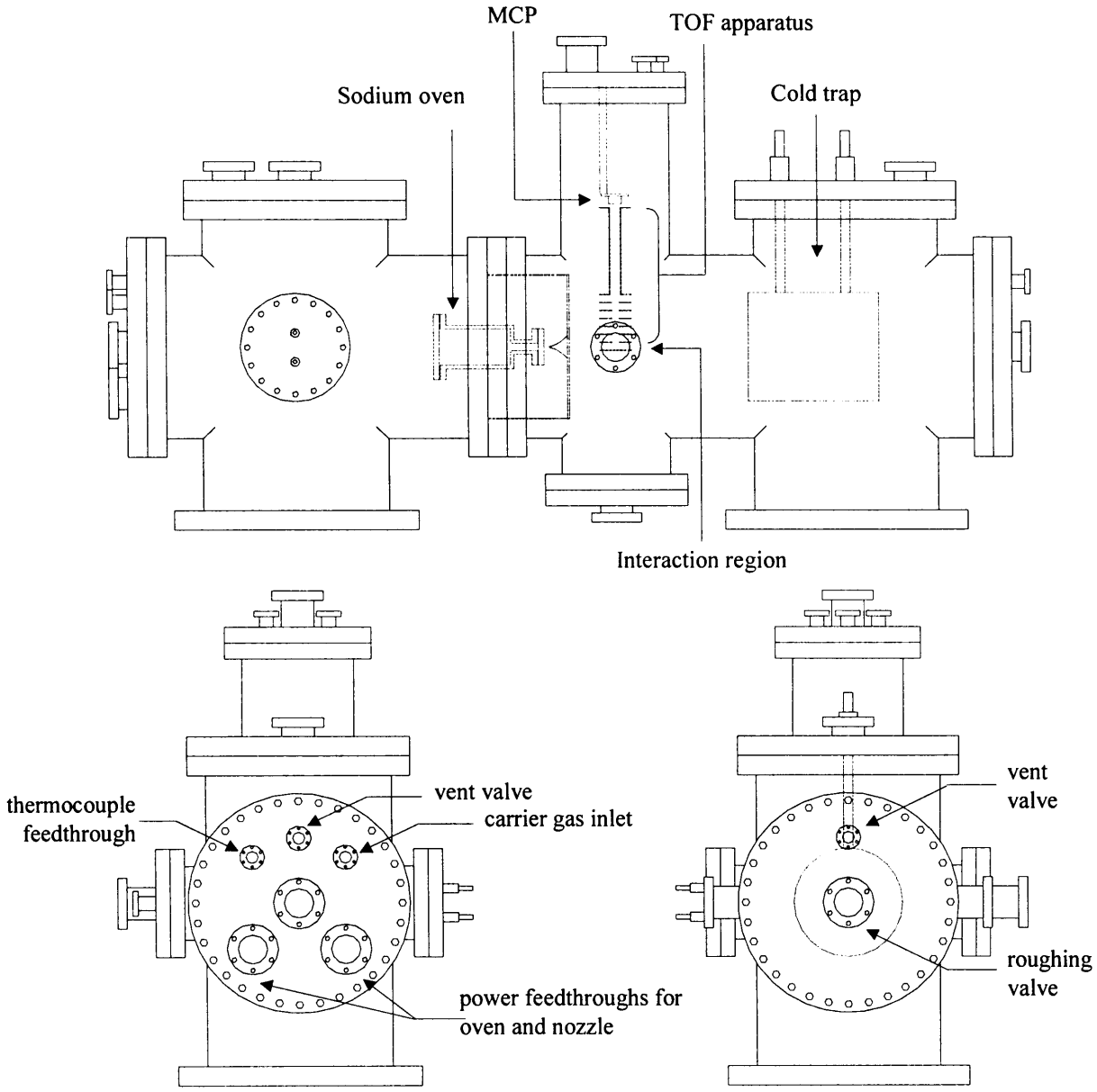

Figure 3.5 Vacuum apparatus set-up for experiments in Na and Na_2. (a) is the side-on view, illustrating the various structures inside the chamber, including the sodium oven, skimmer, time of flight apparatus, MCP and cold trap. (b) and (c) are the two end views of the vacuum chamber, showing the oven and nozzle power feedthroughs, the thermocouple feedthroughs, venting valves and the carrier gas inlet.

The interaction region of the time-of-flight (TOF) apparatus consists of two 60 mm diameter, 1 mm thick stainless steel plates, positioned 10 mm apart. The upper plate has a central, 10 mm diameter hole covered by a 99% transmitting, fine wire mesh. The sodium molecular beam passes through this region and is intersected, at right angles, with the incoming laser beams. Ions or electrons are directed through the hole in the upper plate by applying a pulsed electric field to the solid bottom plate. 10 mm above this field plate is the first of six electron lenses, each separated by 10 mm. A free flight tube is positioned 10 mm higher than the last electron lens, and there is a final electron lens 5 mm above the top of the free flight tube. The ions/electrons pass through the 20 cm field-free time-of-flight apparatus, before being collected at a multichannel plate (Hamamatsu F4566-10 for ion detection and F4566-12 for electron detection), positioned 10 mm above the last electron lens, and attached to the top flange. The entire time-of-flight apparatus is surrounded by a two layers of mu-metal shielding, to protect the ions/electrons from any stray fields in the chamber.

3.6 THE SODIUM OVEN

The sodium oven, illustrated in figure 3.6, is the atom and dimer source in all the experiments described in this thesis. It comprises two independently heated stainless steel cylindrical chambers of different diameters with a nozzle at the end of the smaller chamber. The larger chamber has an inner diameter of 50 mm, into which approximately 5 g of solid sodium is placed. The back door of the oven is simply a Conflat flange with a tube welded into the centre, through which the carrier gas (argon) is introduced. The smaller chamber is responsible for transmitting the seeded sodium to the nozzle. The nozzle comprises a molybdenum disc, 9.525 mm (3/8″) in diameter and 250 μm thick, with a laser-cut, 100 μm diameter hole in the centre. The molybdenum disc is held in place by a modified Conflat flange, 50 mm in diameter, bolted to the end of the smaller oven chamber. The flanges at both ends of the oven are sealed using standard copper gaskets.

Both chambers of the oven are independently heated by separate coaxial resistive heaters[2], wrapped round the outside of each chamber. Initially, the heaters on both sections were supplied and brazed on by Thermocoax. The heater on the larger section of the oven had an outer diameter of 1.5 mm but unfortunately, was not very robust and was subsequently replaced by a 7.9 mm diameter coaxial resistive heater from Farnell. This heater operates at a maximum of 240 V and can heat the oven up to 800 °C. The heater for the smaller section of the oven is 1 mm in diameter, operates at a maximum of 42 V and can achieve temperatures up to 850 °C. Again, this heater was initially brazed on by Thermocoax but was subsequently replaced by an identical heater secured on to the smaller chamber of the oven with a wormdrive hose clip (Jubilee). This set-up not only protects the Thermocoax heater, but also provides a means to secure a thermocouple to record the temperature. The ends of both heating wires are brazed onto ceramic connectors, which are attached to threaded feedthroughs on the back flange of the vacuum chamber.

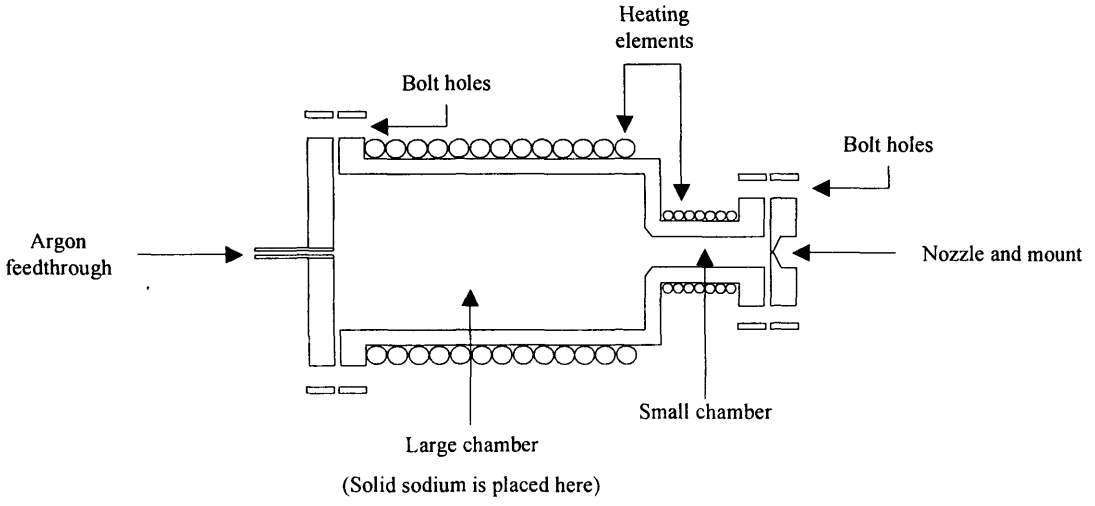

Figure 3.6 Cross-section through the sodium oven. Approximately 5 g of sodium in placed in the main chamber of the oven. The back door comprises a standard conflat flange with a tube welded in the middle to form the carrier gas feedthrough. Appropriately sized heating elements are used for the two sections of the oven. The nozzle is 100 μm in diameter, in the centre of a molybdenum disc secured by another conflat flange.

[2] These particular coaxial resistive heater wires comprise an Inconel (nickel-chromium-iron) core and an outer sheath separated by compacted MgO powder.

Power is supplied to the two oven heaters via variable transformers powered by the mains (240 V), and measured on a voltmeter connected in parallel. Each section of the oven has a thermocouple attached near the centre of the heater to monitor the temperature. The thermocouples are K-type, formed by a Chromel and Alumel[3] junction, and have a temperature range of -200 °C to +1200 °C. The thermocouple wire extends from the oven for approximately 50 cm. The ends of the wire are fitted with the pins from a standard miniature thermocouple plug, and the corresponding plug is connected to a feedthrough on the back flange of the chamber.

To determine the oven and nozzle temperatures using thermocouples, one has to measure the voltage generated when two dissimilar metals are in contact (in the case of K-type thermocouples, these are Chromel and Alumel as mentioned above). The temperature is found by comparing the measured potential, obtained from the voltmeter reading, against the known behaviour of the thermocouple [4] (see figure 3.7(b)). However, simply measuring the voltage across a thermocouple is not entirely accurate, as the connection formed when two thermocouple wires connect to the voltmeter is itself a thermocouple, and will therefore create a constant error in the voltage reading. To obtain this error and effectively calibrate the thermocouples, the voltage difference between two like ends of the two thermocouples was measured, whilst the end of one was attached to the oven and the end of the other was held in iced water (this creates a 'double' thermocouple). True thermocouple reading are obtained with reference to one thermocouple held at a constant temperature of 0°C [4]. Figure 3.7(a) is a plot obtained when the measured voltage of the double thermocouple (held at 0°C) is plotted against the measured voltage of the oven thermocouple (the single thermocouple). Through the gradient, we can accurately obtain the temperature of the oven. For example, if oven thermocouple gives a reading of 10 mV, the actual voltage is 11.03 mV. Figure 3.7(b) is a plot of tabulated thermocouple data from [4]. The temperature that corresponds to a particular voltage is obtained with use of the gradient. In the example presented above, a voltage of 11.03 mV corresponds to a temperature of approximately 273°C.

[3] Chromel is a chromium and nickel alloy, and Alumel is an aluminium and nickel alloy.

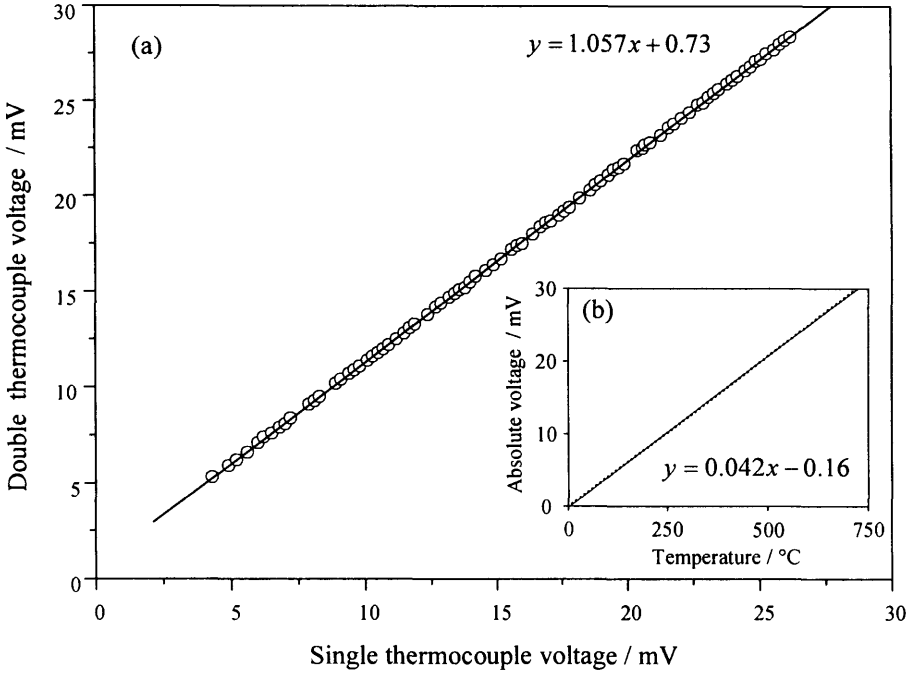

Figure 3.7 Graph (a) is a plot of the voltage obtained from heating a double thermocouple (with one end in iced water at 0°C) verses the voltage obtained from heating a single thermocouple (the oven thermocouple). The gradient provides us with an accurate measure of the voltage of the oven thermocouple. Graph (b) is a plot of tabulated thermocouple data from [4], which is used to convert the voltage reading to temperature.

3.7 THE STABILISED INTERFEROMETER

The wave packet control experiments discussed in this thesis all rely on the generation of identical pulses to create two or more wave packets with a well-defined phase difference between them. To monitor the time-evolution of the wave packet, the optical Ramsey method [5] is employed. The theory behind this method was introduced in chapter 2 and the experimental details are explained in section 3.8.1 of this chapter. A complementary detection technique, which enables us to determine the population amplitudes of the eigenstates in a wave packet, is state selective field ionisation. The concepts and experimental details of this method are discussed in section 3.8.2.

The crucial element of the control experiments presented in this thesis is the ability to create phase-locked optical pulses, and to control the exact time delay between each pulse in the sequence. This is implemented experimentally with the use of a Michelson interferometer. In this set-up, the incoming pulse is split into two identical parts at a 50% beamsplitter, as shown in figure 3.8.

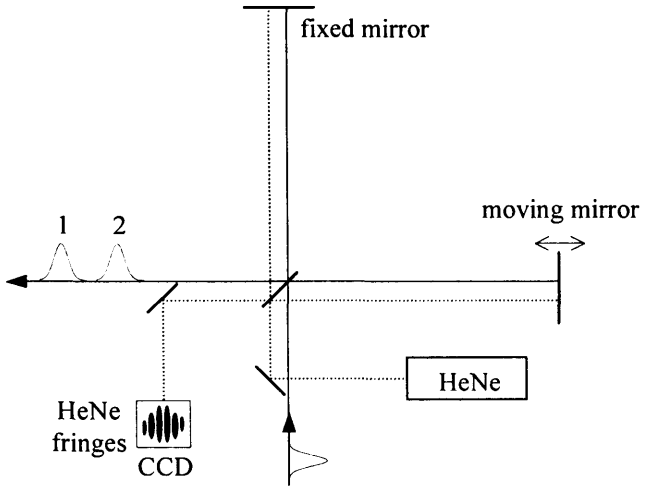

Figure 3.8 Schematic diagram of a single Michelson interferometer used to create a pulse pair with a well-defined phase difference. The incoming beam is split at a 50% beamsplitter. The moving arm allows a delay to be created between the pulses. The stabilisation set-up is also shown.

The difference between the path lengths of the two arms of the interferometer determines the phase difference of the wave packets; it is achieved by allowing one arm to move while the other arm remains in a fixed position, which generates a temporal delay between the optical pulses. A typical path length difference of the interferometers used in our experiments is approximately 30 μm, which corresponds to a delay between the two optical pulses of 0.2 ps. Coarse adjustments to the path length are made with a linear translation stage (Physik Instrumente M-510), which moves in steps of around 20 μm while fine adjustments are made with a piezoelectric actuator (Physik Instrumente P-780) bolted on top of the translation stage, and with the interferometer mirror bolted to it. The piezo is capable of moving in step sizes of 10 nm.

Low frequency vibrations of the optics or optical table could alter the phase of the combined pulses, so to counteract any external low-frequency external vibrations, the interferometer is continuously stabilised with an analogue stabilisation circuit. The interferometer is stabilised with reference to the interference pattern generated by a continuous wave HeNe laser as it travels parallel to the excitation pulse, through the interferometer (see the laser table set-up in figure 3.3). The interference fringes generated by the HeNe laser (Carl Zeiss Jena LGK7628) are monitored on an analogue charge coupled device (CCD) array (Loral CCD181DB), where four to five fringes are monitored across 1064 pixels. The interference fringes generated by the HeNe laser act as a reference signal for a proportional integral derivative (PID) feedback circuit, which generates an error signal whenever the fringes deviate from the reference position [6]. This error signal aims to retain the reference position by generating a voltage, which is sent to the piezo on which the mirror of the moveable arm is mounted. The voltage moves the piezo in the appropriate direction thereby generating a path-difference equivalent to the reference value. The stabilisation circuit allows the piezo to take very accurate steps, which are much smaller than the wavelength of the excitation field, whilst providing temporal stability of the delay between the pulses. The stabilisation circuit has a response time of approximately 10 ms and can stabilise path length fluctuations in the interferometer of up to 15 nm [6].

The coherent control schemes presented in this thesis are based on the excitation of sequences of phase-locked pulses. To detect the resultant wave packet created after a sequence of pump pulses, the interference is monitored, as before, with a single probe pulse, using the optical Ramsey method (section 3.8.1). The use of two pump pulses requires a total of three optical pulses, which are all phase-locked to each other, but which also have independent, variable delays between them. This is achieved in our laboratory using a three-armed Michelson interferometer, which was integrated into the original stabilised Michelson interferometer, by inserting a third arm into the existing fixed arm as shown in figure 3.9.

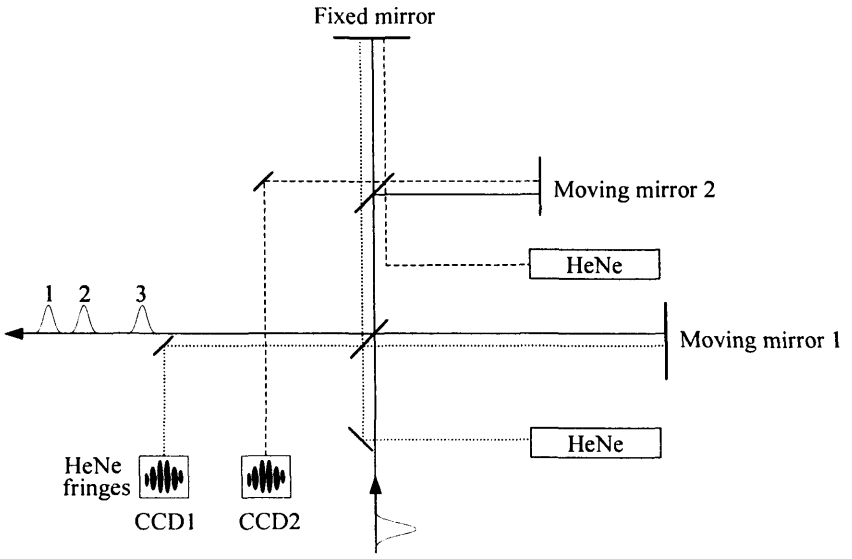

Figure 3.9 The double interferometer is employed in the coherent control experiments. The path length of the smaller, nested interferometer determines the delay between the two control pulses. The large interferometer generates the probe pulse. Both arms are stabilised against vibrations of the optics or optical table. The nested interferometer is stabilised by a digital stabilisation circuit, whilst an analogue system stabilises the original interferometer. Both piezos derive their signals from a feedback loop using interference fringes from a HeNe laser monitored on a digital camera or an analogue CCD array.

The nested interferometer is responsible for generating the control pulses whilst the existing, larger interferometer generates the probe pulse. In the control arm of the nested interferometer, coarse adjustments to the path length are made with a linear translation stage (Physik Instrumente P510.12) while fine adjustments are made with a piezoelectric actuator (Physik Instrumente P753.31C) bolted on top of the translation stage, and with the interferometer mirror bolted to it. The translation stage is controlled using National Instruments LabView program via an ISA card (Physik Instrumente C842) in a PC, whilst the piezo is powered with a x10 voltage and current amplifier (Physik Instrumente E501).

To ensure that the three optical pulses emerging from the interferometer have similar intensities, the mirrors on the two moving arms and the one fixed arm are chosen with specific reflectivities. With reference to figure 3.9, the laser beam enters the

bottom of the interferometer and hits a 50% beamsplitter. Half of the beam is reflected to a 25% reflecting mirror mounted on a piezo (moving mirror 1), which in turn is mounted on a motorised translation stage. The remaining 50% of the beam is transmitted and hits a second 50% beamsplitter, which again reflects half the beam onto a similarly mounted 100% reflecting mirror (moving mirror 2). The remainder of the beam (which is now a quarter of the strength of the original beam) is transmitted onto a 100% reflecting fixed mirror. The three pulses are then recombined at the first beamslitter and they exit the interferometer with only one sixteenth of the original pulse energy as both interferometers loose three quarters of the input pulse.

It is necessary for all three of the pulses to be phase-locked with each other, so the one fixed arm is used as reference for all the stabilisation. This is achieved in essentially the same way as with the single interferometer but now, two HeNe lasers are incorporated to stabilise each arm individually. Stabilisation of the nested interferometer is achieved with the analogue stabilisation circuit discussed above. The larger interferometer is stabilised with a digital stabilisation circuit [7], using the same approach as described above: The interference fringes generated by a HeNe laser (Plasma - 303) act as a reference signal for a proportional integral derivative (PID) feedback circuit, which generates an error signal whenever the fringes deviate from the reference position. The HeNe fringes are collected on a CCD array with 1024 pixels and 8-bit resolution per pixel (Basler L101-k). This stabilisation circuit can stabilise path length fluctuations in the interferometer of as low as 4 nm [7]. The two control pulses, generated by the nested interferometer, are stabilised by the analogue stabilisation circuit on account of its superior long-term stability. Long-term stability is imperative when stabilising the second control pulse, which needs to stay phase-locked for the entire coherent control experiment (sometimes in excess of 12 hours). The digital system, whilst able to stabilise with superior accuracy, is not as effective when required to stabilise for long periods of time. Therefore, this system is used to stabilise the probe pulse, which is only required to remain phase-locked for the time it takes for the piezo to take 40 steps (a typical number in a wave packet experiment).

3.8 WAVE PACKET DETECTION

3.8.1 THE OPTICAL RAMSEY METHOD

The optical Ramsey Method [5] is used to monitor the time evolution of a wave packet, and the underlying theory has been discussed in detail in the previous chapter. We use this method to monitor wave packets created by a single laser pulse, or from a sequence of laser pulses, using either the single or double interferometer, both described above. The following sub-sections describe how the optical Ramsey method is implemented experimentally in single and multi-wave packet excitation.

In section 3.6, the stabilised Michelson interferometer was introduced. Here, a laser beam enters the interferometer and a pair of phase-locked light pulses exits. In the terminology of the optical Ramsey method, the first light pulse to leave the interferometer is the 'pump' pulse, and will couple the initial ground state population $|g\rangle$ to the Rydberg states $|n\rangle$ by creating Rabi oscillations between the levels. In the weak field limit, the population of the ground state is not depleted, and the frequency of the oscillations matches the optical frequency. The second pulse to exit the interferometer is the 'probe' pulse, which creates a second, virtually identical wave packet that has a well defined phase difference to the first, and can therefore interfere with it. It is assumed that the second 'probe' wave packet does not have time to move and only exists at the core. Consequently, the degree of interference between this wave packet and the initial pump wave packet can be determined by the spatial overlap of the two wave packets. The total Rydberg population is therefore a direct reflection of this interference between the pump and probe wave packets, so it is possible to tell when the original wave packet is in the vicinity of the core, and to what extent it has dispersed or rephased. If the pump and probe wave packets overlap spatially and are in phase, the result is constructive interference; the wave packet amplitudes add together and consequently the coherent Rydberg population is four times as large. If the wave

packets overlap but are out of phase, the amplitudes cancel each other out and the result is zero Rydberg population. Alternatively, if there is no spatial overlap at all between the two wave packets, there is no interference and the incoherent Rydberg population is double created by a single pulse.

To apply the optical Ramsey method the interferometer, as described in section 3.6, is used. The evolution of an electron wave packet is typically in the picosecond regime, so in order to track the dynamics by scanning through the phase difference between the pump and probe pulses, steps of 40 nm for 3 cm (equivalent to 0.2 ps steps for 200 ps) would be necessary. In practice, this type of precision is impractical and means that the data collection process would be very lengthy. The data collection time is significantly shortened through the use a piezo mounted on the motorised translation stage. The translation stage takes coarse steps of approximately 30 μm (corresponding to 0.2 ps delay between the optical pulses). Once the translation stage has moved one coarse step, the piezo is stepped through 3 – 4 optical cycles (this corresponds to a step size of approximately 40 nm – depending on wavelength of the laser pulse). During this movement of the piezo, the ion signal is recorded. The translation stage is then moved another 30 μm and the piezo again stepped over a few optical cycles. At each step of the piezo, the ion signal is recorded through a digital oscilloscope, integrated and averaged, typically over 5 – 10 laser shots. Consequently, one time spectrum my take up to three hours to generate.

In figure 3.10, the raw data (a) collected in a typical optical Ramsey experiment in Na is presented, with the corresponding wave packet recurrence spectrum (c). Figure 3.10(b) shows 4 fringes, collected over 40 piezo steps. Sections of raw data from each set of 40 piezo steps are filtered using a Mathematica program, which is designed to fit a sine wave with a defined frequency to each section of raw data. The root mean square of this sine wave is then used to define the autocorrelation value at the specific time delay, given by the coarse steps of the translation stage. The resultant recurrence spectrum is shown in figure 3.10(c).

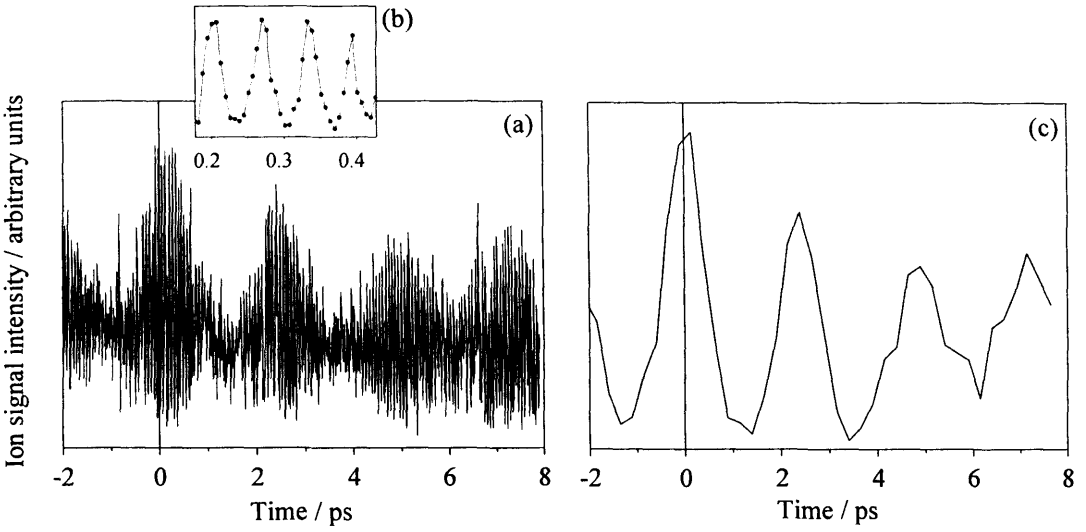

Figure 3.10 Plot (a) is an sample of the raw data collected in a typical wave packet experiment. In this example, a wave packet was excited in Na with average energy centred around n = 30, with a 0.7 ps laser pulse. The translation stage is moved in coarse steps of 30μm, which corresponds to a delay between the pulses of 0.2 ps. For each coarse delay, the piezo moves 40 steps at approximately 40 nm/step, shown in inset (b). Interference fringes recorded by the piezo, as in this example, are indicative of the wave packet's presence in the core region. Plot (c) is the recurrence spectrum obtained from fitting a sine wave to the raw data in (a). In this example, the wave packet has a classical period of approximately 2.5 ps.

A purpose-designed LabView program [7] provides detailed control over the variables required in an optical Ramsey experiment. The user has control over the number of steps, and step size of the translation stage and the piezo, as well as the number of laser shots the data is averaged over. Various oscilloscope settings including time base, voltage scale and trigger level, are also controllable from the LabView interface.

The coherent control experiments described in this thesis all rely on the interference effects induced by particular phase differences between two, or more, wave packets. In this coherent control method, a wave packet is created, and allowed to evolve to a distinct point in its evolution. For example, in one of the coherent control experiments presented in chapter 5, the first wave packet is allowed to evolve for 1.5 classical orbit periods (9.22 ps for an electron wave packet in sodium, centred around n

= 35). This is achieved experimentally by setting the interferometer path length so that the pulses exiting the interferometer are separated by 9.22 ps, ensuring the second wave packet is excited when the first has evolved for $1.5T_{cl}$. This coarse movement of the path length is carried out with one translation stage. By stepping the piezo on top of the same translation stage, the second wave packet is scanned through the first wave packet an amount equal to one oscillation of the optical cycle, λ (in the present example, λ is the wavelength of the transition from the $^2P_{3/2}$ intermediate state to the $d(n = 35)$ Rydberg state in sodium) in steps of approximately $\lambda/20$. Each tiny step of the piezo alters the phase between the wave packets, resulting in a modulation in the Rydberg state population. The resultant wave packet is allowed to evolve for a specified time (one that allows the components of the wave packet to rephase – a partial revival for example), before a third wave packet is launched to probe the dynamics.

An important factor in these experiments is knowledge of the exact value of the phase difference between the wave packets. Returning to the example discussed above, if the second wave packet is launched 9.22 ps ($1.5\ T_{cl}$) after the first, the translation stage is moved 1.38 mm, with an error of ± 17 nm. Therefore, the second wave packet will be phase shifted relative to the first before the first step of the piezo, and there is no accurate way of knowing the exact phase between the wave packets. To determine a precise value of the phase shift, and to ensure that the two wave packets are shifted completely through λ, the following procedure is followed each time a coherent control experiment is carried out: A series of fringes are collected at $t = 0$ in an optical Ramsey experiment, for a known number of piezo steps. A set of electron fringes collected around $t = 0$ for 120 piezo steps are presented in figure 3.11, for an electron wave packet excited around $n = 35$ in the sodium atom. There are 10.5 fringes in this plot (a sine wave has been fitted to the data to accurately determine the number of fringes).

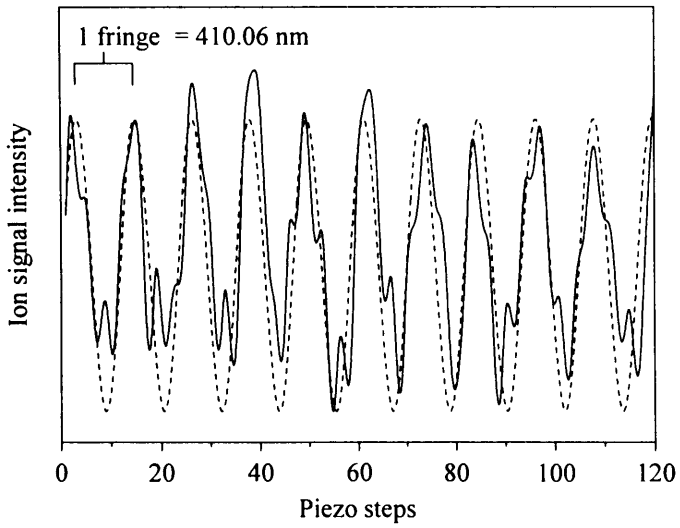

Figure 3.11 Optical Ramsey fringes in the region of t = 0 for an electron wave packet excited around n =35 in the sodium atom. In this data set there are 10.5 fringes, where each fringe represents one optical cycle, λ, where λ = 410.06 nm. The fringes result from 120 piezo steps. A sine wave is fitted to the data to accurately obtain the number of optical cycles. This type of plot is used to ascertain the number of piezo steps required to completely scan the phase difference between the two wave packets through one optical cycle.

In this example (as above) λ = 410.06 nm and there are 10.5 fringes, each corresponding to one optical cycle, the total path length moved by the translation stage and piezo is 4305.66 nm. The piezo has moved 120 steps, so the amount moved by the piezo is 35.88 nm step^{-1}. The final stage is to ascertain how many steps the piezo has to take to ensure the two wave packets are scanned through one complete oscillation of the optical cycle. If the piezo moves at 35.88 nm step^{-1} and the optical cycle is 410.06 nm, then each steps corresponds to 0.175 π step^{-1}, where $\pi = \lambda/2$. Therefore, the piezo has to take at least 11 steps to ensure that the wave packets are scanned through one optical cycle. After each piezo step, an optical Ramsey experiment is run to obtain a wave packet recurrence spectrum. After a sequence of steps running though λ, the recurrence spectra are compared to theoretical spectra to determine the absolute value of the phase difference. It is imperative that the interferometer is not disturbed during a coherent

control experiment, as each piezo step is only meaningful when it is in sequence of steps that scan through λ.

3.8.2 STATE SELECTIVE FIELD IONISATION

Whilst the optical Ramsey method provides information about the phase evolution of the wave packet, the population amplitudes, a_n of the eigenstates in the wave packet are not directly accessible. A direct analysis of the wave packet amplitude can be obtained using state selective field ionisation (SSFI) [8], which has been widely used as an experimental tool to measure the character and population of highly excited states of atoms and molecules (for examples, see refs. [9,10]). In this method, the atoms or molecules are subjected to a ramped electric field over a time period longer than the classical evolution of the system. The electric field induces a saddle point in the Coulomb potential at an energy, in wavenumbers, of

$$E = -6.12\sqrt{F}\ , \qquad (3.1)$$

where F is the electric field in $\mathrm{Vcm^{-1}}$. As the field ramps to higher strengths, the barrier to ionisation is lowered slowly and, as the contributing Rydberg states have different energies they ionise, and reach the MCP at different times (illustrated in figure 3.12). Consequently, the time of detection at the MCP marks the field at which the states ionise, which is then a measure of the energy of each state in the wave packet before ionisation.

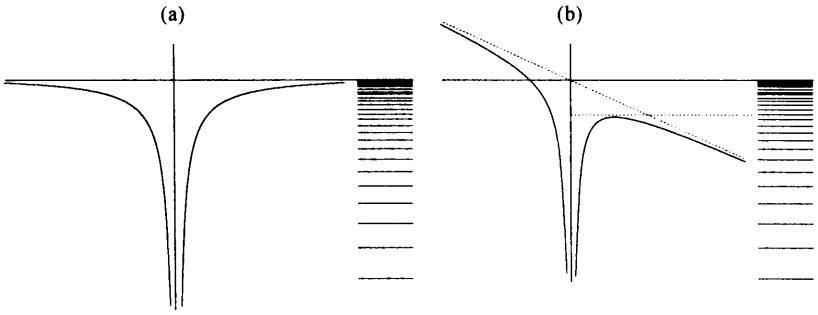

Figure 3.12 Schematic diagram showing the Coulombic potential of an electron in (a) the absence of a field and (b) in the presence of a field along the z-axis. If a given Rydberg state is initially populated in the absence of an electric field, and switching on a field lowers the ionisation energy below the energy of that particular state, the Rydberg electron will change from being bound to unbound and will field-ionise.

In an electric field, atomic Rydberg energy levels lose their degeneracy and split into a manifold of states, the number of which depends on the value of the principal quantum number, n [11]. As a result of the density of states in Rydberg systems, it is common for these manifolds to overlap and perturb one another, forming a series of avoided crossings. These pathways can be visualised if the energy of each state is plotted against the increasing strength of the applied field; this type of plot is known as a Stark map. In traversing the Stark map from zero field to ionisation, a particular Rydberg state encounters many avoided crossings which can be traversed adiabatically or diabatically.

The probability of traversing an isolated avoided crossing, diabatically is given by the Landau-Zener approximation [12]

$$P_{diabatic} = \exp\left(-2\pi \frac{|V_{12}|^2}{\hbar(\mathrm{d}W_{12}/\mathrm{d}t)}\right) \tag{3.2}$$

where V_{12} is the coupling matrix element of the interaction that is responsible for the avoided crossing between levels 1 and 2, and W_{12} is the energy difference between the

two states. The slew rate of the field can be expressed by rewriting the time derivative as

$$\frac{dW_{12}}{dt} = \dot{F}\left|\frac{dE_1}{dF} - \frac{dE_2}{dF}\right| \tag{3.3}$$

where $\dot{F}$ is the slew rate of the field, and the dE/dF terms are the slopes of the two states involved in the crossing. From (3.2) it is possible to calculate the probability that a particular state will cross each avoided crossing in the Stark map diabatically, for a particular slew rate of the field. It is apparent that, for a given energy separation, the slower the field is ramped, i.e. the slower the slew rate, the lower the probability of a diabatic crossing. The SSFI experiments on sodium wave packets, discussed in chapter 5, are all carried out by ramping an electric field from 0 to 1000 V, at a slew rate of approximately 700 V cm^{-1} μs^{-1}. In sodium Rydberg wave packets, this results in predominantly adiabatic crossings across the Stark map, for all states in the wave packet.

To carry out the SSFI experiments, modifications were made to the high voltage pulser (DEI PVX-4140) to produced a ramped electric field. This pulser is specified to pulse high voltage electric fields with a rise time[4] of ≈25 ns, which effectively ionises all the Rydberg states in a wave packet simultaneously. In an SSFI experiment, a rise time on the order of microseconds is required so that the Rydberg states are ionised sequentially and separated in time sufficiently that they may be resolved on an oscilloscope. This was achieved by adding a series resistor (14.53 kΩ) to the output of the pulser, which increased the rise time to approximately 2.3 μs. The modifications are illustrated in figure 3.13.

[4] The rise time is typically defined as the time it takes for the voltage to rise from 10% to 90% of its maximum.

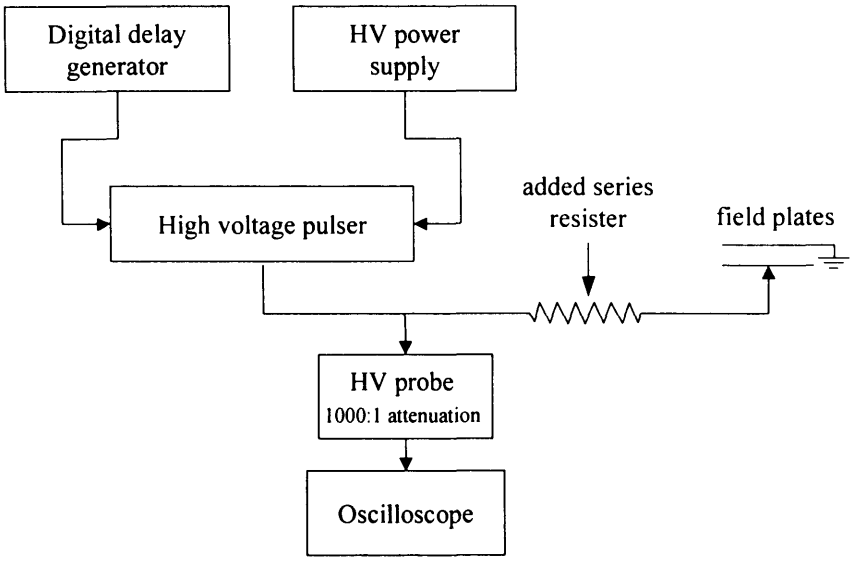

Figure 3.13 Schematic diagram showing the modifications to the high voltage pulser. A series resistor was added to the output of the high voltage pulser to increase the rise time of the pulse to around 2.3 μs.

The details of the laser setup are as described in section 3.2.1 of this chapter and in more detail in chapter 5. Briefly, the translation stage in a single Michelson interferometer is set to generate two wave packets separated by one classical period. The first time the wave packet returns to the core is after one classical period, and following this, at the partial revivals. If the wave packet is in the core region, excitation of a second wave packet provides an opportunity for interference to occur. Scanning the phase of the second wave packet results in a modulation in the Rydberg state population. This is achieved experimentally by altering the path length of the interferometer by a distance corresponding to one oscillation of the optical cycle, in steps of approximately $\lambda/20$, where λ is ps laser wavelength. The detected signal generated by each laser shot was viewed on a digital oscilloscope and collected on a PC. For each piezo step, the signal was summed over 1000 laser shots.

A sample of the raw data collected from a typical SSFI experiment is presented in figure 3.14.

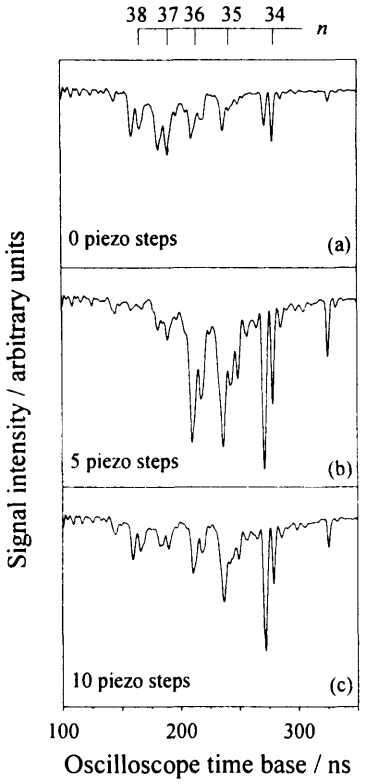

Figure 3.14 Raw data from a typical SSFI experiment in Na. The wave packet was excited from the $^2P_{3/2}$ intermediate state of Na to around n = 35, with a 0.7 ps laser pulse. A second wave packet was launched at t = 6.5 ps, by moving the translation state the equivalent distance, to coincide with the first recurrence to the core of the original wave packet. The piezo was stepped 15 times, with a step size approximately 1/14 of the optical cycle. At each piezo step, the signal was viewed on an oscilloscope, averaged over 1000 laser shots and collected on a PC running LabView. Plot (a) is the SSFI trace before the piezo started stepping, plot (b) and (c) are traces after 5 and 10 piezo steps respectively.

In this example, a wave packet was excited around n = 35 in the sodium atom, with a laser pulse whose bandwidth was 21.01 cm^{-1} (which corresponds to a 0.7 ps bandwidth limited laser pulse). After 6.5 ps (one classical period) a second wave packet was launched. The piezo was then moved a total of 14 steps, each equaling approximately $\lambda/14$. Each step of the piezo alters the phase between the two wave packets, resulting in a modulation in the Rydberg state population. After each piezo step, the ion signal was viewed on a digital oscilloscope. A LabView program, specifically designed for these experiments, collects the signal from the oscilloscope,

sums the data over 1000 laser shots, and writes the output to file. The step size of the piezo, the number of steps and the relevant oscilloscope functions (voltage scale, timebase etc.) are all controllable from the LabView interface. An example of a typical SSFI experiment is presented in figure 3.14 for (a) zero piezo steps, (b) 5 peizo steps and (c) 10 peizo steps. Each peak in the signal represents a Rydberg state in the wave packet. By changing the relative phase of the two laser pulses, the population amplitude of the individual states can be controlled.

3.8.3 PROPOSED DETECTION METHOD FOR WAVE PACKETS IN Na_2^+

In section 3.2 of this chapter, the laser set-up for a proposed experiment was described, which involved the investigation and control of vibrational wave packet dynamics in Na_2. With these experiments, it was hoped that we could implement a new technique for exciting and observing vibrational wave packet dynamics on the ionic potential surface, by combining the methods of phase-modulated detection and zero kinetic energy spectroscopy – pulsed field ionisation (ZEKE-PFI) [13]. Unfortunately the wave packet experiments in Na_2 have not been successful. However, due to the amount of work that has been undertaken to reach this conclusion, this section on the proposed detection technique is included, which also explains the motivations for the work and provides a basis for the theoretical calculations carried out in chapter 4.

The majority of vibrational wave packet experiments take place in neutral molecules, probably the most famous examples being the work of Zewail [14,15] on several molecules containing iodine (e.g. I_2, ICH, ICN and INa). The only experiments on ions have taken place in the gas-phase and involve probing and controlling the products of photo-fragmentation for example, via multi-photon ionisation [16,17] as opposed to investigating the dynamics of the wave packet on the ionic potential surface.

The basic outline of the proposed scheme involves using a broad bandwidth femtosecond laser to excite a coherent superposition of several vibrational states of the

Na_2^+ ion, along with their corresponding Rydberg series. The resultant wave packet will evolve in both the electronic and vibrational coordinate. At a later time, a second wave packet is excited which is phase-locked to the first (using the same interferometer set-up described in section 3.7). The two wave packets will then interfere, providing a measure of the autocorrelation function. The magnitude of the autocorrelation function will depend on both the delay between the laser pulses and the precise phase difference between them, as these two variables are responsible for the two wave packets interfering constructively or destructively. It was hoped that the interference would have been visible as modulations in the total excited state population. We had hoped to observe these modulations by applying a pulsed electric field, some time after both wave packet excitations had taken place, to ionise the Rydberg state population. Using a very small pulsed electric field, typically a few Vcm^{-1}, only the highest lying Rydberg states would be ionised. By collecting these electrons alone, it should have been possible to filter out the beating between the bunches of Rydberg states converging to the various vibrational ionisation limits from the beating between adjacent Rydberg states [18], thereby extracting the vibrational dynamics and providing a novel way of observing the vibrational wave packets on an ionic potential surface.

3.9 DATA COLLECTION AND ACQUISITION

The method of translating the detected ion signal into data is equivalent for both the frequency and time resolved experiments in Na and the frequency resolved experiments in Na_2. After interaction with the laser beam, ions or electrons are directed through a hole in the upper field plate of the interaction region by applying, to the bottom field plate, a 2 kV pulsed electric field from a high voltage power supply (Stanford Research Systems PS350) connected to a high voltage pulser (DEI PVX-4140). This pulsed voltage is applied 70 - 150 ns after laser excitation. The ions / electrons pass through a 20 cm field-free, time-of-flight apparatus, before being collected at an appropriately

biased multichannel plate (Hamamatsu F4566-10 for ion detection and F4566-12 for electron detection), positioned on the top flange of the vacuum chamber. The voltage to the MCP is supplied by a second high voltage power supply (Stanford Research Systems PS230).

The ion signal from the MCP is amplified by a fast timing pre-amplifier (EG&G Ortec VT120C) and is then transferred to a 500 MHz oscilloscope (LeCroy LT372), via a standard BNC cable. The maximum resolution of the oscilloscope is 2 ns and a typical signal has a full-width-half-maximum (FWHM) of 10 ns in Na and 50 ns in Na_2. The data is transferred from the oscilloscope to a PC running LabView through a general-purpose interface bus (GPIB).

3.10 SUMMARY

This chapter has provided the details of the experimental equipment and techniques used to excite electronic wave packets in Na and the set-up for the proposed experiment for the excitation and control of vibrational wave packets in Na_2^+. Both approaches are based on a two step excitation, where an intermediate state is accessed with a narrow-bandwidth nanosecond laser and wave packets are created with a broad bandwidth, ultrafast laser. The relative successes of both approaches have been discussed.

A new vacuum apparatus and sodium source were constructed, and employed for all the experiments in this thesis. The set-up of the vacuum chamber has been described in detail, along with some of the problems it has presented and the corresponding solutions. The details of the sodium oven are discussed, including the various modifications it has endured and how the temperature measurements are obtained.

Attention has been given to the complementary detection techniques of the optical Ramsey method, for monitoring the time-evolution, and state selective field ionisation, for detection of the probability amplitudes of Rydberg electron wave packets

in Na. This includes a detailed discussion of the stabilisation of the interferometer and also, a new method for determining the relative phase shifts that the wave packets undergo in our control experiments.

Finally, a new technique for monitoring vibrational wave packets on the ionic potential surface has been described, in order to convey some of the original motivations for the experiments in sodium the theoretical control schemes presented in chapter 4.

3.11 REFERENCES

1. W. Demtroder, *Laser Spectroscopy*. Springer, 1996.
2. A. C. Effantin, A. O. Babaky, A. K. Hussein, A. J. d'Incan, and A. R. F. Barrow, *J. Phys. B-At. Mol. Opt. Phys.* **18**, 4077 (1985).
3. D. S. Bethune, *App. Opt.* **20** (11), 1897 (1981).
4. *CRC Handbook of Chemistry and Physics*, 1st student edition ed. CRC Press, 1988.
5. L. D. Noordam, D. I. Duncan, and T. F. Gallagher, *Phys. Rev. A* **45** (7), 4734 (1992).
6. Q. Hong, J. A. Ramswell, V. G. Stavros, C. J. Barnett, and H. H. Fielding, *Meas. Sci. Technol.* **9** (3), 378 (1998).
7. J. R. R. Verlet, PhD ThesisPhD Thesis, King's College London, 2003.
8. T. F. Gallagher, L. M. Humphrey, W. E. Cooke, R. M. Hill, and S. A. Edelstein, *Phys. Rev. A* **16** (3), 1098 (1977).
9. K. Muller-Dethlefs, M. Sander, and E. W. Schlag, *Chem. Phys. Lett.* **112** (4), 291 (1984).
10. L. G. Gray and K. B. Macadam, *J. Phys. B-At. Mol. Opt. Phys.* **27** (14), 3055 (1994).

11. G. Herzberg, *Atomic Spectra and Atomic Structure*. Blackie & Son Limited, London and Glasgow, 1937.

12. J. R. Rubbmark, M. M. Kash, M. G. Littman, and D. Kleppner, *Phys. Rev. A* **23** (6), 3107 (1981).

13. F. Merkt, *Annu. Rev. Phys. Chem.* **48**, 675 (1997).

14. A. H. Zewail, *Femtochemistry: Ultrafast Dynamics of the Chemical Bond, Vol. 1*. World Scientific, 1994.

15. A. H. Zewail, *Femtochemistry: Ultrafast Dynamics of the Chemical Bond, Vol. 2*. World Scientific, 1994.

16. A. Assion, T. Baumert, J. Helbing, V. Seyfried, and G. Gerber, *Chem. Phys. Lett.* **259** (5,6), 488 (1996).

17. T. Baumert, B. Buhler, M. Grosser, R. Thalweiser, V. Weiss, E. Wiedenmann, and G. Gerber, *J. Phys. Chem.* **95** (21), 8103 (1991).

18. V. G. Stavros and H. H. Fielding, *J. Chem. Phys.* **112** (21), 9343 (2000).

CHAPTER 4:

OPTICAL CONTROL OF THE QUANTUM-STATE DISTRIBUTION OF VIBRATIONAL WAVE PACKETS IN Na_2^+

This chapter describes an intuitive scheme for controlling the quantum state distribution of one-coordinate molecular wave packets. The control is achieved by exploiting the phase-evolution of the constituent vibrational quantum states. By determining the phase relationship and the accumulated phase difference between the various components of the wave packet, a sequence of phase-locked optical pulses is designed in order to selectively enhance or depopulate specific vibrational states, or sets of vibrational states. The quantum state composition of the resulting wave packet, and the efficiency of the control scheme, is determined by calculating the multi-pulse response of the time-dependent vibrational state populations.

4.1 INTRODUCTION

In this chapter, the phase-evolution of vibrational wave packet quantum states I sexplored and subsequently, the role of phase in the control of vibrational wave packet dynamics. An understanding of the phase-evolution of the individual components of a wave packet is integral to the design of intuitive coherent control strategies. Accordingly, it is shown that it is possible to predict sequences of optical pulses which are capable of selectively enhancing or depopulating specific vibrational states or sets of vibrational states.

The use of coherent laser radiation to control photochemical reactions is a major goal in the field of chemical physics. Significant advances in laser and optical technology, theoretical methodology and computational power during the last decade mean that we are now well equipped with the right tools to realise this goal.

Briefly, coherent control involves engineering the temporal or spectral characteristics of laser light to generate quantum interferences, which result in a preferential enhancement of one product over another. There is more than one approach to setting up these quantum interferences. The Brumer-Shapiro [1,2] method works in the frequency-domain and involves changing the phase-difference between two narrow bandwidth light fields coupling one initial state with the same degenerate set of final states. The Tannor-Kosloff-Rice [3,4] strategy works in the time-domain and involves changing the delays in a sequence of femtosecond light pulses used to transfer population from an initial state to a defined final state. It is now appreciated that these two approaches are equivalent, although the time-domain perspective is conceptually more appealing due to its correspondence with the classical dynamics of the system. In the time domain approach, the inherent large bandwidth of the first light pulse in a femtosecond pulse sequence creates a coherent superposition of eigenstates of the system, generating a wave packet, whose initial motion mimics that of a classical particle moving in its corresponding classical potential. Subsequent femtosecond light pulses can then be timed to coincide with the wave packet visiting a particular point on

its potential, where it can be preferentially transferred to a defined point on another potential.

To determine a sequence of pulses or waveform for a particular control problem obviously requires prior knowledge of the spatial and phase-evolution of the wave packet. The problem can, however, be tackled in reverse, using learning algorithms to optimise the spectral and phase profiles of the femtosecond laser pulse with feedback from the experiment. This idea was proposed in 1992 by Judson and Rabitz [5], and requires no prior knowledge about the Hamiltonian of the system. The first photochemical control experiment employing this technique was reported by Gerber *et al.* in 1998. It involved manipulating the ratio of various photodissociation products of $CpFe(CO)_2Cl$ [6]. Since then, there has been a great deal of activity and success in employing learning algorithms to control various photochemical and photophysical processes, e.g. [7-11]. More recently Gerber, Baumert and coworkers developed a technique involving the time-dependent shaping of femtosecond light polarisation, allowing control beyond standard pulse shaping [12]. Unfortunately, it has proved exceedingly difficult to decode the complex optical waveforms to retrieve the details of the underlying physics. In an experiment to control the photochemistry of the transition metal complex $CpMn(CO)_5$ [13], Daniel *et al.* deciphered their pulse shape using *ab initio* calculations. Although the pulse turned out to contain just two dominant peaks in the time domain, a great deal of work was needed in order to understand this relatively simple control mechanism. A general solution to the problem of decoding the waveform has still not been developed and has subsequently become an area of huge interest and importance. Considering the above, it therefore seems prudent to return to simple physical systems in which it is possible to fully identify the spatial and phase-evolution of a wave packet in terms of known electronic and molecular parameters. In this chapter, we return to one-coordinate vibrational wave packets and exploit the phase-evolution of the constituent vibrational quantum states, in order to predict sequences of optical pulses which are capable of selectively enhancing or depopulating specific vibrational states, or sets of vibrational states.

In the strong-field regime, theoretical models combining pulse-shaping and adiabatic rapid passage have demonstrated the possibility of a complete transfer of population from an arbitrary initial state to a desired "target" state or superposition of states [14,15]. In contrast, developing an understanding of the phase-evolution of the individual components of a wave packet excited in the weak field regime provides us with knowledge of the underlying physics of the system, and therefore enables the design of intuitive coherent control strategies. There has been a great deal of interest in this type of intuitive coherent control scheme in the context of Rydberg wave packets. For example, Noel and Stroud [16,17] demonstrated that a sequence of two laser pulses with a well-defined phase-difference modifies the state distribution compared to that of a single wave packet, leaving superpositions of only odd or even Rydberg states, and Bucksbaum *et al.* have employed phase-shaping methods to generate Rydberg wave packets with specific characteristics [18,19]. Fielding *et al.* have exploited the phase evolution of angular momentum character in various Rydberg wave packet systems to control the orbital angular momentum in an atom [20], rotational angular momentum in a molecule [21], and the autoionisation/predissociation ratio [22]. Recent experiments with rotational wave packets have further made use of partial revivals to manipulate the phase and spectral content of ultrashort laser pulses [23,24] as well as to control the wave packet evolution [23,25].

The phase evolution of vibrational wave packets has been exploited since the early days of coherent control. For example, Scherer *et al.* first demonstrated how sequences of phase-locked optical pulses could be employed for phase-sensitive detection of wave packets [26]. Fielding *et al.* have exploited the well-defined phase difference that accumulates between vibrations in different isotopes of the same molecular species after just a few vibrational periods, as well as using pairs of optical pulses to selectively pump one isotope back down to the ground state thereby enhancing the excited state population of the other isotope [27]. Leibscher and Averbukh [28] have also used interference methods to maximise the difference between the ionisation probabilities of two isotopes at a fixed time interval, but rather than using an intuitive

approach they employed a linear optimisation procedure. More recently, Shapiro *et al.* [29] illustrated that it was possible to control the evolution and revival structure of a vibrational wave packet using the perspective of quantum information processing.

Some of the above ideas are extended in this work, with the aim of controlling the population distribution and therefore the dynamics of vibrational wave packets. From our definition of the phase relationship between the individual vibrational states that constitute the wave packet, we demonstrate full control over the time-dependent populations in the superposition using an intuitive sequence of phase-locked pulses. In addition, our results offer some insight into recent experiments by Ohmori *et al.*, who employed the optical Ramsey method to manipulate the populations of vibrational eigenstates in HgAr dimers [30].

4.2 DYNAMICS OF VIBRATIONAL WAVE PACKETS

The dynamics of one-dimensional vibrational wave packets have been investigated since the early days of quantum mechanics [31], long before the era of coherent control. One of the major challenges in the field was the problem of classical-quantum correspondence, which stimulated studies of wave packet motion in anharmonic systems, primarily the Morse potential. Wilson and co-workers [32-34] calculated the exact quantum dynamics of wave packets in a Morse potential and showed that the more anharmonic the potential, the quicker the wave packet dynamics deviated from the classical trajectory. Stechel and Schwartz [35] performed numerical calculations of the long-time evolution of Gaussian wave packets that were initially localized near the right and left turning point of the Morse potential. They showed that after many oscillations, the dynamics of the wave packet differed from the classical picture. They also discovered the phenomenon of wave packet bifurcation i.e. the splitting up of the wave packet into two parts.

The excited vibrational states, v, of diatomic molecules exhibit anharmonicity in the approximate form of the Morse potential with energy $E = \hbar\omega_{cl}(v - \alpha v^2)$, where ω_{cl} is the classical vibrational frequency and α is the anharmonicity parameter. It is now well understood that immediately after its creation, a vibrational wave packet approximates a classical particle by oscillating in the vibrational coordinate with a classical period $T_{cl} = 2\pi/\omega_{cl}$. The anharmonicity of the potential, determined by α, causes the wave packet to disperse after several vibrational periods. However, this process is reversible and after a time $T_{rev} = T_{cl}/\alpha$, all the components in the wave packet are back in phase with one another. Averbukh and Perelman [36] made a detailed investigation of the long-term evolution of wave packets composed of excited states of quantum systems in general. They recognised that at distinct intervals along the classical trajectory for $t < T_{rev}$, series of correlated sets of localised components were formed. These mini-packets or partial revivals, have $1/q$ of the total probability and exhibit local periodicities of T_{cl}/q. They arise when the different components of the wave packet move in and out of phase with one another. In terms of the phase evolution, at times $t = (p/q)T_{rev}$, where p/q is an irreducible fraction of integers, the phase distribution gains some order and the individual components of the wave packet are split into sets of states within which the contributing components are in phase with one another. The first visible reconstruction of the wave packet occurs at $T_{rev}/2$, although at this time the phases of the odd eigenstates are π out of phase with the even eigenstates [36]. The review by Robinett [37] provides an excellent and very detailed account of wave packet revivals and partial revivals in a variety of different physical systems. Vetchinkin *et al.* [38,39] used this general analysis of the phase-evolution of wave packets and specifically determined the spectral composition and intensities of the partial revivals in a Morse-like anharmonic system.

Early experimental work on the control of vibrational wave packet dynamics, through the use of wave packets prepared by shaped femtosecond pulses, demanded a detailed understanding of the various orders of molecular wave packet phenomena, and therefore, recognition of differences between atomic and molecular behaviour.

Molecular systems have to rely on detection points determined by the Franck-Condon factors for the relevant potential curves. Consequently, interesting dynamics can occur when the Condon point is not at a classical turning point of the potential curve. A well-known example is provided by the I_2 system [40,41], where experiments revealed an apparent full revival around the time of the second order partial revival. As a result, the wave packet was detected twice per classical period leading to the observation of harmonics in the wave packet motion. Recently Löhmuller *et al* [42] used the interferences between the constituent eigenstates of a vibrational wave packet to explain the anomalous results. These types of experiment clearly indicate that, in comparison to atomic systems, analysis of wave packet motion in molecular systems requires both knowledge of the relevant potential energy curves and an understanding of the phase evolution of the wave packet constituents.

With the aim of understanding vibrational wave packet motion in terms of oscillations of specific eigenstates, Vrakking *et al.* [43] determined which vibrational states were in phase at each partial revival order, and showed that at the qth order revival, every qth vibrational state in the wave packet is in phase. In their analysis, the detected signal was defined as $S(t)=|P(t)|^2$, where $P(t)=\sum_v g_v \exp(-iE_v t/\hbar)$. As the period of the signal is related to the classical frequency of the molecular vibration, ω_{cl}, the signal can be expressed as

$$S(t)=\sum_{v'v} a_{v'}a_v \cos[(E_v - E_{v'})t/\hbar] \tag{4.1}$$

Here $a_v = g_v\langle f|\vec{\mu}\cdot\vec{E}|v\rangle$, where $\langle f|$ represents the final ionic state, $\vec{\mu}$ is the transition dipole and $\vec{E}$ is the electric field vector of the laser pulse. This expression shows that the observed wave packet signal is composed of beat frequencies between all pairs of energy levels that make up the wave packet. The lowest frequencies correspond to beats between adjacent vibrational levels, $v' = v \pm 1$, with a frequency of approximately ω_{cl}. The higher frequencies correspond to beats between further separated energy levels. In general, frequencies of approximately $l\omega_{cl}$ are due to beats between energy levels v and

$v-l$, where l is an integer. Using (4.1), it is possible to determine which harmonics are expected for each partial revival order, by expressing the phase of the beats between vibrational states $|v\rangle$ and $|v'\rangle$ as

$$\phi_{vv'}(t) = (E_v - E_{v'})t/\hbar = 2\pi(\alpha^{-1} - v - v')(v - v')t/T_{rev} . \tag{4.2}$$

The lth harmonic of ω_{cl} comes from the beating between states $|v\rangle$ and $|v-l\rangle$, which have a phase difference of

$$\phi_{v,v-l}(t) = 2\pi l(\alpha^{-1} - 2v + l)t/T_{rev} . \tag{4.3}$$

To determine which vibrational states are in phase at each partial revival, the times t need to be established where the phase differences are independent of v (in modulo 2π), so that all states separated by l can add constructively. This requires $2vlt/T_{rev}$ to be an integer, which has solutions $t/T_{rev} = k/(2l)$ where k is an integer. Therefore the lowest frequency beats, where $l = 1$, will be in phase at $t = T_{rev}/2$, T_{rev}, ..., while the second harmonic beats ($l = 2$) will be in phase at $t = T_{rev}/4$, $T_{rev}/2$, $3T_{rev}/4$,....etc. Essentially, the above analysis shows that at the second order partial revival, all the odd states are in phase and they are π out of phase with all the even states. In a similar way, at the third order partial revival, every third vibrational state is in phase, and each set of states is separated from the other states by $2\pi/3$. This pattern is established for each partial revival order.

This description of the phase relationship of vibrational states at the partial revivals is significant to our analysis of the phase evolution of vibrational states in 2- and *n*- wave packet excitation. In the same way as this model describes the phase at the various revival orders, this chapter provides a description of the phase relationship of vibrational states during the first vibrational period. A complete description of the phase evolution is also presented and, in addition, we use the predicted phase evolution to design intuitive pulse sequences in order to manipulate the dynamics of the system.

4.3 THEORY

4.3.1 SPECTROSCOPY OF Na_2

The coherent control strategy proposed in this chapter is illustrated by simulating wave packet interference in the ground state of the sodium dimer ion. A unique approach for exciting and observing vibrational wave packet dynamics on the ionic potential surface, described in chapter 3 and ref. [44], combines phase-modulated detection e.g. [45,46] and ZEKE-PFI techniques e.g.[47,48]. In this method, discrete ranges of Rydberg states associated with each individual vibrational state of the ion are selectively pulsed-field ionised. This effectively filters out the dynamics of the nuclei in the vibrational coordinate. In relation to the calculations, the sodium dimer is convenient for a number of reasons. The vibrational spectrum is closely quadratic and the vibrational spacing yields a classical vibration period of approximately 270 fs, which is ideal for excitation with commercial femtosecond laser sources. There are detailed experimental data available in the form of molecular constants, Franck-Condon factors and potential energy curves [49,50]. Ref [51] for example, presents an extensive bibliography summarising a variety of experimental and theoretical work on the electronic and rovibrational levels of Na_2.

Figure 4.1 illustrates the two-photon excitation scheme used in the calculations. The Na_2^+ ion is excited from a stationary vibrational level of the $A^1\Sigma_u^+$ state of Na_2, which is readily accessible from the ground $X^1\Sigma_g^+$ state. Wave packets are created in the $X^2\Sigma_g^+$ state of the ion by excitation with a broad bandwidth femtosecond laser pulse, forming a coherent superposition of several vibrational states. Note that v'', v' and v correspond to vibrational states in the ground $X^1\Sigma_g^+$ state, the intermediate $A^1\Sigma_u^+$ state and the $X^2\Sigma_g^+$ state of the ion respectively.

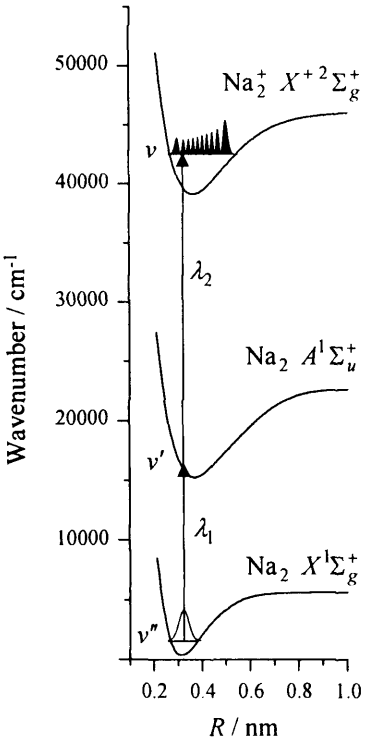

Figure 4.1 Schematic representation of the two-photon excitation scheme employed in the calculations. The first excitation is from the ground $Na_2\ X^1\Sigma_g^+(v''=0)$ state to a well-defined vibrational level of the $Na_2\ A^1\Sigma_u^+$ intermediate state ($\lambda_1 \approx 565$ nm). The second excitation ($\lambda_2 \approx 400$ nm) creates a vibrational wave packet in the $Na_2^+\ X^{+2}\Sigma_g^+$ potential. Vibrational levels in the ground, intermediate and excited states are designated v'', v' and v respectively.

The vibrational and rotational energies for the excitations were calculated using spectroscopic constants determined by Kusch and Hessel (model I) [52] for the $X\ ^1\Sigma_g^+$ state, Jackowska *et al* [53] for the $A\ ^1\Sigma_u^+$ state and Bordas *et al.* [54] for the $Na_2^+\ X^2\Sigma_g^+$ state. The constants were fed into the Dunham expansion [55],

$$T_{i,k} = \sum_{i,k} Y_{i,k}(v+1/2)^i J^k (J+1)^k \qquad (4.4)$$

where the subscript i refers to the power of the vibrational quantum number and j, the rotational quantum number. The coefficients of the expansion are related to the spectroscopic constants in the following way:

$$Y_{10} = \omega_e \qquad Y_{20} = \omega_e x_e \qquad Y_{01} = B_e \qquad Y_{02} = D_e \qquad Y_{11} = \alpha_e \tag{4.5}$$

The Dunham expansion uses the following expressions to represent the energy difference between the *(v', J')* and *(v'', J'')* vibrational-rotational levels of the electronic states involved in the transition:

$$v(v''J'', v'J') = T_e + \left[G(v') - G(v'')\right] + \left[F_{v'}(J') - F_{v''}(J'')\right] \tag{4.6}$$

where

$$G(v) = \omega_e(v+1/2) - \omega_e x_e(v+1/2)^2 + \omega_e y_e(v+1/2)^3 + \omega_e z_e(v+1/2)^3 + \ldots \tag{4.7}$$

and

$$F_v(J) = B_v\left[J(J+1) - \Lambda^2\right] - D_v\left[J(J+1) - \Lambda^2\right]^2 + \ldots \tag{4.8}$$

The first term, T_e, in (4.6) is the electronic energy separation between the ground and excited states (the energy separation between the minima of the two potential energy curves). The second term expresses the vibrational energy difference, and the last term represents the energy difference between the rotational levels in the upper and lower vibrational states. In (4.7) the vibrational energy, $G(v)$, is given by a series expansion in powers of $(v+1/2)$ where v is the vibrational quantum number. In (4.8) the rotational energy in the vibrational level v, $F_v(J)$, is given by a series expansion in powers of $[J(J+1)-\Lambda^2]$, where J is the rotational quantum number and Λ is the absolute value of the projection of the electronic angular momentum on the internuclear axis. For

Σ states $\Lambda = 0$, therefore this term has been neglected in the calculations. The rotational constants B_v and D_v depend on the vibrational level v and are represented by another power series in $(v+1/2)$:

$$B_v = B_e - \alpha_e(v+1/2) + \gamma_e(v+1/2)^2 + \ldots \tag{4.9}$$

and

$$D_v = D_e + \beta_e(v+1/2) + \delta_e(v+1/2)^2 + \ldots \tag{4.10}$$

A selection of the calculated energies were compared to the experimentally determined values of Verma *et al* [51] and were found to be accurate to 0.2 cm^{-1} for $0 < v < 30$. Both the vibrational and rotational energies are calculated for completeness. Nevertheless, we neglect the effects of molecular rotation in the wave packet calculations. Such an approximation is justified by the fact that the rotational period is very long compared to the vibrational period.

4.3.2 VIBRATIONAL WAVEFUNCTIONS AND FRANCK-CONDON FACTORS

The composition of vibrational states in a wave packet is not only determined by the energy and bandwidth of the exciting laser pulse – the transition probabilities also are an integral part of the excitation. To determine which transitions between vibrational states are more probable, the vibrational wavefunctions and the corresponding Franck-Condon factors were calculated. The wave functions were calculated from the pseudopotentials of Bardsley *et al.* [56], using LeRoy's program Level 7.1 [57] which numerically integrates the Schrödinger equation using the Numerov-Cooley method [58]. The output wave functions from Level 7.1 were fed into a Fortran77 program (see appendix 1) to calculate the relevant Franck-Condon factors. In addition to the

calculated results, the following section provides a brief description of vibrational wave functions and the origin of the Franck-Condon principle.

For a diatomic molecule A—B with n electrons, the Schrödinger equation is written:

$$\left(-\frac{\hbar}{2\mu}\nabla^2 - \frac{\hbar^2}{2m}\sum_{i=1}^{n}\nabla^2 + V\right)\Psi = E\Psi \tag{4.11}$$

where Ψ is the total electronic and nuclear wavefunction and E is the total energy. It is assumed that 4.11 can be solved if the electronic and nuclear motion are separated. This assumption is called the Born-Oppenheimer approximation and takes into account the vastly different masses of the electrons and the nuclei. By applying the Born-Oppenheimer approximation, a separate Schrödinger equation can be written for just the nuclear motion which depends only on the internuclear distance R. This is the radial Schrödinger equation for nuclear motion:

$$-\frac{\hbar^2}{2\mu R^2}\frac{d^2}{dR^2}\left(R^2\frac{d\psi}{dR}\right) + \frac{J(J+1)\hbar^2}{2\mu R^2}\psi(R) + E(R)\psi(R) = E_{v,J}\psi(R) \tag{4.12}$$

The solutions $\psi(R)$ give the vibrational wavefunctions.

In the rigid rotor model for vibrational motion of a diatomic molecule, the internuclear distance is assumed to be fixed at R_e so that the radial Schrödinger equation for the nuclear motion can be ignored. To look at the radial (vibrational) motion by itself, an assumption is made that the rotational energy term can be approximated by its rigid rotor value.

$$\frac{J(J+1)\hbar^2}{2\mu R^2} \approx \frac{J(J+1)\hbar^2}{2\mu R_e^2} = E_{rot} \tag{4.13}$$

(4.12) now becomes

$$-\frac{\hbar^2}{2\mu R^2}\frac{d^2}{dR^2}\left(R^2\frac{d\psi_{v,J}}{dR}\right) + E_{rot}\psi(R) + E(R)\psi_{v,J}(R) = E_{v,J}\psi_{v,J}(R) \tag{4.14}$$

By taking the zero of the energy to be minimum in the potential energy function *E(R)*, the nuclear motion can be written as $E_{v,J} \equiv E_{nuc} = E_{vib} + E_{rot}$ and cancelling the term $E_{rot}\psi(R)$ on both sides of 4.14 and some simplification gives

$$-\frac{\hbar^2}{2\mu}\frac{d^2}{dR^2}\left(R^2\frac{d\psi}{dR}\right)+E(R)\psi(R)=E_{vib}\psi(R) \tag{4.15}$$

This is equivalent to the Schrödinger equation for the harmonic oscillator and is a satisfactory first approximation. The kinetic energy term in (4.15) can be simplified by writing $\psi(R)=(1/R)\chi(R)$ and substituting into (4.15) to obtain

$$-\frac{\hbar^2}{2\mu}\frac{d^2}{dR^2}\chi(R)+E(R)\chi(R)=E_{vib}\chi(R) \tag{4.16}$$

The solutions to 4.16 are single-valued and finite, but are also continuous and vanish at infinity. Most importantly, solutions only exist for values where

$$E_{vib}=E(v)=h\nu_{cl}\left(v+\tfrac{1}{2}\right) \qquad v=0,\,1,\,2,... \tag{4.17}$$

where ν_{cl} is the classical vibrational frequency given by

$$\nu_{cl}=\frac{h}{2\pi}\sqrt{\frac{k}{\mu}} \tag{4.18}$$

The eigenfunctions of the Schrödinger equation (4.16) of the harmonic oscillator are known as Hermite orthogonal functions [59], and are polynomials of the form:

$$\psi_v = N_v e^{-\frac{1}{2}ax^2} H_v\left(\sqrt{a}x\right). \tag{4.19}$$

Here, N_v is a normalisation constant, $\alpha = 4\pi^2 \mu \nu_{cl} / h$ and $H_v(\sqrt{a}x)$ is a Hermite polynomial of the vth degree. A selection of relevant vibrational eigenfunctions ψ_v of the X^+ state of Na_2 is plotted in figure 4.2.

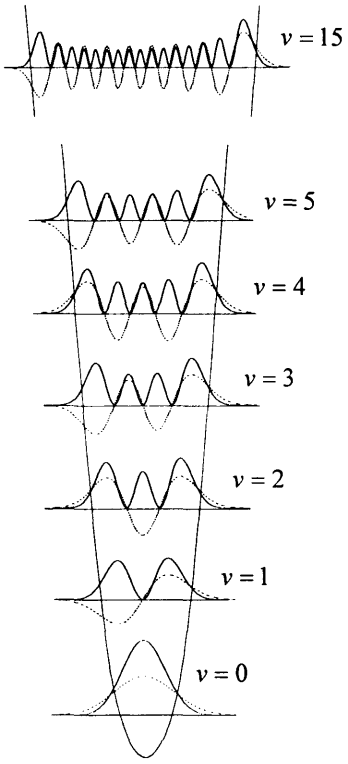

Figure 4.2 The vibrational wavefunctions (dashed lines) and probability density distributions (solid lines) of Na_2^+ for $v = 0-5$ and $v = 10$, calculated using LeRoy's program Level 7.1 [57]. The wave functions are plotted schematically against the Na potential curve obtained from Bardsley *et al.* [56].

The next step in the calculations is to determine the transition probabilities for the $A^1\Sigma_u^+(v') \leftarrow X^1\Sigma_g^+(v'')$ and $X^{+2}\Sigma_g^+(v) \leftarrow A^1\Sigma_u^+(v')$ transitions in Na_2. The first assumption we make is that the Na_2 molecules are vibrationally cold, i.e. at equilibrium there will be greatest probability of the molecules occupying the $v'' = 0$ state of the ground $X^1\Sigma_g^+$ state of Na_2. The number of molecules in a state v is given by $N_v = (N/Q_v)e^{-E_v hc/kt}$ where $Q_v = 1 + e^{-E_v hc/kt}$ is the vibrational partition function. For example in a jet-cooled beam, a vibrational temperature of 50K can be achieved resulting in 98.97% of sodium dimers being in the $v'' = 0$ state.

The transition probability for a vibrational transition between potential curves is determined by the Franck-Condon principle, which can be stated as follows. Due to the vastly differing masses of the electrons and nuclei, the electronic motion is much more rapid than the nuclear motion and therefore, electronic transitions take place on a time scale that is too short for any appreciable nuclear motion [60]. Essentially, electronic transitions are "vertical" in the sense that the internuclear distance in the final state is the same as it was in the initial state. The result is a whole series of vibrational transitions of differing intensities to neighbouring levels as opposed to a single sharp transition with a well-defined vibrational excitation energy. The quantum-mechanical formulation states that the transition probability is determined by the Franck-Condon integral:

$$a_{v'v} = \int \psi_{v'}(R)\psi_{v}(R)dR \tag{4.20}$$

which describes the overlap of vibrational functions in the ground and excited electronic states; its square $a^2_{v',v}$ is referred to as the Franck-Condon factor. The Franck-Condon factors for the $A^1\Sigma_u^+(v'=0-21) \leftarrow X^1\Sigma_g^+(v''=0)$ transitions in Na_2 are shown in figure 4.3.

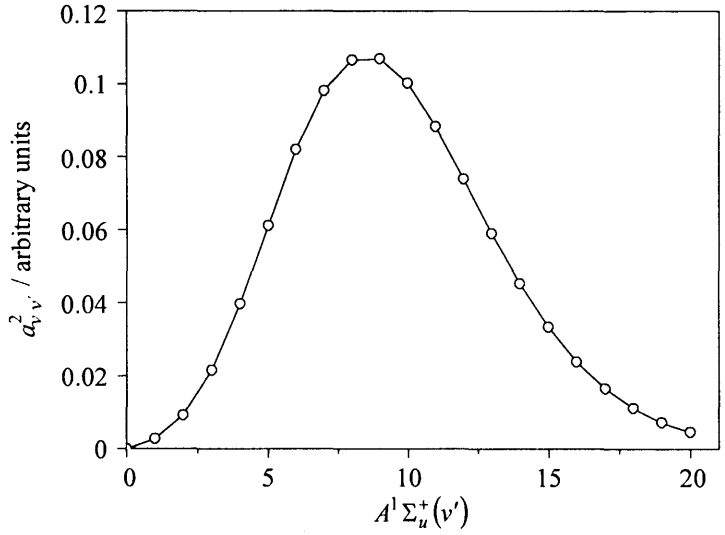

Figure 4.3 Franck Condon factors for the $A^1\Sigma_u^+(v'=0-20) \leftarrow X^1\Sigma_u^+(v''=0)$ transitions.

It is clear that the maximum transition probability is attributed to the $v' = 8,9 \leftarrow v'' = 0$ transitions, although there is also appreciable intensity in all transitions ranging from $v' = 5 \leftarrow v'' = 0$ to $v' = 15 \leftarrow v'' = 0$. This presents us with a choice of "launch state" for vibrational wave packet creation. Essentially, we can make an excitation to the Na_2^+ state from $v' = 5 - 15$ vibrational levels of the intermediate A state.

The Franck-Condon factors for the $Na_2^+ X^{+\,2}\Sigma_g^+(v = 0 - 20) \leftarrow Na_2\, A^1\Sigma_u^+(v' = 0 - 20)$ transitions are presented in figure 4.4. These values are of physical significance as they determine the relative populations of vibrational eigenstates in the resulting wave packet.

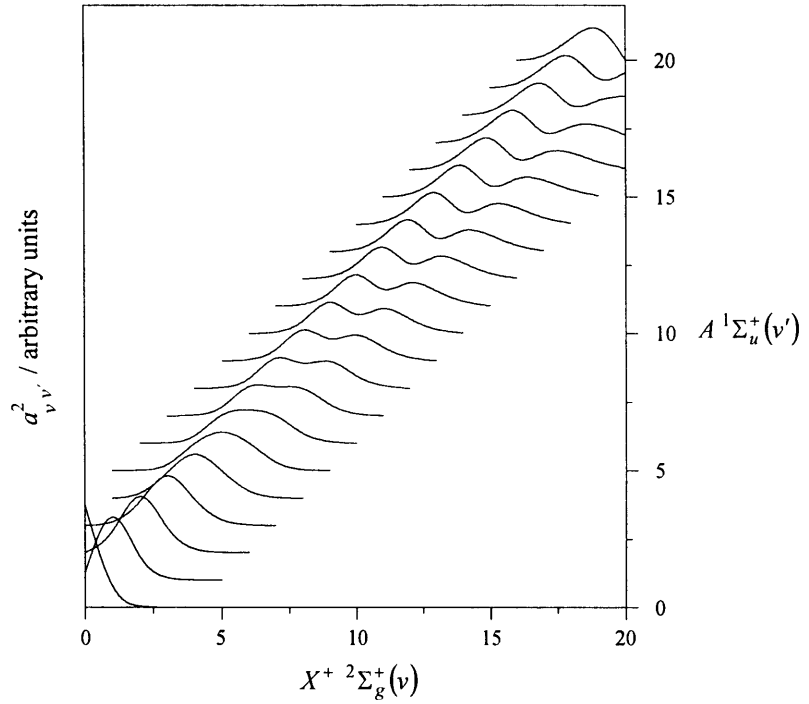

Figure 4.4 Calculated Franck-Condon factors for a series of transitions ranging from a single vibrational level in the $A^1\Sigma_u^+$ state of Na_2, to $v = 0 - 20$ of the $X^{+\,1}\Sigma_u^+$ state of Na_2^+. The factors were obtained from the overlap integrals of the vibrational wavefunctions described previously. The y – axis on the right represents the initial vibrational level of the A state, whilst the x – axis represents the range of excited state vibrational levels for each transition. The left-hand y – axis shows the relative intensity of each transition.

The steep front ridges of the Franck-Condon factors in figure 4.4 arise from the constructive overlap of the maxima of the probability distribution of one vibrational wavefunction with the maxima of the probability distribution of the other. This corresponds to the molecule making a vertical transition in the potential energy diagram. From figure 4.4 it can be seen that double peak structure emerges as transitions to higher vibrational levels are made. These result from the constructive and destructive interference between the intermediate maxima and minima of the vibrational wavefunctions in the overlap integral. Figure 4.5 represents the vibrational wavefunctions and Franck-Condon overlaps for (a) the $v=1 \leftarrow v'=1$ and (b) the $v=9 \leftarrow v'=9$ transitions.

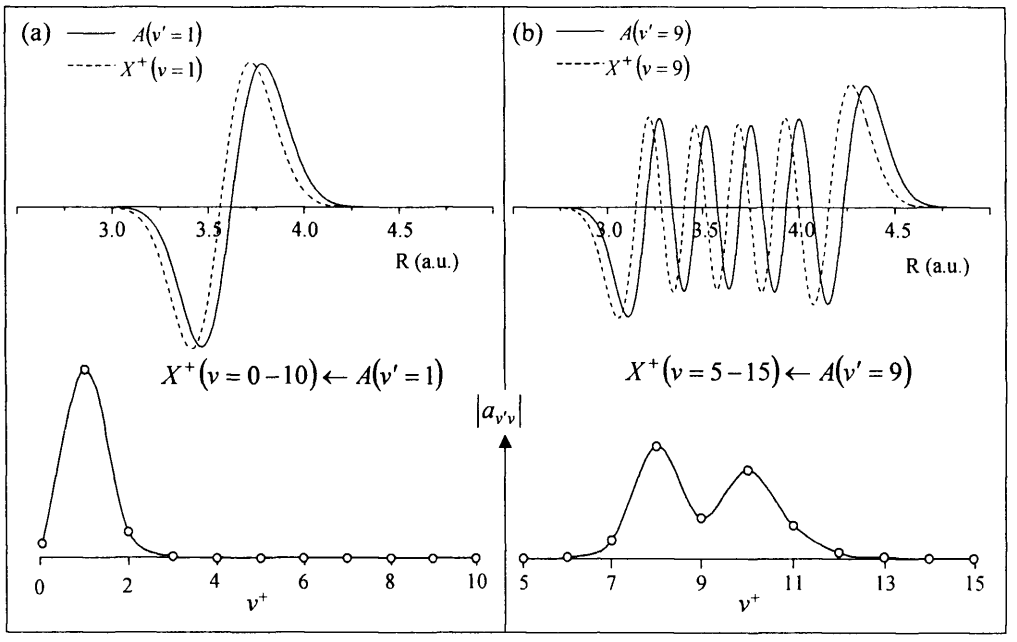

Figure 4.5 In (a) the top graph shows the vibrational wavefunctions for the $v'=1$ and the $v=1$ levels of the A state and ion state. The graph below shows the Franck-Condon overlap for the $X^+(v=0-10) \leftarrow A(v'=1)$. The (1,1) transition has the maximum intensity. In (b) the top graph shows the vibrational wavefunctions for the $v'=9$ (dashed lines) and the $v=9$ (solid lines) levels of the A state and ion state respectively. The graph below shows the Franck-Condon overlap for the $X^+(v=5-15) \leftarrow A(v'=9)$. The (8, 9) and (10, 9) transitions have the maximum intensity.

It can be seen in figure 4.5(a) that there is almost complete constructive interference between the maxima and minima of the vibrational wavefunctions giving rise to an almost perfect Condon Parabola with the most intense peak at the (1,1) vertical transition. However, as we go to transitions with higher vibrational quantum number, we can see that a subsidiary parabola has started to emerge as a result of destructive interference between the maxima and minima of the wavefunctions and the double peak structure emerges. Therefore in figure 4.5(b), the maximum overlap is not the expected vertical (9,9) transition but the (8,9) and (10,9) transitions.

4.3.3 THE CONTROL SCHEME

This section describes our method of optical control, and outlines the theoretical tools we employ in the calculations. The first step is excitation of a number of vibrational states in the Na_2^+ potential by a femtosecond laser pulse, creating a vibrational wave packet, $\Psi(t) = \sum_v a_v g_v |v\rangle \exp(-iE_v t/\hbar)$. Here, $|v\rangle$ is the set of vibrational eigenstates with energies $E_v = \hbar\omega_v$, and $g_v = \exp\left[-2\ln 2(E_v - E_L)^2/\Delta E^2\right]$ is the Gaussian spectral profile of the laser pulse with a full-width at half-maximum ΔE and central excitation energy E_L. We monitor the evolution and probability density of this superposition state using the autocorrelation,

$$\langle \Psi(0)|\Psi(t)\rangle = \sum_v a_v^2 g_v^2 \exp(-i\omega_v t). \tag{4.21}$$

The observable signal in the calculations is the modulus of the autocorrelation $S(t) = \left|\langle \Psi(0)|\Psi(t)\rangle\right|$, which describes the probability of finding the wave packet back in its initial state. In order to simulate a coherent control strategy in which we launch a sequence of k identical laser pulses at times t_k after the initial laser pulse, we need to determine the modulus of the modified autocorrelation,

$$\langle \Psi(0)|\Psi(t)\rangle = \sum_v a_v^2 g_v^2 \exp(-i\omega_v t)\left[1+\sum_k \exp(-i\omega_v t_k)\right]. \tag{4.22}$$

The vibrational state population distribution following the sequence of k identical laser pulses at times t_k can be deduced by calculating the populations b_v^2, after the last excitation pulse [61,62], using

$$b_v = -\frac{i}{2}\Omega_v g_v\left[1+\sum_k \exp(-i\Delta_v t_k)\exp(i\omega_L t_k)\right], \tag{4.23}$$

assuming that the optical fields are weak and the A-state amplitude remains virtually unchanged by the optical pulses. Here, b_v is the probability amplitude and Ω_v is the Rabi frequency for the excitation between the A-state and ionic-state. The detuning Δ_v, is defined as $\Delta_v = \omega_L + \omega_{v'} - \omega_v$, where ω_L is the central excitation frequency of the laser pulse, and $\omega_{v'}$ and ω_v represent the vibrational frequencies of the A-state and the ionic state respectively.

4.4 RESULTS AND DISCUSSION

First, calculations were performed to determine the dynamics of a single wave packet excited from the v' = 5 level of the A-state using a 40 fs laser pulse centred around v = 5 state of the ion. The modulus of the autocorrelation function is calculated using (4.21) and plotted in figure 4.6.

At short times, the spectrum is that of a well-localised wave packet oscillating at the classical vibration frequency (approximately 266 fs). The next step is to investigate the effect of firing a sequence of identical laser pulses. In the simple case of double wave packet excitation, a second wave packet is launched at a time t_k that corresponds to

$$t_k = (p/q)T_{cl} + t_\phi \tag{4.24}$$

where $t_\phi = \phi/\omega$ is the delay that corresponds to an optical phase shift ϕ, with reference to optical frequency ω.

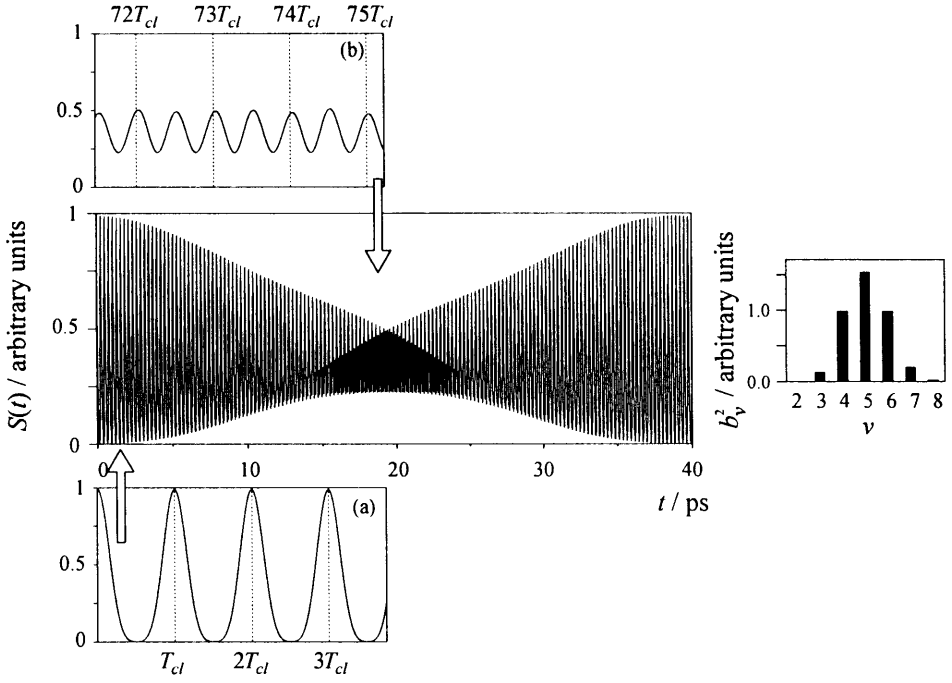

Figure 4.6 Central figure: Calculated wave packet recurrence spectrum and corresponding population distributions of a single wave packet centred around $v = 5$. The excitation was made with a 40 fs bandwidth limited Gaussian pulse. Figure (a) shows the wave packet at t = 0, oscillating at the classical vibrational frequency. Figure (b) shows the dynamics at t = 19.5 ps, the region of the second order partial revival. Here the wave packet has split into two and peaks are observed at twice the classical vibrational frequency. The vibrational state population distribution, showing a Gaussian distribution, is presented on the right hand side of the figure.

The resultant vibrational state population distributions are plotted in figure 4.7. The populations of each of the three central vibrational states v = 4, 5 and 6, are calculated using (4.23), for coarse delays $(p/q)T_{cl}$ corresponding to (a) 0, (b) $T_{cl}/3$, (c) $T_{cl}/2$, (d) $2T_{cl}/3$, (e) T_{cl}, and with ϕ ranging from $-\pi$ to π. We are justified in monitoring the populations of just the three central vibrational states v = 4 – 6, as they constitute 98% of the population of wave packet. Irrespective of the coarse delay between the pair of optical pulses, the populations of the constituent vibrational states oscillate at the optical

frequency for excitation between the A-state and ionic-state. Figure 4.7(a) shows that when the two pulses are launched together at $t = 0$, but with a phase-shift, the populations of the constituent states oscillate in phase with one another. When $\phi = 0$ the populations are maximum, and when $\phi = \pm\pi$ the ionic state vibrational population is depleted. If the first wave packet is allowed to evolve for $T_{cl}/3$ before the second wave packet is launched, the populations of the constituent eigenstates still oscillate at the Rabi frequency as the phase-difference is scanned, but this time the populations of the individual vibrational states oscillate out of phase with one another. From figure 4.7(b) it can be seen that the population of the central $v = 5$ state is a maximum when $\phi = -0.13\pi$, and that the populations of the $v = 4$ and 6 states are maximum for $\phi = 0.53$ and $\phi = -0.80\pi$, i.e. their maxima are shifted $\phi = \pm 2\pi/3$ from that of the $v = 5$ state. Figure 4.7(c) illustrates the population distribution for a delay $T_{cl}/2$. In this case, the population of the odd $v = 5$ state oscillates out of phase with populations of the even $v = 4$ and 6 states. The population of the central $v = 5$ state passes through a maximum when $\phi = -0.20\pi$ which coincides with the minimum population for the even $v = 4$ and 6 states.

Figure 4.7(d) illustrates the population distribution for a delay $2T_{cl}/3$. Now, the population of the central $v = 5$ state is a maximum when $\phi = -0.27\pi$, and the populations of the $v = 4$ and 6 states are maximum for $\phi = -0.93\pi$ and 0.40π. This situation is similar to when the delay is $T_{cl}/3$, in that now the $v = 4$ and 6 population maxima are shifted $\phi = \mp 2\pi/3$ from that of the $v = 5$ maximum. Note that in figure 4.7(d), the phases of the $v = 4$ and 6 states are flipped by π relative to the corresponding phases at in figure 4.7(b). Finally, figure 4.7(e) shows the population distributions following excitation with a pair of optical pulses separated by T_{cl}. Naturally, the populations of all the constituent vibrational states oscillate at the Rabi frequency and in phase with one another, although the populations are now a maximum at $\phi = -0.39\pi$. From figure 4.7 one can establish immediately that the central state of the vibrational wave packet accumulates a phase $\phi = -0.39\pi(p/q)$, where (p/q) is the fraction of T_{cl} for which the first wave packet evolves before the second wave packet is

launched. It is also apparent that these plots can be used to design coherent control strategies. For example, it is clear from figure 4.7(c), that if we allow the first wave packet to evolve for $T_{cl}/2$ (to the outer turning point) and then launch a second wave packet with an optical phase shift $\phi = -0.20\pi$, the odd v = 5 state will interfere constructively enhancing their amplitude whereas the even v = 4 and 6 states will interfere destructively. On the other hand, if we flip the phase by π, the odd vibrational states will be removed from the superposition through destructive interference but the population of even vibrational states will be enhanced through constructive interference. So we already have a rational way of controlling whether the wave packet is composed of even or odd vibrational states.

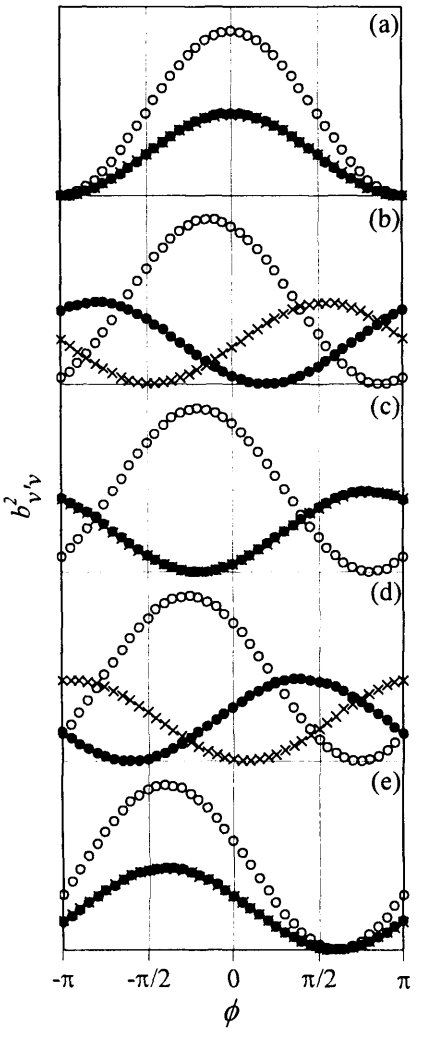

Figure 4.7

Vibrational state population distributions calculated using (3), following excitation with a pair of 40 fs bandwidth limited optical pulses centred around v = 5. The populations of the central v = 5 state are represented by hollow circles, and the adjacent v = 4 and 6 states, by crosses and black circles respectively.

The first wave packet is allowed to evolve to a specific point along the vibrational coordinate before the second wave packet is launched (at time t_2). As the phase, ϕ, of the second wave packet is varied, interference effects between individual vibrational eigenstates are observed in the populations. Plots (a) – (e) are calculated for values of t_2 (a) 0, (b) $T_{cl}/3$, (c) $T_{cl}/2$, (d) $2T_{cl}/3$ and (e) T_{cl} with ϕ ranging from $-\pi$ to π.

In more general terms, we employ a sequence of *k* phase-locked optical pulses to excite *k* wave packets at various times $(p/q)T_{cl}$, where (p/q) is an irreducible fraction of integers. Each pulse in the sequence is shifted by adding a short time delay t_ϕ, specific to each value of *p* and *q*. Essentially, t_ϕ is the time delay needed to induce interference between the molecular phase of a specific vibrational state (or set of states) and the optical phase of the exciting laser pulse, resulting in points of minimum and maximum population. To completely depopulate a specific state *v* we need to set $b_v = 0$ in (4.23), which requires $\mathrm{Re}\left(e^{-i\Delta_v t_k} e^{i\omega_L t_k}\right) = -1$ and $\mathrm{Im}\left(e^{-i\Delta_v t_k} e^{i\omega_L t_k}\right) = 0$. This requirement is satisfied when

$$(\omega_L - \Delta_v)t_k = (2n+1)\pi, \qquad n = 0, \pm 1, \pm 2, \ldots \tag{4.25}$$

Using (4.24) and (4.25), defining $\phi = (\omega_v - \omega_{v'})t_\phi$, and recalling that $\Delta_v = \omega_L + \omega_{v'} - \omega_v$, we can determine the optical phase needed to depopulate a specific state *v*, in the wave packet:

$$\phi_v^- = (2n+1)\pi - (\omega_v - \omega_{v'})(p/q)T_{cl} \qquad n = 0, \pm 1, \pm 2, \ldots \tag{4.26}$$

The superscript '-' implies depopulation. Obviously, flipping the phase by π has the opposite effect and maximises the population of state *v*:

$$\phi_v^+ = 2n\pi - (\omega_v - \omega_{v'})(p/q)T_{cl} \qquad n = 0, \pm 1, \pm 2, \ldots \tag{4.27}$$

We will now use (4.26) and (4.27) to rationalise the control sequences necessary for specific tasks. First, we return to the two pulse scenario described above. Using a sequence of two pulses, separated by half a vibrational period, we wish to determine the phase shift required to completely depopulate a specific vibrational state in the distribution. If we look at the central state in the wavepacket, setting $v = \bar{v}$ and $p/q = 1/2$, (4.26) becomes $\phi_{\bar{v}}^- = (2n+1)\pi - \omega_L T_{cl}/2$. For a wave packet centred around

$\bar{v}$ = 5, excited from the $v' = 5$ level of the $A^1\Sigma_u^+$ state, $\omega_L/2\pi c = 24\,868.01\ \text{cm}^{-1}$ and $T_{cl} = 265.9$ fs. We can therefore determine that the phase shift needed to depopulate the v = 5 state of the wave packet is $\phi^- = 0.804\pi$ for $-\pi < \phi \leq \pi$. Thus, if the second wave packet is launched at $T_{cl}/2$ and phase shifted by ϕ corresponding to $t_\phi = 0.804\pi/\omega_L$, it will interfere destructively with the v = 5 state. In fact, not only does it depopulate the v = 5 state, but it depopulates all the odd states in the wave packet as they are all in phase with one another at $T_{cl}/2$. This can be explained as follows: From (4.26) and (4.27) we deduce that the central state in the wave packet $\bar{v}$, accumulates phase at a rate $d\phi_{\bar{v}}/dt = -\omega_L$. For $\bar{v}$ = 5, $\phi_{\bar{v}} = -0.393\pi(p/q)T_{cl}$ ($-\pi < \phi \leq \pi$) as observed in the population distributions plotted in figure 4.7. We can determine the short-term accumulated phase of all the other states in the wave packet $v = \bar{v} + m$ ($m = \pm1, \pm2, \ldots$) by neglecting anharmonicity and assuming $\omega_{v+m} = \omega_{\bar{v}} + m\omega_{cl}$:

$$\phi_{\bar{v}+m} = \phi_{\bar{v}} - 2\pi m(p/q) \tag{4.28}$$

We can see that after one vibrational period all the states are in phase in modulo 2π, in agreement with figure 4.7(e). This expression also clarifies the population distributions in figure 4.7(b), (c) and (d). Applying (4.28) to figure 4.7(c), every other state in the distribution is in phase in modulo 2π at $T_{cl}/2$, i.e. all the even states are in phase with one another but are π out of phase with the odd states. Applying (4.28) to the situations in figures 4.7(b) and (d), every third state in the distribution is in phase in modulo 2π at $T_{cl}/3$ and $2T_{cl}/3$, and every third state is shifted from the two adjacent states by $2\pi/3$. Figure 4.8 shows the accumulated phase of the $v = 4$, 5 and 6 states in a wave packet centred around $v = 5$ after one vibrational period

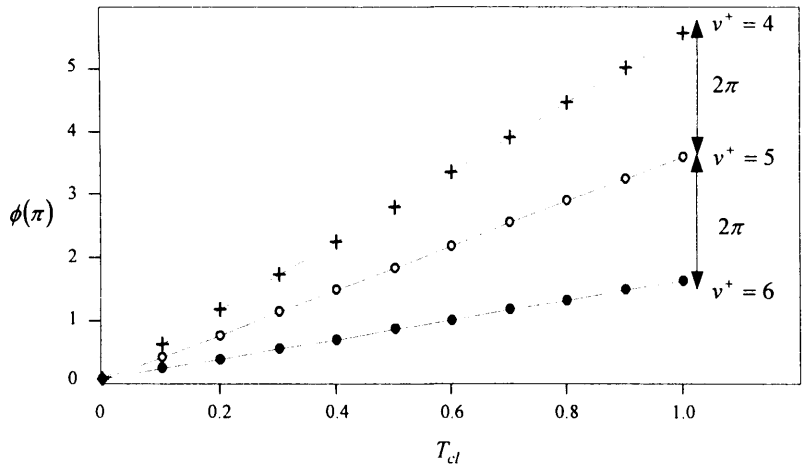

Figure 4.8 Plot showing the rate of phase accumulation of the $v = 4$, 5 and 6 states (crosses, white circles and black circles respectively) after one vibrational period.

The plot clearly shows that after T_{cl}, all the states are in phase in modulo 2π, but in reality each vibrational state v has accumulated 2π more phase than the $(v+1)$th state. Of course, the phasing of vibrational states depends explicitly on the anharmonicity of the system. The Na_2^+ ion is virtually harmonic at these low v and therefore is an ideal candidate for this type of coherent control scheme.

A portion of a wave packet recurrence spectrum following excitation by a sequence of two pulses separated by $T_{cl}/2$ is illustrated in figure 4.9, along with the corresponding vibrational state population distribution. The corresponding spectrum following excitation by a single pulse was presented in figure 4.6 for comparison. Launching the second pulse at $T_{cl}/2$ ensures that the even and odd vibrational states are out of phase with one another, giving us the freedom to launch the second wave packet to interfere constructively with one set and destructively with the other set.

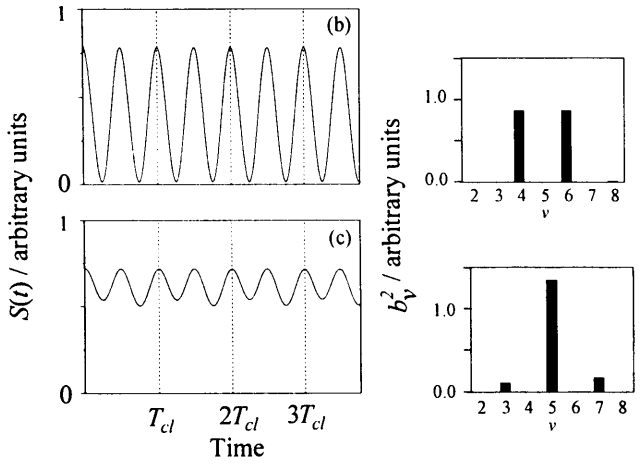

Figure 4.9 Calculated wave packet recurrence spectra and corresponding population distributions following excitation with a 40 fs bandwidth limited Gaussian pulse, of a single wave packet (a) and two wave packets separated by $T_{cl}/2$ (b) and (c). In (b), the second pulse is phase shifted to depopulate all the odd states and leave just even states and in (c) the phase is flipped by π to depopulate the even states and leave just the odd states.

As previously mentioned, we know that the odd states are depopulated when $\phi^- = 0.804\pi$. In other words, setting $t_\phi = 0.804\pi/\omega_L$ leaves a wave packet composed of even vibrational states only. Alternatively, flipping the phase by π, i.e. setting $t_\phi = -0.196\pi/\omega_L$ results in a wave packet composed entirely of odd vibrational states. Both of these cases result in a wave packet that oscillates at twice the classical frequency of a wave packet composed of all vibrational states. The "even" wave packet is composed predominantly of two vibrational states v = 4 and 6 and the spectrum is resembles a beat spectrum with no evidence of dispersion. The "odd" wave packet is composed predominantly of a single stationary state v = 5, with very little contribution from v = 3 and 7. This wave packet is not very well localised and therefore the modulations in the time-resolved spectrum are very weak.

Now that we have an understanding of the phase evolution of the individual vibrational components of the wave packet, we can extend the control scheme to a more complex situation. In figure 4.3, the Frank-Condon factors presented for the $Na_2^+(v=5-15) \leftarrow Na_2(v'=9)$ transitions show a minimum in the transition probability for excitation to the central v = 9 state. The distribution clearly shows that

five states have appreciable intensity. Therefore, a sequence of five pulses separated by intervals of $T_{cl}/5$, with well-defined phases determined by (4.26) and (4.27), can provide total control over the shape of the Franck-Condon profile, and hence the overall wavefunction and the resulting wave packet dynamics. The proposed control scheme is illustrated in figure 4.10. Once the original wave packet is excited, the second wave packet is launched after a delay of $T_{cl}/5$. This wave packet is not phase shifted as the intensity of the $v = 7$ state does not need to be modified. On the other hand, we wish to reduce the relative contribution to the wave packet from the $v = 8$ state, so the third wave packet, excited at $2T_{cl}/5$ is phase shifted to depopulate this state by approximately 50%. The contribution from the central, $v = 9$ state is increased by exciting the fourth wave packet at $3T_{cl}/5$ with a phase shift, which enhances its contribution. The final pulse in the sequence is excited at delay $4T_{cl}/5$. The phase is tuned to decrease the population of the $v = 10$ state by 33% to match the population of the $v = 7$ state.

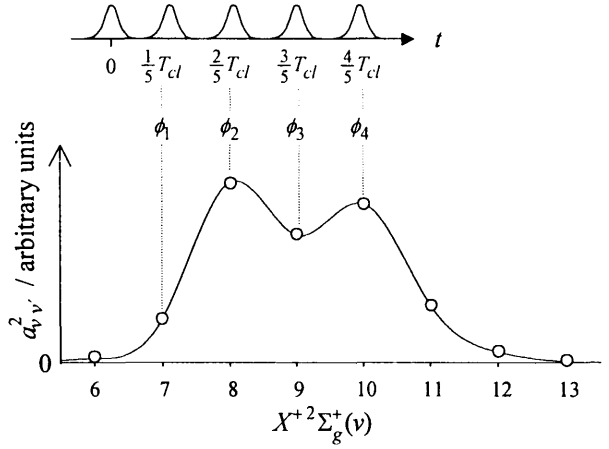

Figure 4.10 Cartoon of a control scheme illustrating how the relative populations of individual states in a wave packet, excited around $v = 9$, can be manipulated. Pulse 1 generates the wave packet and pulses 2 - 5 are assigned to control the vibrational populations of states $v = 7 - 11$ respectively. Pulse 2 is excited after $T_{cl}/5$. Pulse 3 is excited at $2T_{cl}/5$ and phase shifted by $\phi = 0.68\pi$ to reduce the population of $v = 8$ by approximately 50%. The population of the central $v = 9$ state is enhanced by exciting pulse 4 at $3T_{cl}/5$ with a phase shift $\phi = -0.77\pi$. The final pulse 5 is excited at $4T_{cl}/5$ and phase-shifted by $\phi = 0.94\pi$ to interfere destructively and reduce the population of the $v = 10$ state by approximately 33%.

In figure 4.11, the wave packet spectra and corresponding population distributions are presented for wave packets created with (a) the original composition and (b) the engineered composition. The radial distribution functions at $t = 0$ are also presented, as well as the corresponding population distributions are also presented. The natural wave packet spectrum presented in figure 4.10(a) exhibits peaks at twice the classical frequency. The unusual dynamics are a result of the dominant beat between the v = 8 and 10 states. This can also be interpreted as a wave packet that is localised at both extremes of the vibrational coordinate (see inset).

The results of the 5-pulse excitation scheme are presented in figure 4.10(b).

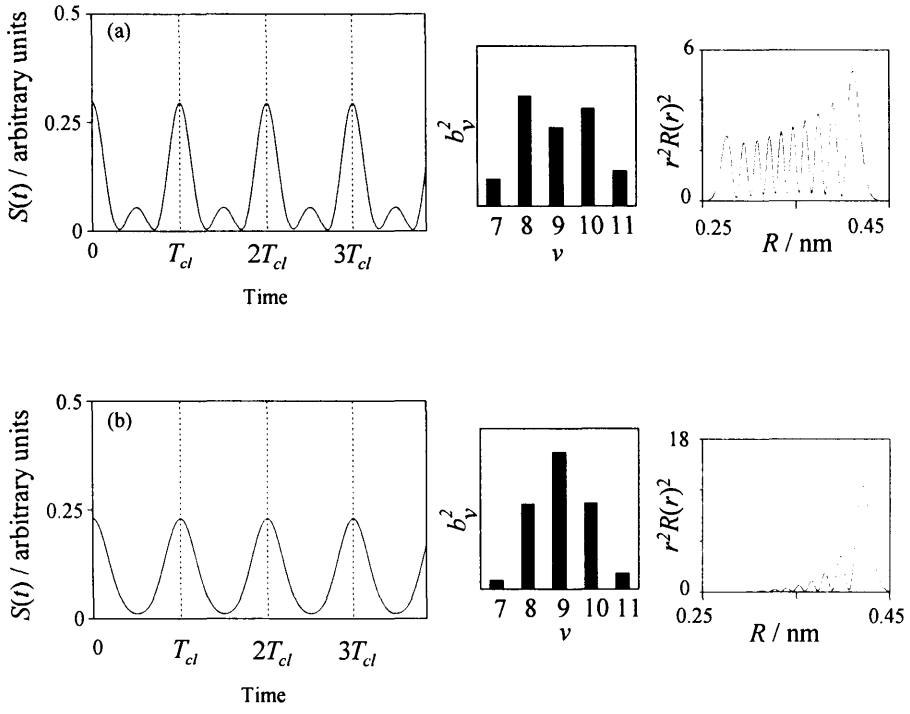

Figure 4.11 Calculated wave packet recurrence spectra following excitation of a single wave packet centered around v = 9 (a) (top) and a sequence of 5 phase-locked wave packets (b) (bottom). Both wave packet spectra are plotted on the same vertical scale with arbitrary intensity units. Vibrational state population distributions are also presented, along with the corresponding radial distribution functions of the resultant vibrational wave packets, immediately after their creation.

The engineered population distribution has a more regular profile and results in a wave packet that oscillates at the classical vibrational frequency. The inset shows that we have effectively destroyed the wave function at the inner turning point of the vibrational coordinate and left only the contribution from the outer turning point.

4.5 CONCLUSION

We have described a logical coherent control scheme, which employs a train of phase-locked optical pulses to generate customised vibrational wave packets. Through our definition of the exact relationship between the phases of the vibrational eigenstates and the optical phase of the laser pulse, we have complete control over the time-dependent populations of the individual components of the wave packet. Our model enables us to select the relative contribution of any state or set of states in the wave packet, following excitation with a sequence of optical pulses with phase-differences that can be precisely determined using our knowledge of the spectroscopic parameters. Although it is possible to develop analytic solutions in the strong field regime, effecting total control over population transfer, our weak field scheme provides an entirely intuitive solution.

These ideas demonstrate that coherent control studies in simple molecular systems help improve our understanding of the link between optical phase and quantum mechanical phase, which is a step further towards the logical engineering of wave packets in complex systems.

4.6 REFERENCES

1. P. Brumer and M. Shapiro, *Chem. Phys. Lett.* **126** (6), 541 (1986).
2. M. Shapiro, J. W. Hepburn, and P. Brumer, *Chem. Phys. Lett.* **149** (5-6), 451 (1988).
3. D. J. Tannor and S. A. Rice, *J. Chem. Phys.* **83** (10), 5013 (1985).
4. D. J. Tannor, R. Kosloff, and S. A. Rice, *J. Chem. Phys.* **85** (10), 5805 (1986).

5. R. S. Judson and H. Rabitz, *Phys. Rev. Lett.* **68** (10), 1500 (1992).
6. A. Assion, T. Baumert, M. Bergt, T. Brixner, B. Kiefer, V. Seyfried, M. Strehle, and G. Gerber, *Science* **282** (5390), 919 (1998).
7. T. Brixner and G. Gerber, *ChemPhysChem* **4** (5), 418 (2003).
8. M. Dantus and V. V. Lozovoy, *Chem. Rev.* **104** (4), 1813 (2004).
9. M. Shapiro and P. Brumer, *Rep. Prog. Phys.* **66** (6), 859 (2003).
10. I. Walmsley and E. Rabitz, *Phys. Today* **56** (8), 43 (2003).
11. H. Rabitz, *Science* **299** (5606), 525 (2003).
12. T. Brixner, G. Krampert, T. Pfeifer, R. Selle, G. Gerber, M. Wollenhaupt, O. Graefe, C. Horn, D. Liese, and T. Baumert, *Phys. Rev. Lett.* **92** (20), 208301 (2004).
13. C. Daniel, *Science* **300** (5621), 903 (2003).
14. P. Kral, Z. Amitay, and M. Shapiro, *Phys. Rev. Lett.* **89** (6), 063002 (2002).
15. P. Kral and M. Shapiro, *Phys. Rev. A* **65** (4), 043413 (2002).
16. M. W. Noel and C. R. Stroud, *Phys. Rev. Lett.* **77** (10), 1913 (1996).
17. M. W. Noel and C. R. Stroud, *Phys. Rev. Lett.* **75** (7), 1252 (1995).
18. H. Wen, C. Rangan, and P. H. Bucksbaum, *Phys. Rev. A* **68** (5), 053405 (2003).
19. T. C. Weinacht, J. Ahn, and P. H. Bucksbaum, *Nature* **397** (6716), 233 (1999).
20. J. R. R. Verlet, V. G. Stavros, R. S. Minns, and H. H. Fielding, *Phys. Rev. Lett.* **89** (26), 263004 (2002).
21. R. S. Minns, R. Patel, J. R. R. Verlet, and H. H. Fielding, *Phys. Rev. Lett.* **91** (24), 243601 (2003).
22. R. S. Minns, J. R. R. Verlet, L. J. Watkins, and H. H. Fielding, *J. Chem. Phys.* **119** (12), 5842 (2003).
23. R. A. Bartels, T. C. Weinacht, N. Wagner, M. Baertschy, C. H. Greene, M. M. Murnane, and H. C. Kapteyn, *Phys. Rev. Lett.* **8801** (1), 013903 (2002).
24. M. Comstock, V. V. Lozovoy, and M. Dantus, *Chem. Phys. Lett.* **372**, 739 (2003).

25. M. Spanner, E. A. Shapiro, and M. Ivanov, *Phys. Rev. Lett.* **92** (9), 093001 (2004).

26. N. F. Scherer, R. J. Carlson, A. Matro, M. Du, A. J. Ruggiero, V. Romerorochin, J. A. Cina, G. R. Fleming, and S. A. Rice, *J. Chem. Phys.* **95** (3), 1487 (1991).

27. J. R. R. Verlet, V. G. Stavros, and H. H. Fielding, *Phys. Rev. A* **65** (3), 032504 (2002).

28. M. Leibscher and I. S. Averbukh, *Phys. Rev. A* **6304** (4), 043407 (2001).

29. E. A. Shapiro, M. Spanner, and M. Y. Ivanov, *Phys. Rev. Lett.* **91** (23), 237901 (2003).

30. K. Ohmori, Y. Sato, E. E. Nikitin, and S. A. Rice, *Phys. Rev. Lett.* **91** (24), 243003 (2003).

31. E. Schrodinger, *Naturewissenschaften* **14**, 664 (1926).

32. E. B. Alterman, C. T. Tahk, and D. J. Wilson, *J. Chem. Phys.* **44** (2), 451 (1966).

33. R. C. Baetzold, C. T. Tahk, and D. J. Wilson, *J. Chem. Phys.* **45** (11), 4209 (1996).

34. P. F. Enders and D. J. Wilson, *J. Chem. Phys.* **46** (2), 425 (1967).

35. E. B. Setchel and R. H. Schwartz, *Chem. Phys. Lett.* **83** (2), 350 (1981).

36. I. S. Averbukh and N. F. Perelman, *Phys. Lett. A* **139** (9), 449 (1989).

37. R. W. Robinett, *Phys. Rep.* **392**, 1 (2004).

38. S. I. Vetchinkin and V. V. Eryomin, *Chem. Phys. Lett.* **222** (4), 394 (1994).

39. S. I. Vetchinkin, A. S. Vetchinkin, V. V. Eryomin, and I. M. Umanskii, *Chem. Phys. Lett.* **215** (1-3), 11 (1993).

40. R. M. Bowman, M. Dantus, and A. H. Zewail, *Chem. Phys. Lett.* **161** (4-5), 297 (1989).

41. M. Gruebele and A. H. Zewail, *J. Chem. Phys.* **98** (2), 883 (1993).

42. T. Lohmuller, V. Engel, J. A. Beswick, and C. Meier, *J. Chem. Phys.* **120** (22), 10442 (2004).

43. M. J. J. Vrakking, D. M. Villeneuve, and A. Stolow, *Phys. Rev. A* **54** (1), R37 (1996).

44. V. G. Stavros and H. H. Fielding, *J. Chem. Phys.* **112** (21), 9343 (2000).

45. J. A. Ramswell, V. G. Stavros, J. Lei, Q. Hong, and H. H. Fielding, *Phys. Rev. A* **59** (3), 2186 (1999).

46. J. Wals, H. H. Fielding, J. F. Christian, L. C. Snoek, W. J. Vanderzande, and H. B. V. Vandenheuvell, *Phys. Rev. Lett.* **72** (24), 3783 (1994).

47. K. Muller-Dethlefs and E. W. Schlag, *Angew. Chem.-Int. Edit.* **37** (10), 1346 (1998).

48. F. Merkt, *Annu. Rev. Phys. Chem.* **48**, 675 (1997).

49. R. G. Daniel, J. S. Keller, D. Pines, and R. S. Berry, *Chem. Phys. Lett.* **182** (3-4), 275 (1991).

50. C. Bordas, P. Labastie, J. Chevaleyre, and M. Broyer, *Chem. Phys.* **129** (1), 21 (1989).

51. K. K. Verma, J. T. Bahns, A. R. Rajaeirizi, W. C. Stwalley, and W. T. Zemke, *J. Chem. Phys.* **78** (6), 3599 (1983).

52. P. Kusch and M. M. Hessel, *J. Chem. Phys.* **68** (6) (1978).

53. I. Jackowska, W. Jastrzebski, R. Feber, O. Nikolayeva, and P. Kowalczyk, *Mol. Phys.* **89** (6), 1719 (1996).

54. C. Bordas, M. Broyer, and J. L. Vialle, *J. Chem. Phys.* **92** (7), 4030 (1990).

55. J. L. Dunham, *Phys. Rev.* **41**, 721 (1932).

56. J. N. Bardsely, B. R. Junker, and D. W. Norcross, *Chem. Phys. Lett.* **37**, 502 (1976).

57. R. J. LeRoy, *University of Waterloo Chemical Physics Research Reports* **CP 642** (1996).

58. J. W. Cooley, *Math. Comput.* **15**, 363 (1961).

59. L. Pauling and E. B. Wilson, *Introduction to Quantum Mechanics*. McGraw-Hill, New York, 1935.

60. G. Herzberg, *Molecular Spectra and Molecular Structure 1. Spectra of Diatomic Molecules*. D. Van Nostrand Company, Inc., Princton, New Jersey, 1950.

61. L. D. Noordam, D. I. Duncan, and T. F. Gallagher, *Phys. Rev. A* **45** (7), 4734 (1992).

62. X. Chen and J. A. Yeazell, *Phys. Rev. A* **55** (4), 3264 (1997).

CHAPTER 5:

OPTICAL CONTROL OF ORBITAL ANGULAR MOMENTUM IN Na

This chapter presents an experimental and theoretical analysis of quantum interference between Rydberg wave packets in Na. This is achieved using pairs of phase-locked wave packets to manipulate the total orbital angular momentum of Na Rydberg atoms. Initially, the wave packet is composed of a superposition of *s* and *d* Rydberg series. Exploitation of the difference between the quantum defects of the two series allows one to predict the phase of the second wave packet required to engineer specific angular momentum compositions within the resultant wave packet. Experimentally, this final quantum state distribution is analysed in the frequency domain using state selective field ionisation, and in the time domain using the optical Ramsey method. The theoretical calculations show how the phase difference between pairs of optical pulses is linked to the corresponding Rydberg frequency spectrum, therefore enabling the control of the quantum state composition of the wave packets.

5.1 INTRODUCTION

During the last two decades, considerable advances in ultra-fast laser technology has led to an increasing interest in the study of Rydberg wave packets as a means to understand, and ultimately control, time-dependent quantum systems. Rydberg electron wave packets are spatially localised quantum states of an electron possessing both particle-like and wave-like properties. They were introduced briefly in chapter 2 and will be considered in more detail in this chapter.

The initial interest in electronic wave packets arose from the desire to understand the limit of the correspondence principle in atomic systems. It was understood that the classical motion of a projectile is captured in the motion of a wave packet, and could therefore provide a direct observation of classical mechanics emerging from quantum mechanics. The classical and quantum aspects of wave packet evolution have been analysed in detail and there are a number of comprehensive reviews of atomic Rydberg wave packets detailing their underlying theory [1,2] and their experimental generation and detection [3,4]. However, during the last few years a dramatic shift has occurred from the observation of wave packets to their customisation, manipulation and control [5-8].

The process of wave packet control involves the manipulation of quantum interferences within an atomic or molecular system by adjusting various external experimental parameters, for example, the phase difference between a pair of laser pulses. Various control schemes have been devised to tackle a range of problems in Rydberg atoms, including the creation of Schrödinger's cat-states [9,10], control of angular momentum [11-15] and quantum computing techniques [16-21]. Moving to molecular Rydberg systems, control of the photodissociation [22] and rotational angular momentum in NO [23] has been achieved, as well as the control of rotational wave packet dynamics [24-27].

More recently, there has been an increasing interest in the extension from small molecules to large, polyatomic molecules [28]. For example, a number of control

experiments employing learning algorithms have been performed on organometallic substances [29]. One important aim in the control of large molecules is the extension to the biological realm. Control over various degrees of freedom in organic systems could ultimately lead to the probing and manipulation of biological functions [30].

One major obstacle in the control of polyatomic systems is the lack of understanding of the spectroscopic details of the system. The work in this chapter returns to a simple atomic system, and an intuitive control scheme, with the aim to understand the underlying physics of the problem.

Both coherent control schemes presented involve the use of a pair of phase locked pulses to manipulate the *s* and *d* angular momentum components of a wave packet in Na. In the first scheme, two wave packets separated by one classical orbit period are phase-shifted in order to separate the angular momentum components in the resultant wave packet. The populations of these Rydberg states are investigated using state selective field ionisation (SSFI), and are the first experimental observation of angular momentum separation in an atomic system and are in excellent agreement with calculations.

In the second scheme, two wave packets separated by 1.5 classical orbit periods are phase-shifted in order to spatially localise the angular momentum components at different locations on the electronic orbit. This localisation is demonstrated experimentally using a third phase-locked pulse in a Ramsey-type experiment, and the dynamics are verified using a modified autocorrelation calculation. In both schemes, the theoretical calculations show how the phase difference between pairs of optical pulses is linked to the corresponding Rydberg frequency spectrum, therefore enabling control of the quantum state composition of the wave packets through a logical control scheme.

5.2 DYNAMICS OF RYDBERG ELECTRON WAVE PACKETS

The dynamics of electron wave packets were discussed briefly in chapter 2. In this section, a more detailed description of the dynamics of Rydberg electron wave packets is presented. A Rydberg state is a highly excited electronic state of an atom or molecule, where at least one electron has a high principal quantum number, n. Classically, such a state corresponds to putting one electron into an orbit whose dimensions are very large compared to the size of the ion core. The energy distribution of Rydberg states is given by the Rydberg formula:

$$E_n = -\frac{R}{n^2}, \tag{5.1}$$

where

$$R = \frac{\mu e^4}{8\varepsilon_0^2 h^3 c} \tag{5.2}$$

is the Rydberg constant. In (5.2) the reduced mass is represented by μ and the fundamental constants are as follows: e = charge of an electron, ε_0 = vacuum permittivity constant, h = Planck's constant and c = the speed of light. (5.1) describes the total energy of an electron with high principal quantum number n, and shows that the energy spacings between consecutive states scales as $1/n^3$. This is significant in wave packet creation as the separation between the energy levels becomes small very rapidly with decreasing binding energy. On approaching the ionisation limit, adjacent Rydberg states lie very close in energy making it possible for the coherent bandwidth of an ultrafast laser pulse to excite a number of stationary states, creating a spatially localised and time-dependent Rydberg wave packet.

Initially, the wave packet mimics a classical electron by travelling within the Coulombic potential. At its maximum potential energy, at the outer turning point of the

orbit, the wave packet is pulled back to the core with high kinetic energy. From classical mechanics, a bound particle in a Coulomb potential moves in an elliptical orbit according to Kepler's third law: *the square of the orbit period is proportional to the cube of the semi-major axis of the elliptical orbit* [31],

$$T^2 = 2\pi a^3, \tag{5.3}$$

where the expression for the semi-major axis is $a = 1/2|E|$. In a Rydberg atom, the energy E, is related to $\bar{n}$, the average principal quantum number in the superposition by $E = -1/2\bar{n}^2$. As discussed in chapter 2, the energy difference ΔE_n, between the constituent states in the superposition is related to the orbit period of the wave packet by $T_{cl} = 2\pi/\Delta E_n$. Using the fact that the energy difference of adjacent levels in Rydberg series is proportional to $1/n^3$, the following classical relation between orbit period and energy is obtained:

$$T_{cl} = \pi\left(1/2E^3\right)^{1/2} = 2\pi\bar{n}^3 \tag{5.4}$$

When a coherent superposition of Rydberg states is excited, the resultant time-dependent wave packet is of the form

$$\Psi(r,t) = \sum_n a_n \psi_n(r,\theta,\phi) e^{-i\omega_n t}, \tag{5.5}$$

where the sum is over all the states contributing to the superposition, and $\psi_n(r,\theta,\phi)$ represents the radial and angular components of the corresponding wavefunctions. The specific contribution of each state to the superposition is determined by the amplitude factor a_n, which in turn, depends on the transition dipole moments $\langle \psi_{nl}|r|\psi_g \rangle$ [32], from the ground state ψ_g to the Rydberg states, and the excitation profile of the laser field.

If the excitation is from a low-lying state, the electric dipole transition selection rules dictate that the orbital angular momentum may only change by one unit and therefore, it is usual for one or two Rydberg series to dominate the superposition. Equation (5.5) can therefore often be reduced to a sum over the radial coordinate only, incorporating angular momentum states within the radial summation:

$$\Psi(r,t) = \sum_{nl} a_{nl}\psi_{nl}(r)e^{-i\omega_n t} \tag{5.6}$$

The calculations and experimental results in this chapter are all investigations of radial wave packet dynamics. If more than one Rydberg series is present in the superposition, the resulting radial dynamics will show an angular dependence. The time-dependent behaviour of Rydberg wave packets has been predicted and observed in several groups [33-38].

The principal dynamical difference between radial Rydberg wave packets and vibrational wave packets is due to the significant anharmonicity of the Coulomb potential in comparison to the Morse potential. For example, in Na, a wave packet excited from a single Rydberg series at around n = 28, with a 0.7 ps pulse, contains approximately 3 Rydberg states with appreciable intensity. This wave packet begins to spread and delocalise after one classical orbit period, i.e. within around 5 ps. This is in stark comparison to vibrational wave packets. A vibrational wave packet excited around the v = 15 state in the $A^1\Sigma_u^+$ state in Na_2, with a 50 fs pulse, will also contain approximately 3 states. This wave packet oscillates for over 8 ps (32 classical orbit periods) before the first sign of dispersion. In both of these examples, the second order partial revival occurs around 20 ps. However, the vibrational wave packet has completed more that 80 oscillations before it is dispersed enough to form a the second order partial revival, whereas the Rydberg electron wave packet only needs to undergo 5 oscillations to achieve the second order partial revival.

5.3 SPECTROSCOPY OF Na

5.3.1 THE QUANTUM DEFECT

Spectroscopically, a Rydberg series is a set of bound states of the excited electron for a given angular momentum quantum number and ion core state. In quantum defect theory terms, this constitutes a channel. For a channel that is not interacting with any others, the Rydberg state energies follow a simple formula:

$$E_n = -\frac{R}{(n-\mu)^2} \tag{5.7}$$

where n is the principal quantum number, R is the Rydberg constant for the system and μ is the quantum defect. The quantum defect describes how much the Rydberg series departs from the behaviour of the Rydberg states of atomic hydrogen, and is directly related to the interaction of the excited electron with the ion core.

A Rydberg atom has a positive nucleus and therefore produces an electric field, which is shielded by the electrons in inner orbits. Depending on the value of the angular momentum quantum number l, the shielding experienced by the outer electron is not constant at all points in its orbit. The quantum defect accounts for the variation in shielding the electron experiences, and has high values for states of low angular momentum, as these electrons experience little or no shielding. The quantum defect is therefore regarded as a measure of core-electron interaction at short range; it vanishes for non-penetrating high-l Rydberg states.

Investigations into the effect of the quantum defect on Rydberg states becomes more complex when one considers an energy region where there are states associated with more than one channel. For example, these channels might be associated with different spin-orbit states of the ion core in an atom, or different rotational and

vibrational states of a molecular ion core. Interactions between channels give rise to coupling between the states of different channels, which in turn leads to energy shifts and intensity variations in the Rydberg series resulting in either a mixing of bound states or autoionisation. Multi-channel Quantum Defect theory (MQDT), provides a unified treatment of both open and closed coupled channels [39-41].

The quantum defect is a measure of how strongly the outer electron interacts with the core electrons, and therefore is affected by the orbital angular momentum of the outer electron. As the orbital angular momentum, ℓ, increases, the elliptical orbit of the electron becomes more circular. In this case, the electron is far from the core at all times and core penetration is therefore minimal. Conversely, when ℓ becomes smaller, the orbit becomes strongly elliptical and in the limit of zero orbital angular momentum, the orbit is a straight line and there is significant penetration into the core region. In Na, a transition from the $^2P_{3/2}$ state results in excitation of the *s* and *d* Rydberg series. The *s* states ($l = 0$) will have a large quantum defect in comparison to the *d* states ($l = 2$).

5.3.2 ENERGY LEVELS AND OSCILLATOR SRENGTHS

In order to calculate the wave packet dynamics and corresponding populations, preliminary calculations were performed incorporating the energy levels in Na and their relative intensities within a wave packet. There are a number of factors that contribute to the distribution of states within an electron wave packet. Aside from the external parameters attributed by the laser pulse, i.e. its profile and bandwidth, the rules and features governing atomic transitions play an important role in the final distribution of states in a wave packet.

On photon absorption, the electric dipole transition selection rules dictate that the orbital angular momentum may only change by one unit. Therefore, in the absence of external fields, a transition from the *p* state in sodium will result in the excitation of

only s and d series. Figure 5.1 is the excitation scheme illustrating the relevant transitions to the Na Rydberg states.

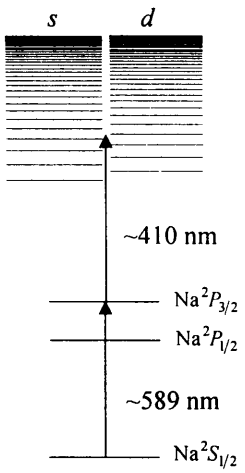

Figure 5.1 Excitation scheme illustrating the relevant transitions in Na. All the experiments and calculations presented in this chapter occur via the $\mathrm{Na}\,^2P_{3/2}$ state .

The Na transition energies were calculated using equation (5.7) where $R_{\mathrm{Na}} = 109734.697\ \mathrm{cm}^{-1}$. The Na Rydberg constant was calculated from the most recent recommended values for R_∞, and the masses of the sodium atom and the electron [42]. The quantum defects for the s and d series are $\delta = 0.35$ (in modulo 1) and $\delta = 0.0$ respectively [43].

Another important factor governing electronic transitions is the oscillator strength, defined as *the ratio of the strength of a transition to that of an electric dipole transition between two states of an electron oscillating harmonically in three dimensions* [44]. Experimentally, the average oscillator strength is a dimensionless quantity describing the relative intensity of electronic transitions. However, a convenient way of expressing the strength of electronic transitions from a level nl to a level $n'l'$, is with the average oscillator strength $\bar{f}_{n'l',nl}$:

$$\bar{f}_{n'l',nl} = \frac{2}{3}\omega_{n'l',nl}\frac{l_{\max}}{2l+1}\left|\langle n'l'|r|nl\rangle\right|^2 \tag{5.8}$$

where $\omega_{n'l',nl} = (E_{n'l'} - E_{nl})/\hbar$ is the energy separation between the Rydberg states, and $l_{\max}$ is the larger of l and l'. Through substitution of appropriate values for l, l' and $l_{\max}$ into (5.8), the relative strengths of the $(ns, nd \leftarrow 3p)$ transitions in Na can be calculated:

$$\frac{\bar{f}_{ns,3p}}{\bar{f}_{nd,3p}} = \frac{\omega_{ns,3p}}{\omega_{nd,3p}} \frac{(1/3)}{(1/2)} \frac{|\langle ns|r|3p\rangle|^2}{|\langle nd|r|3p\rangle|^2} = \frac{1}{2}. \tag{5.9}$$

As shown by (5.9), the oscillator strengths for the transitions to the *s* and *d* Rydberg series have a ratio of 1:2 [45]. Therefore, a wave packet created from a superposition of *s* and *d* Rydberg states will have twice as much *d* character as *s* character, significantly affecting the resulting dynamics.

The effect on the wave packet dynamics is illustrated in figure 5.2.

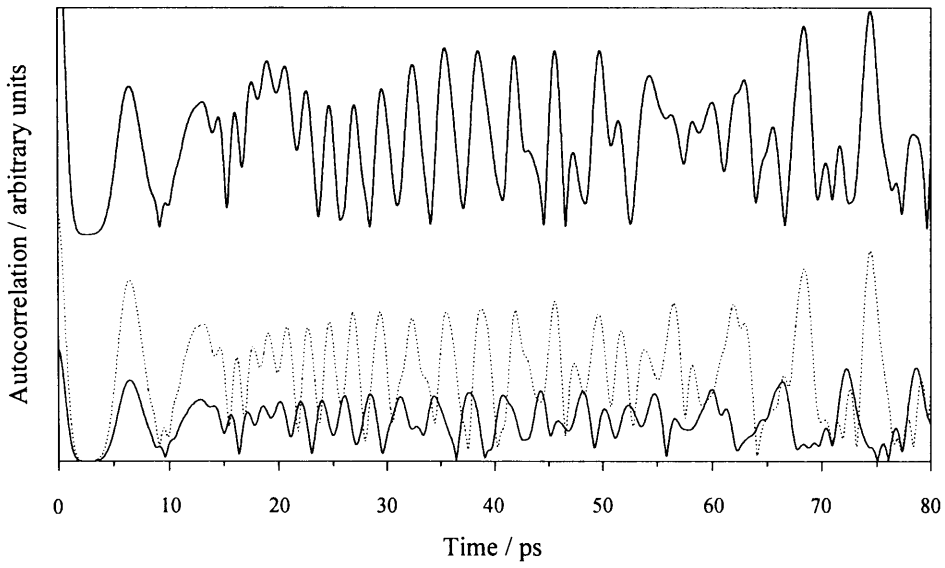

Figure 5.2 Upper trace: calculated recurrence spectrum for a wave packet excited around n = 35 in Na. The first reconstruction of the wave packet occurs at around 70 ps. The lower trace represents the same wave packet, but deconvoluted into its *s* and *d* components. The plots illustrate the dominance of the *d* states in the superposition due to the 2:1 oscillator strength ratio of the *d* /*s* states in the superposition.

The upper plot is a calculated recurrence spectrum of a wave packet excited around n = 35 in Na, with a 0.7 ps pulse, corresponding to a bandwidth of 21 cm^{-1}. The lower trace shows the same wave packet, but deconvoluted to its *s* and *d* components, represented by the solid and dotted lines respectively.

It is evident that the dynamics of the wave packet are very similar to the *d* component of the wave packet, reflecting the dominance of the *d* Rydberg states in the superposition due to its higher oscillator strength in comparison to the *s* states. Also evident in the lower trace is the natural separation of the *s* and *d* components at around 70 ps – the first reconstruction of the wave packet. Achieving this type of spatial separation of the angular momentum components at unusual points in the wave packet evolution is the focus of the one of the coherent control schemes presented in this chapter.

5.4 THE CONTROL SCHEME

The background required to understand the mechanism behind the control scheme was described in chapter 2 with reference to wave packet interference in atomic hydrogen. In this section, the theory is discussed briefly, but related, where needed, to the atomic Na system. The approach is based on interfering wave packets, where an initial launch state g is coupled to a set of Rydberg states n by a sequence of laser pulses. The form of the resulting electric field is given by equation (2.13). The solution of the time-dependent Schrödinger equation is expressed as

$$\Psi(r,t) = a_g(t)\psi_g(r)e^{-i\omega_g t} + \sum_n a_n(t)\psi_n(r)e^{-i\omega_n t} \tag{5.10}$$

where a_n and ω_n are the amplitudes and angular frequencies of the Rydberg state, and a_g and ω_g are the corresponding quantities for the launch state, in this case the $^1S_{1/2}$

state of Na. Using standard time-dependent perturbation theory, it was shown in chapter 2 that the probability amplitudes of the Rydberg states after a sequence of k pulses are

$$a_n(t) = -\frac{i}{2}\Omega_n g_n \left[1 + \sum_k e^{i\Delta_n t_k} e^{i\omega t_k}\right]. \tag{5.11}$$

where $\Delta_n = \omega_n - \omega_g - \omega$, $\Omega_n = eE_0\langle n|z|g\rangle/\hbar$ is the Rabi coupling and $g_n = \exp\left[-(\Delta_n \tau_p)^2/8\ln 2\right]$ is the spectral amplitude of the pulses. For an individual Rydberg state n, the interference term in square brackets oscillates rapidly with the angular frequency, $\omega_n - \omega_g$, i.e. with the same angular frequency as the component of the light field that excited that state. For a wave packet composed of a superposition of Rydberg states, these oscillations beat in and out of phase with one another. If only one Rydberg series contributes to the wave packet, this beating can be characterised by making use of the expansion,

$$\omega_n = -1/2n^2 = -1/2\bar{n}^2\left[1 - 2\,\delta n/\bar{n} + 3(\delta n/\bar{n})^2 - \cdots\right], \tag{5.12}$$

where $\delta n = (\bar{n} - n)$ and $\delta n << \bar{n}$. Here, $\bar{n}$ represents the centre of the wave packet and is related to the central angular frequency of the laser field, $\omega = -1/2\bar{n}^2$. The first term in the expansion represents the average oscillation frequency of the population amplitude of the wave packet. The second term in the expansion is linear in δn. It represents the harmonic dephasing and rephasing of the individual amplitude components and corresponds to the classical oscillation period of a Rydberg wave packet in the radial coordinate $T_{cl} = 2\pi\bar{n}^3$. The third term in the expansion is quadratic in δn and introduces anharmonicity into the wave packet.

When just one optical pulse is used to excite a Rydberg wave packet, the amplitudes of the states in the superposition reflect the Gaussian distribution of the intensity profile of the laser pulse, and by adding a second laser pulse, interference is

generated in the system, the result of which depends on the phase difference between the optical pulses.

In a similar way to the vibrational wave packet control scheme discussed in chapter 4, two temporally overlapping optical pulses are separated by a time, $t_\phi << \tau_p$, where $t_\phi = \phi/\omega$ corresponds to an optical phase shift ϕ with reference to the optical frequency ω. When $\phi = 2m\pi$ $(m = 0,1,2,\ldots)$ the optical pulses are in phase with one another and interfere constructively, and when $\phi = (2m+1)\pi$ $(m = 0,1,2,\ldots)$ the optical pulses are out of phase with one another and interfere destructively. In atomic systems, the optical intensity determines the final Rydberg state population and, correspondingly, fringes would be observed in the total Rydberg population, $\sum_n a_n^2(t)$, at the optical frequency.

The important cases to consider are when the two optical pulses are temporally separated by a time $t \approx T_{cl}/2 > \tau_p$ and by a time $t \approx T_{cl}$, which were both discussed in detail in chapter 2. Referring back to figure 2.2, the spectral profile of a single Gaussian bandwidth limited pulse $(\tau_p = 0.7\,\text{ps})$, with central frequency corresponding to excitation of the $40p$ level in the H atom from the $1s$ launch state, is plotted, together with the spectral intensities of pulses sequences, obtained from the Fourier transforms of pairs of identical pulses, with delays corresponding to (b) $T_{cl}/2$, (c) T_{cl}, (d) $T_{cl} + \pi/\omega$, (e) $3T_{cl}/2$.

The Fourier transform of two Gaussian pulses with central angular frequency ω separated by a delay T gives a comb of frequencies at $\omega + 2m\pi/T$ $(m = 0,1,2,\ldots)$ with the same frequency envelope as the single pulse. Therefore, when $T = T_{cl}$ the peaks in the frequency comb coincide (to first order) with the excitation frequencies of the Rydberg states and the total Rydberg population is $\sum_n \Omega_n^2 g_n^2$. Increasing the delay between the two optical pulses by a time corresponding to half an optical cycle, i.e. $T = T_{cl} + \pi/\omega$, translates the modulation in the frequency spectrum by π, so that the dips in the frequency comb correspond (to first order) with the excitation frequencies of the Rydberg states and the total Rydberg population is zero. For a pulse separation $T = T_{cl}/2$, the peaks in the frequency comb coincide with the excitation frequencies of

alternate Rydberg states in the superposition, in this example, the odd Rydberg states. Therefore, to first order, the total Rydberg population is $\sum_{odd} \Omega_n^2 g_n^2$.

5.5 THE QUANTUM DEFECT AND WAVE PACKET DYNAMICS

A wave packet consisting of two Rydberg series may be pictured as consisting of two independent components, each of which has its own electronic orbital angular momentum l, and associated quantum defect μ_l. Referring back to equation (5.6), where $\psi_{nl}(r)$ is the radial wavefunction of the eigenstate $|nl\rangle$ and a_{nl} is its amplitude in the superposition, the quantum defect can be effectively introduced by expressing the angular frequency (in atomic units) as

$$\omega_{nl} = -1/2(n-\mu_l)^2. \tag{5.13}$$

The effect of the quantum defect of a Rydberg series on the dynamics of a wave packet is illustrated by introducing the effective principal quantum number, $\nu_{nl} = n - \mu_l$, and then expanding the frequency dependent term in the exponential of (5.6) as a Taylor's series:

$$\exp[i\omega_{nl}t] = \exp\left[-\frac{i}{2\bar{\nu}^2}\left[1-2\left(\frac{\delta\nu}{\bar{\nu}}\right)+3\left(\frac{\delta\nu}{\bar{\nu}}\right)^2-\cdots\right]t\right], \tag{5.14}$$

where $\delta\nu = (\bar{\nu} - \nu_{nl})$, $\delta\nu << \bar{\nu}$ and $\bar{\nu}$ represents the centre of the wave packet. The first term in (5.14) is the average energy of the wave packet. The second term, which relates to the classical oscillation period of the wave packet, can be rewritten as

$$\exp\left[-\frac{i(n-\bar{n})t}{\bar{\nu}^3}+\frac{i\mu_l t}{\bar{\nu}^3}\right] = \exp\left[-2\pi i(n_l-\bar{n})\frac{t}{T_{cl}}\right]\exp\left[2\pi i\mu\frac{t}{T_{cl}}\right]. \tag{5.15}$$

The first term in (5.15) is simply the classical orbit period of the wave packet. However, the second term has the effect of phase shifting the Rabi oscillations, resulting in a total accumulated phase difference between the probability amplitudes of the two Rydberg series. Therefore, after a time t given by the Rabi oscillations will have phase shifted by an amount

$$\phi = 2\pi k\Delta\mu . \tag{5.16}$$

where $k = t/T_{cl}$ and $\Delta\mu$ is the quantum defect difference between the two Rydberg series contributing to the superposition. The quantum defect difference between two series in a wave packet superposition has an effect on the recurrence spectrum through introduction of a slow modulation onto the spectrum. The period of the oscillation corresponds to the quantum beat between the *s* and *d* series:

$$t_{\mu} = T_{cl} / \Delta\mu , \tag{5.17}$$

The magnitude of the quantum defect has an important effect on the wave packet dynamics. Figure 5.3 illustrates this effect with a series of calculated recurrence spectra with differing quantum defects. Plot (a) is a generic recurrence spectrum created from the excitation of one Rydberg series (in this case, the *d* series in Na), with a 0.7 ps pulse. Plot (b) is a recurrence spectrum of a wave packet created from two identical series with a quantum defect difference, $\Delta\mu = 1/2$. Application of equation (5.16) reveals that after one classical orbit period, the two series will be π out of phase with one another. This is evident in plot (b) as there is no wave packet intensity at T_{cl}. After two classical oscillations, the two series are in phase with one another, as shown by the intense peak at $2T_{cl}$. Plot (c) illustrates the opposite situation; this wave packet is created from two series with a quantum defect difference, $\Delta\mu = 1/4$. In this case, after $2T_{cl}$, the two series are π out of phase. Coherent control schemes aiming to manipulate

the angular momentum components of two Rydberg series, could be successfully implemented at T_{cl} in a system with $\Delta\mu = 1/2$ and $2T_{cl}$ in a system with $\Delta\mu = 1/4$. In fact, the *s* and *d* series in Xe have $\Delta\mu = 1/4$, and successful control of the angular momentum components has been demonstrated in wave packet experiments with two phase-locked pulses [13]. The removal of either the *s* or *d* series from the wave packet superposition markedly altered the dynamics, by either enhancing or depleting the strength of the angular beat on the recurrence spectrum.

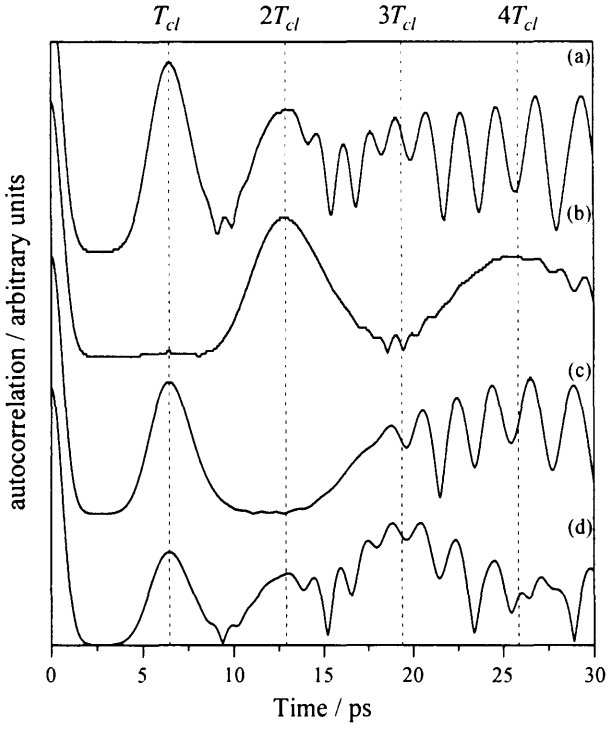

Figure 5.3 Calculated wave packet recurrence spectra of a set of theoretical wave packets. The vertical dashed lines represent positions of the first three classical orbit periods. Plot (a) is a single series wave packet presented for reference. Plots (b) – (d) are recurrence spectra of wave packets consisting of two series, with the same intensities, but with quantum defect differences between the series of $\Delta\mu = 1/2$, 1/4 and 1/3 respectively. In plot (b), the two series are in phase with one another after $2T_{cl}$, and are exactly π out of phase at T_{cl}. The opposite situation occurs in plot (c). Plot (d) illustrates the case where $\Delta\mu = 1/3$, analogous to the *s* and *d* series in Na. At both T_{cl} and $2T_{cl}$, the two series are partially in phase with one another . At $3T_{cl}/2$, the two series are π out of phase with one another.

The case relevant to this work is illustrated with plot (d). This wave packet was created with a quantum defect difference, $\Delta\mu = 1/3$, which is almost the quantum defect difference between the *s* and *d* series in Na. This wave packet has peaks at both T_{cl} and $2T_{cl}$, at which the two series are $2\pi/3$ and $\pi/3$ out of phase respectively. In light of this, a more complex control scheme is required to control the angular momentum distribution in Na after one classical oscillation, as the states do not have a phase relationship that is a multiple of π. In addition, the resultant wave packet dynamics would not be readily observed, as there is only partial interference in the core region. This is in contrast to maximum interference observed in the core region in the Xe system.

A more direct method of observing the angular momentum is SSFI, which was used in this case to observe the phase evolution of the *s* and *d* states in Na after one classical oscillation. Referring back to plot (d), there is an interval of complete destructive interference between the *s* and *d* states at $3T_{cl}/2$. Therefore, any coherent control scheme implemented at this time interval would be readily observed in the wave packet dynamics, as is demonstrated in section 5.7.

5.6 EXPERIMENTAL DETAILS

An outline of the experimental techniques employed for wave packet and SSFI experiments in Na is described in this section. For details of the various techniques, see chapter 3. Coherent superpositions of Na Rydberg states were excited in a resonance-enhanced one-nanosecond plus one-picosecond ($1_{ns} + 1_{ps}$) excitation process. To access the intermediate $^2P_{3/2}$ state, the output of a Nd:YAG pumped nanosecond dye laser was tuned to resonance with the $^2P_{3/2} \leftarrow ^1S_{1/2}$ transition in Na at 589.16 nm. The dye-amplified output of a synchronously-pumped picosecond dye laser was frequency-doubled to generate pulses of near-ultraviolet radiation (~410 nm) with bandwidth of approximately 20 cm^{-1}, and a feedback-stabilised Michelson interferometer was

employed to generate sequences of two or three pulses with precisely determined optical phase difference ($\pm \pi / 5$) [46]. After the interferometer, the nanosecond and picosecond radiation were focused collinearly into an atomic beam of Na to excite a superposition of *s* and *d* Rydberg states converging to the Na^+ ionisation limit. The subsequent dynamics of the wave packet were determined using the optical Ramsey method, which measures the total Rydberg population after a sequence of optical pulses [4]. Approximately 70 ns after laser excitation, a pulsed electric field (2 kV cm^{-1} with ~10 ns rise time) field-ionises the Rydberg states and accelerates them along a 20 cm flight tube towards a microchannel plate detector (MCP). The resultant preamplified electron signal is typically averaged over 10 laser shots for a given delay. The total population $\sum_n a_n^2(t)$ is recorded as a function of the delay time between the laser pulses. Fringes are observed in the total Rydberg population at the optical frequency. The root-mean-square of the fringes is calculated and provides a measure of the autocorrelation function of the wave packet. In addition, the population amplitudes of the individual eigenstates in the wave packet were measured directly by using state selective field ionisation (SSFI). Approximately 100 ns after laser excitation, a ramped electric field with a slow slew rate (~700 V cm^{-1} μs^{-1}) field-ionises the various components of the wave packet in succession and accelerates the electrons along a 20 cm flight tube towards the MCP. The resultant current is preamplified and monitored on a 500 MHz digital oscilloscope interfaced to a personal computer (PC).

Frequency spectra of the Na Rydberg states were also recorded. The $^2P_{3/2} \leftarrow ^1 S_{1/2}$ transition in atomic sodium (589.15 nm) was excited with a narrow bandwidth nanosecond dye laser (Sirah Precisionscan) pumped with approximately 60% of the second harmonic of a Q-switched nanosecond Nd:YAG laser (Continuum Powerlite 8010). The remaining 40% of the Nd:YAG laser was used to pump a Continuum ND-6000 dye laser operating with the dye Rhodamine 610 dissolved in methanol (0.11 g L^{-1}), which has a wavelength range of 578 – 610 nm.

The Na Rydberg states were accessed with a second nanosecond dye laser (Sirah Precisionscan) pumped with the frequency tripled output of the nanosecond Nd:YAG (1

W, 100 mJ pulse^{-1}). The dye laser was operated with Exalite 411 (0.13 g L^{-1} in para-dioxane), and had an output pulse power of 10 μJ pulse^{-1} at 410 nm. As before, the collinear laser beams intersect the Na beam in the interaction region, where an electric field accelerates the ions towards an MCP detector. The current at the MCP is preamplified and monitored on a 500 MHz digital oscilloscope interfaced to a personal computer.

5.7 RESULTS

5.7.1 Na FREQUENCY SPECTRA

The frequency spectrum of a set of Rydberg states in Na is presented in figure 5.4.

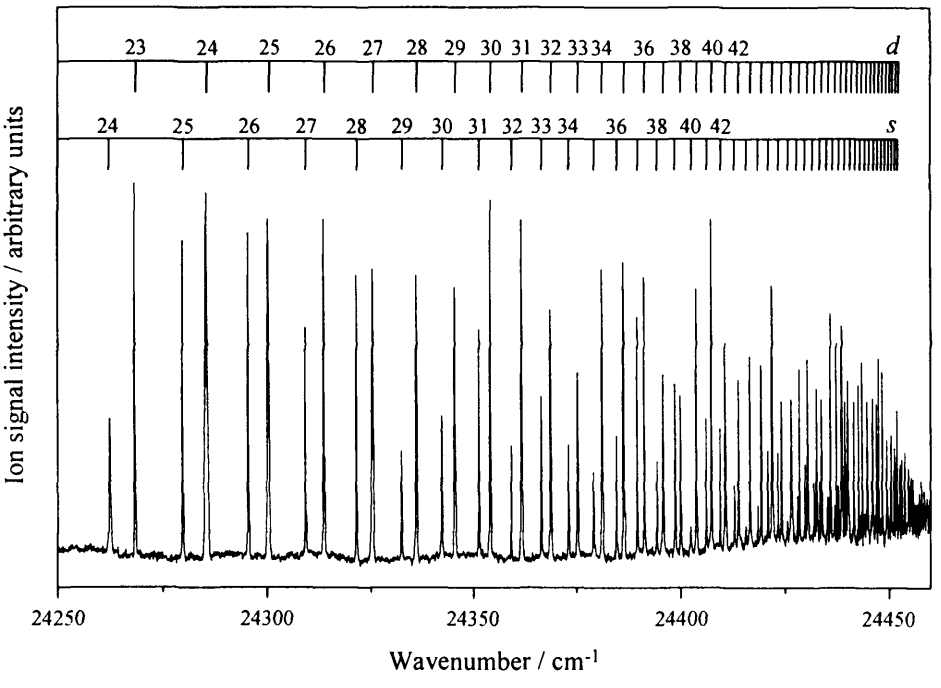

Figure 5.4 Frequency spectrum of Na over the region of n = 24 to the ionisation limit. The positions of the s and d Rydberg series are also plotted. Note: the x-axis is plotted as transition energy in wavenumbers, not the absolute energies of the Rydberg states.

The Na Rydberg states range from n = 24 and are resolved up to around n = 60, at which point the ionisation continuum obscures the features. The *s* and *d* doublets are visible, and the *d* series is more intense than the *s* series, illustrating the dominance of the *d* transition strength.

Figure 5.5 is a higher resolution frequency spectrum of the n = 31 - 40 states in Na, overlaid with a Gaussian profile representing a 0.7 ps laser pulse, corresponding to a bandwidth of 21 cm^{-1}. The Gaussian profile is centered on the 35*d* state, which is the central state of the wave packets in the control experiments presented in this chapter.

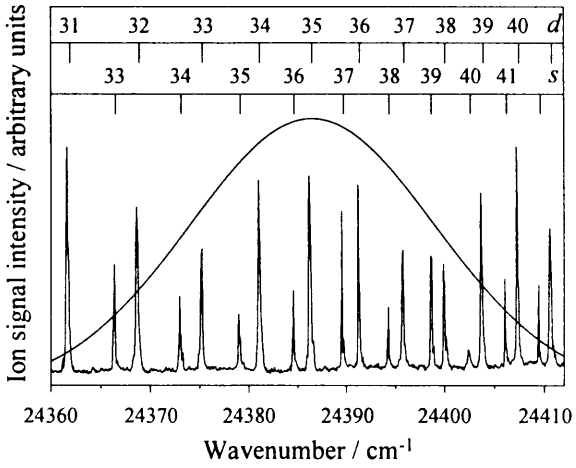

Figure 5.5 Frequency spectrum of Na Rydberg states illustrating the region of the spectrum where the wave packet control experiments take place. The Gausian profile overlaying the spectrum represents the laser pulse profile, and illustrates the range of states that would be excited for a wave packet centered around n = 35 with a 0.7 ps (21 cm^{-1} bandwidth) laser pulse

5.7.2 WAVE PACKETS IN Na

In figures 5.6 and 5.7, wave packet recurrence spectra are presented for a range of average principal quantum number, $\bar{n}$, all excited with a 0.7 ps laser pulse, corresponding to a bandwidth of 21 cm^{-1}. In all the spectra, the lower trace represents

the experimental results and the upper trace is the corresponding calculated spectrum. The low energy regime is illustrated in figure 5.5. In (a), the wave packet has an average principal quantum number $\bar{n} = 25$, and oscillates between the core and outer turning point with a period $T_{cl} = 2.4$ ps. In this case, there is only a significant contribution from two Rydberg states and consequently there is no dispersion. In figure 5.6(b) the wave packet has an average principal quantum number $\bar{n} = 28$ and at this slightly higher energy, the Rydberg states are now sufficiently close together so that 3 states are present in the superposition. The classical oscillation period has decreased to 3.3 ps and a second order partial revival is observed at t = 15.6 ps.

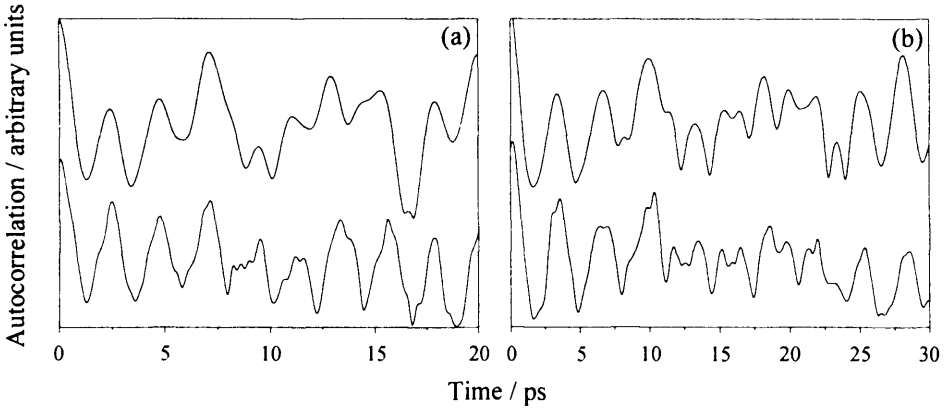

Figure 5.6 Wave packet recurrence spectra in Na for wave packets excited around (a) n = 25 and (b) n = 28, with a 0.7 ps laser pulse, corresponding to a bandwidth of 21 cm^{-1}. In both cases, the upper, dashed trace is the calculated plot, whilst the lower trace represents the experimental data. In both cases there is good agreement between experiment and theory.

Increasing the excitation energy (keeping the bandwidth of the laser constant), ensures that more states are included in the superposition as the energy separation between adjacent states scales as n^{-3}. In figure 5.7, a wave packet spectra excited around $\bar{n} = 35$ is presented. In this case, at least 6 states have a significant contribution to the wave packet resulting in faster dispersion and the formation of higher order partial revivals.

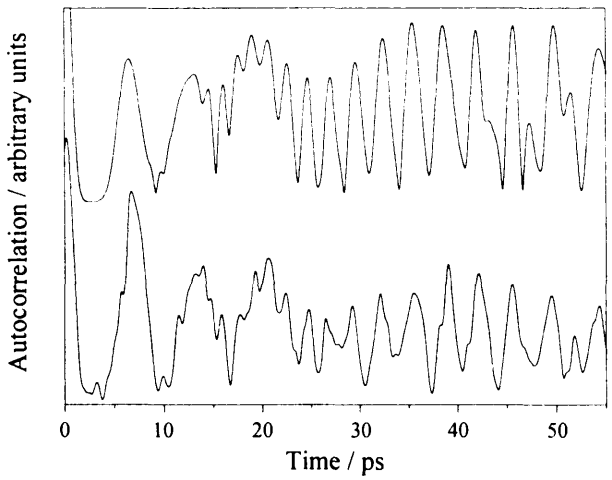

Figure 5.7 Experimental (lower trace) and calculated (upper trace) recurrence spectra of a wave packet excited around n = 35 in Na. There is evidence of a second, third and fourth order partial revival.

The spectrum clearly shows a second order partial revival at t = 38.0 ps, a third order partial revival at t = 25.3 ps and hints of a fourth order partial revivals at 19.0 ps. Also, due to the reduction of the average energy gap between the Rydberg states, the classical oscillation period of the wave packet has increased to $T_{cl} = 6.5$ ps.

In figure 5.8 experimental (lower trace) and calculated (upper trace) wave packet spectra for average principal quantum number n = 31 are presented. The spectrum illustrates a second order partial revival at t = 23.4 ps and a full revival at t = 47.8 ps. A slow beat in the form of a cosine wave with a period 12.9 ps, is superimposed on the spectrum. The oscillation is a consequence of the difference in quantum defects between the s and d Rydberg series excited by the laser pulse, discussed in section 5.6. The period of the angular beat, is $t_\mu = T_{cl} / \Delta\mu$ where $T_{cl} = 4.5\,\text{ps}$ and $\Delta\mu = 0.35$ is the difference between the quantum defects of the s and d series (in modulo 1). Figure 5.8(c) is a calculated plot of the Rydberg state population of the wave packet, employing a 0.7 ps Gaussian pulse. The white bars represent the d series and the black bars the s series.

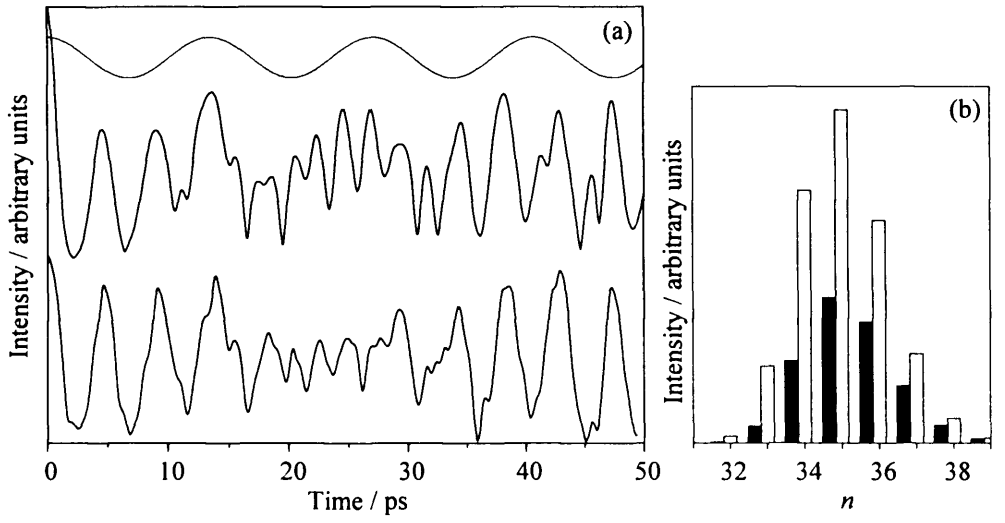

Figure 5.8 Plot (a) is a recurrence spectrum of a wave packet excited around n = 31 in Na. The upper trace is a calculated spectrum and the lower is experimental data. There is evidence of a slow oscillation with period $t_\mu = 12.9$ ps, represented as a cosine wave overlaying the spectra, which illustrates the influence of the quantum defects on the radial dynamics of the wave packet. Plot (b) is a calculated population distribution of the s and d states within the wave packet. As before, the black and white bars represent the s and d components respectively.

To demonstrate the initial classical dynamics of this system, a plot of the classical orbit period as a function of average principal quantum number is presented in figure 5.9. As the energy spacing scales as n^{-3}, the orbit period will scale as n^3 and is plotted as a solid line. The classical orbit periods were determined in a range of wave packet spectra over varying $\overline{n}$, by fitting a Gaussian profile to the first recurrence peak of each spectrum; this data is plotted as circles. The agreement is excellent as expected for a simple atomic system like Na.

The transition energy corresponding to the average principal quantum number in figure 5.9 is subject to some uncertainty, due to the broad bandwidth of the picosecond laser pulse. The excitation wavelength was determined with a wavelength meter (Angstrom WS-7), which has an error in the wavelength of 0.002 nm. This corresponds to an error of 0.5 % for an excitation around n = 20 and an error of 2.5 % for an

excitation around $n = 40$. This degree of uncertainty is relatively minor and is less than the width of the circles in figure 5.9.

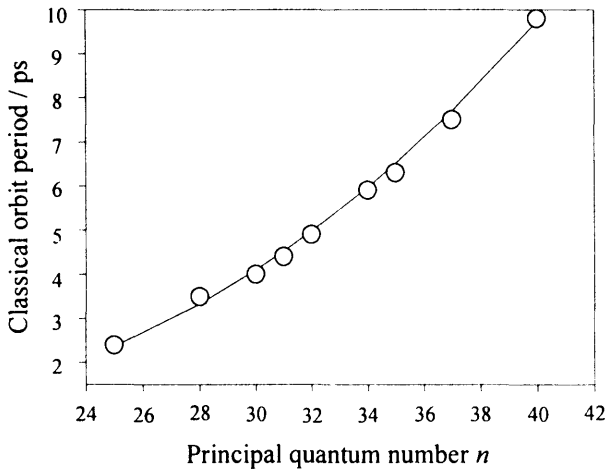

Figure 5.9 Plot showing the trend in classical orbit period as the average energy (in terms of principal quantum number) increases. The circles represent experimentally determined orbit periods and the solid line represents the calculated trend.

5.7.3 WAVE PACKETS SEPARATED BY T_{cl}

As mentioned above, the quantum defect difference between the *d* and s Rydberg series in Na $\Delta\mu = 0.35$. Therefore, applying equation (5.16), after one classical period of motion, the two angular momentum components of the wave packet will have a phase difference 0.7π. A second wave packet launched at this time can be tuned so that it is exactly out of phase with one angular momentum component of the wave packet but not with the other. Removing one of the angular momentum components from the wave packet has the effect of filtering out the oscillation in the angular coordinate to leave only the radial motion.

The results of such an experiment are presented as state-selective field-ionisation (SSFI) plots in figure 5.10. The spectra in figure 5.10(a) are the SSFI profiles of the individual components of a wave packet with average principal quantum number n =

35. The solid lines are SSFI traces of the $34d$ – $38d$ states and the dashed lines are SSFI traces of the $35s$ – $39s$ states. The traces have different profiles and depend on the mechanism of field-ionisation, as the evolution of a Rydberg state from zero-field to high-field depends on the slew rate of the electric field and the gradients of the potential energy curves [32]. From these traces it is apparent that with our experimental parameters it is easiest to distinguish between the $34d$ and $35s$ Rydberg states.

Figure 5.10(b) represents a set of experimentally measured SSFI traces as a function of the phase difference between two optical pulses, separated by one classical orbit period (6.5 ps). The horizontal axis is the time-of-flight, the vertical axis is the phase difference between the two pulses, and the colour is a measure of the electron intensity. Blue is the least intense and red, the most intense. In a typical measurement, the electron signal is summed for 1000 laser shots, and the phase is changed in steps of $\lambda/14$.

As the optical phase difference is scanned, Ramsey fringes are observed in each of the constituent Rydberg states. The fringe frequency is dependent on the energy separation between each Rydberg state in the superposition and the 'launch' state, and therefore the fringes in the populations of the individual quantum states are out of phase with one another. The most significant observation is made in the region of the $35s$ and $34d$ quantum states, which are quite clearly phase-shifted with respect to one another. The maximum intensity of the $34d$ state is observed around $\phi = 0$. When $\phi = 0.7\pi$ the $35s$ state is a maximum.

Figure 5.10(c) is a calculated density plot. The function $a_n^2(t_{cl} + t_\phi)$ is determined from equation (5.11) with ϕ ranging from 0 to 2π, for each individual Rydberg state, and then convoluted with the measured profiles in figure 5.10(a). To date, this is the first direct experimental observation of the angular momentum composition of a radial electron wave packet composed of more than one angular momentum component.

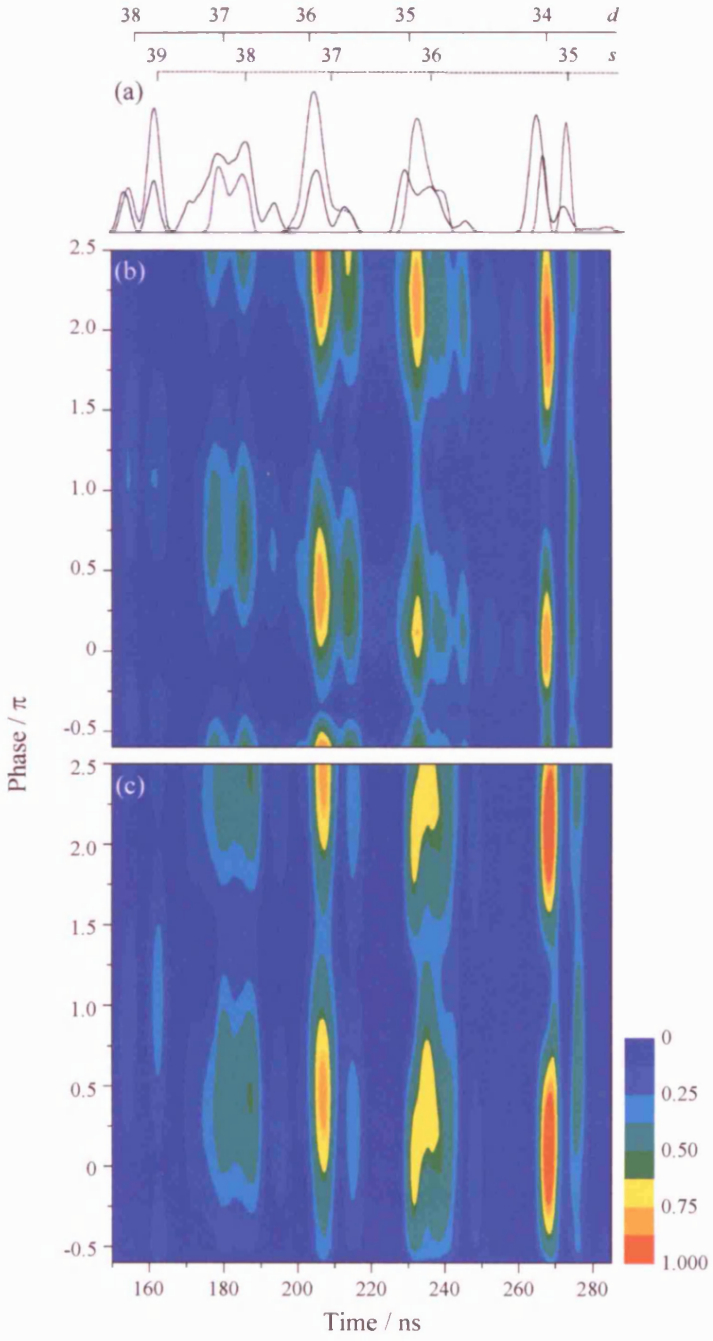

Figure 5.10 Calculated (b) and experimental (c) SSFI traces illustrating the phase evolution of individual *s* and *d* Rydberg states in a wave packet excited around $n = 35$ by a 0.7 ps bandwidth limited laser pulse. The excitation was made with a pair of phase-locked pulses separated by $t = T_{cl} + t_{\phi}$. The individual Rydberg states which make up the wave packet are shown in (a).

Figure 5.11 is an enlarged region of the SSFI spectrum, highlighting the separation of the *s* and *d* component of the wave packet. Along the left hand side of figure 5.11, the populations of the *s* and *d* states are plotted as a function of the phase-shift of the second wave packet. When $\phi = 0$, the 34*d* state is at a maximum and the 35*s* state is, according to the colour key, less than one fifth of the *d* intensity. In contrast, the 35*s* state has a maximum value at $\phi = 0.7\pi$ and the corresponding 34*s* state is about one third of the intensity. In the following section these observations will be fully quantified.

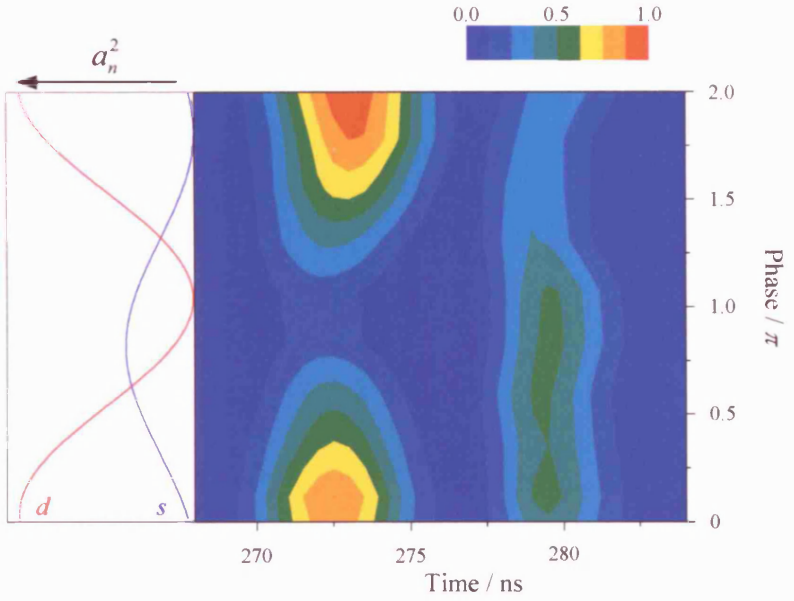

Figure 5.11 SSFI data representing the population distributions of the 34*d* and 35*s* Rydberg states in a Na wave packet after excitation with a pair of phase-locked pulses separated by $t = T_{cl} + t_\phi$. As ϕ is varied from 0 to 2π, the population of each angular momentum component oscillates depending on the degree of interference within the wave packets. A calculated plot showing the population vs. phase evolution is plotted on the left hand side of the SSFI data to provide a linear representation of the variation in population.

The important quantum state compositions are highlighted in figure 5.12. Rydberg state populations, $a_n^2(T_{cl} + \phi/\omega)$, are calculated using equation (5.9) for $\phi =$ (a) 0, (b) π, (c) 0.7π, and (d) -0.3π.

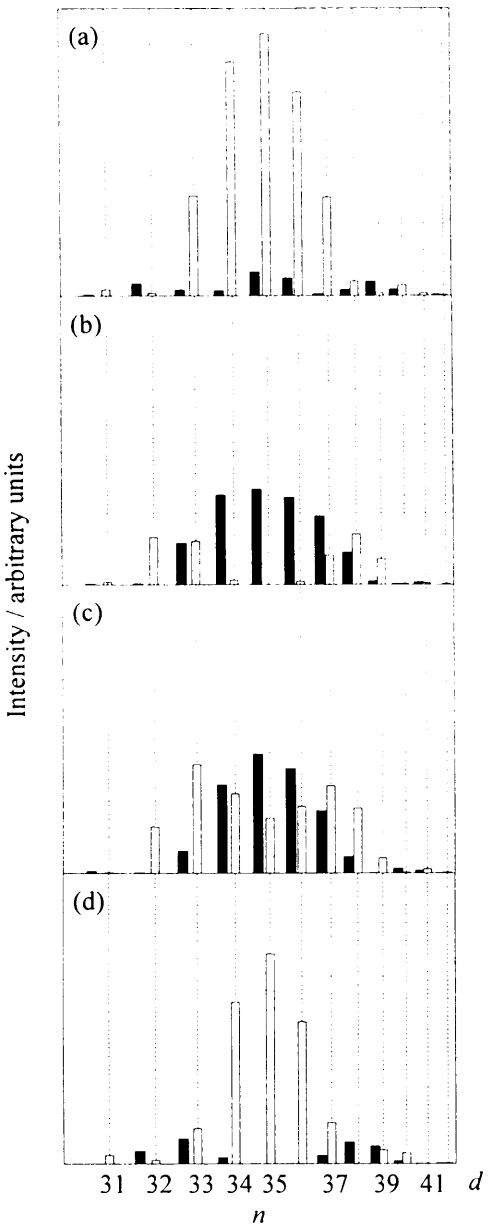

Figure 5.12 Calculated population distributions for the *s* and *d* states in a wave packet in Na, created around $n = 35$ with a pair of 0.7 ps, phase-locked laser pulses. Plots (a) – (d) differ in the amount of time the pulses are separated. In all cases, the second laser pulse is delayed by a time $t = T_{cl} + t_\phi$, where ϕ = (a) 0, (b) π, (c) 0.7π, and (d) -0.3π. When $\phi = 0$, the second wave packet is completely in phase with the *d* component of the first wave packet, resulting in an enhancement of the *d* population. Conversely, when $\phi = \pi$, the *d* component is depopulated. The same situation arises with the *s* states when $\phi = 0.7\pi$ and -0.3π, due to the shift in the energy levels by the quantum defect, $\delta = 0.35$ (in mod 1).

When ϕ = 0, the second wave packet will be in phase with the d component of the evolved wave packet, increasing the intensity of the central d component to its maximum values of $\Omega_d^2 g_d^2$. The s components interfere destructively reducing the intensity of the central s component to

$$\tfrac{1}{4}\Omega_s^2 g_s^2 \left(1+e^{0.7\pi}\right)\left(1+e^{-0.7\pi}\right) \approx 0.2\times\Omega_s^2 g_s^2 \approx 0.1\times\Omega_d^2 g_d^2 . \tag{5.16}$$

With a delay $t = T_{cl} + \pi/\omega$, the second wave packet will be completely out of phase with the central d component of the evolved wave packet, reducing the intensity of the central d state to essentially zero. However, the intensity of the central s component is enhanced to

$$\tfrac{1}{4}\Omega_s^2 g_s^2 \left(1+e^{0.3\pi}\right)\left(1+e^{-0.3\pi}\right) \approx 0.8\times\Omega_s^2 g_s^2 . \tag{5.17}$$

The control scheme is less effective at the wings of the Gaussian distribution due to the anharmonicity of the Rydberg energy levels; however, the total d/s ratio is reduced from 10.6 to 0.5 between figures 5.12(a) and 5.12(b). Similar arguments can be applied for the cases of maximum and minimum s intensity in which the total d/s ratios are 1.3 and 6.6 and illustrated in figures 5.12(c) and 5.12(d) respectively.

5.7.4 WAVE PACKETS SEPARATED BY $3T_{cl}/2$

Separating the angular momentum components in Na is not limited to wave packets separated by one classical orbit period. Using knowledge of the phase evolution of the wave packet, it is possible to engineer a number of situations where interference is

induced between the wave packets, allowing for manipulation of the angular momentum composition.

Consider the case where one wave packet is excited in Na, and allowed to evolve to $3T_{cl}/2$. Applying equation (5.16) where $k = 1.5$ and approximating $\Delta\mu = 1/3$, results in a phase separation between the *s* and *d* components in this wave packet of $\Delta\phi = \pi$. If this wave packet is allowed to evolve for $3T_{cl}/2$ before a second wave packet is excited, the following situation occurs: the first wave packet is at the outer turning point of the orbit, and, having evolved for $3T_{cl}/2$, possesses a phase separation between its *s* and *d* states equal to π. At this point, the second wave packet is created at the core, with its constituent *s* and *d* states in phase with one another. At this time, using knowledge of phase evolution in wave packets, it is possible to selectively enhance or deplete the *s* or *d* components.

Referring back to chapter 2, there are specific intervals throughout the evolution of a wave packet where its constituent states come into phase with one another – the partial revivals. At the second order partial revival, alternate state in the wave packet are $\pi/2$ out of phase with one another [47], therefore, in the situation described above, at the second order partial revival the first wave packet will split into two parts, each separated by $T_{cl}/2$ and having a phase difference equal to $\pi/2$. However, since the *d* component of this wave packet was π out of phase with the *s* component initially, the added phase shift that incurs at the second order partial revival means that now *both* wave packets have *d* components that are π out of phase with the *s* components, whilst still phase shifted by $\pi/2$ from each other. The same situation arises with the second wave packet. However, there is no phase difference initially between the *s* and *d* states in this wave packet. Therefore, when the wave packet is split into two smaller wave packets at the second order partial revival, they will be $\pi/2$ out of phase with each other, but there will be no phase separation between the *s* and *d* components. The above scheme is illustrated in a cartoon plot in figure 5.13.

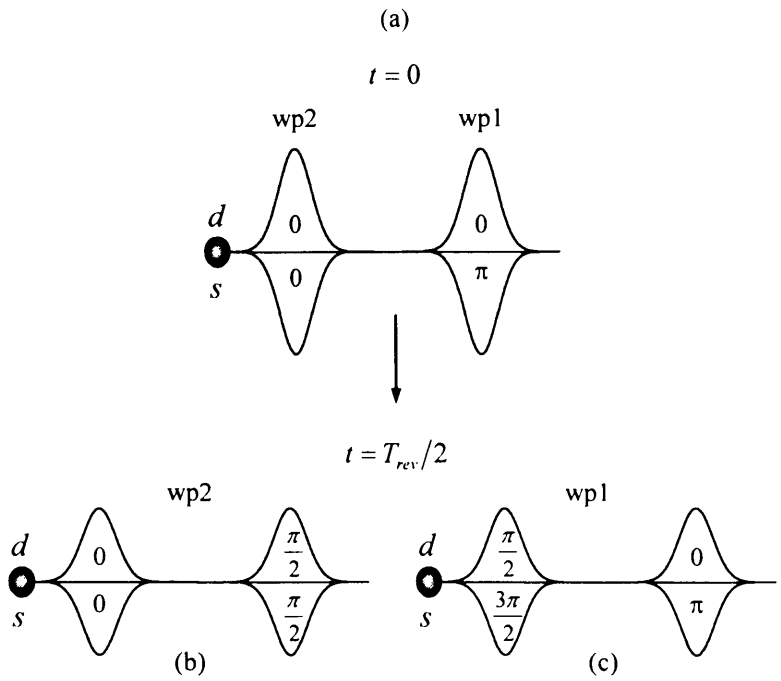

Figure 5.13 Cartoon plot illustrating the phase differences that arise at the second order partial revival, when two wave packets in Na are excited with a pair of phase-locked pulses separated by $3T_{cl}/2$. The quantum defect difference is $\Delta\mu \approx 1/3$, resulting in a phase difference of π between the s and d states in the first wave packet (wp1). At the second order partial revival, both wave packets have split into two, each $\pi/2$ out of phase with the other. In this state, not one of the s or d components of the four resulting wave packets is in phase.

The situation described above provides a good starting point for a coherent control scheme. The s and d components are out of phase in one wave packet and in phase in the other, therefore, phase-shifting the second wave packet by a predetermined amount can result in constructive or destructive interference between a particular angular momentum component in the first wave packet.

Two schemes which successfully depopulate specific angular momentum components arise when the second wave packet is excited at a time $t = 3T_{cl}/2 + t_{\phi}$, where $\phi = \pm\pi/2$. This situation is presented as a cartoon plot in figure 5.14. The left hand side of figure 5.14 illustrates the case where the second wave packet is excited at $t = 3T_{cl}/2 + t_{\phi=-\pi/2}$.

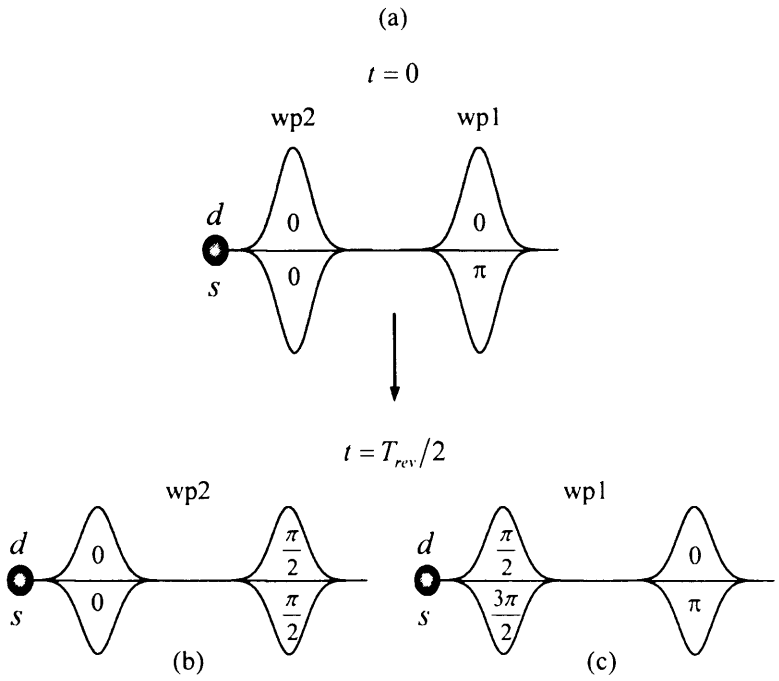

Figure 5.13 Cartoon plot illustrating the phase differences that arise at the second order partial revival, when two wave packets in Na are excited with a pair of phase-locked pulses separated by $3T_{cl}/2$. The quantum defect difference is $\Delta\mu \approx 1/3$, resulting in a phase difference of π between the s and d states in the first wave packet (wp1). At the second order partial revival, both wave packets have split into two, each $\pi/2$ out of phase with the other. In this state, not one of the s or d components of the four resulting wave packets is in phase.

The situation described above provides a good starting point for a coherent control scheme. The s and d components are out of phase in one wave packet and in phase in the other, therefore, phase-shifting the second wave packet by a predetermined amount can result in constructive or destructive interference between a particular angular momentum component in the first wave packet.

Two schemes which successfully depopulate specific angular momentum components arise when the second wave packet is excited at a time $t = 3T_{cl}/2 + t_{\phi}$, where $\phi = \pm\pi/2$. This situation is presented as a cartoon plot in figure 5.14. The left hand side of figure 5.14 illustrates the case where the second wave packet is excited at $t = 3T_{cl}/2 + t_{\phi=-\pi/2}$.

possesses only *d* angular momentum in the core region and only *s* angular momentum at the outer turning point. The right had side of figure 5.12 outlines the case where the second wave packet is excited at $t = 3T_{cl}/2 + t_{\phi=+\pi/2}$. The situation is analogous to the one described above, except that the final wave packet, "wave packet (b)" consists of *s* character at the core, and the *d* character at the outer turning point.

Experimental wave packet recurrence spectra following excitation with a pair of phase-locked pulses separated by $t = 3T_{cl}/2 + t_{\phi}$, where $\phi = \pm\pi/2$ are presented in figure 5.15(a). The wave packets were excited with a 0.7 ps pulse corresponding to a bandwidth of 21 cm^{-1}, with an average energy corresponding to $n = 35$. The wave packet spectra were recorded over the region of the second order partial revival at around 38 ps, and the evolution was monitored with a third phase-locked pulse using the optical Ramsey method. Calculated wave packet spectra are presented in plot (b). In (b), the solid line represents the calculated recurrence spectrum, whilst the dotted and dashed lines represent calculated spectrum of a wave packet excited using a single optical pulse. The vertical lines in plots (a) and (b) represent the classical orbit period of the wave packet. The corresponding population distributions, calculated with equation (5.9), are presented in plot (c).

Referring back to the cartoon plots, the upper plots in figure 5.15(a) and (b), represent "final wave packet (a)" with the d component localised in the core region and the *s* component localised at the outer turning point. The lower plots represent the opposite case of "final wave packet (b)", where the opposite situation arises. It is also interesting to note that by removing the angular momentum components at either end of the orbit at the second order partial revival, a full revival has effectively been created. The wave packet is now oscillating at the classical frequency, even though it is in the region of the second order partial revival. In terms of the frequency distribution of Rydberg states, if a pulse pair is separated in time by $t = 3T_{cl}/2 + t_{\phi}$, where $\phi = \pm\pi/2$, a Fourier transform of the pulses results in a frequency comb that coincides the excitation frequencies of alternate *s* states and alternate *d* states in the superposition. This is evident in figure 5.15(c). However, the excitation frequencies of the states under this

frequency comb do not coincide with the dips and troughs in the comb, therefore, the populations of these states do not reach their maximum or minimum value. For reference, the maximum and minimum population values for the central d state are reached when $\phi = 0$ and π respectively. However, separation of the angular momentum components using these phases is not possible, as there is no localisation of just d or just s states – they are mixed over the whole of the orbit.

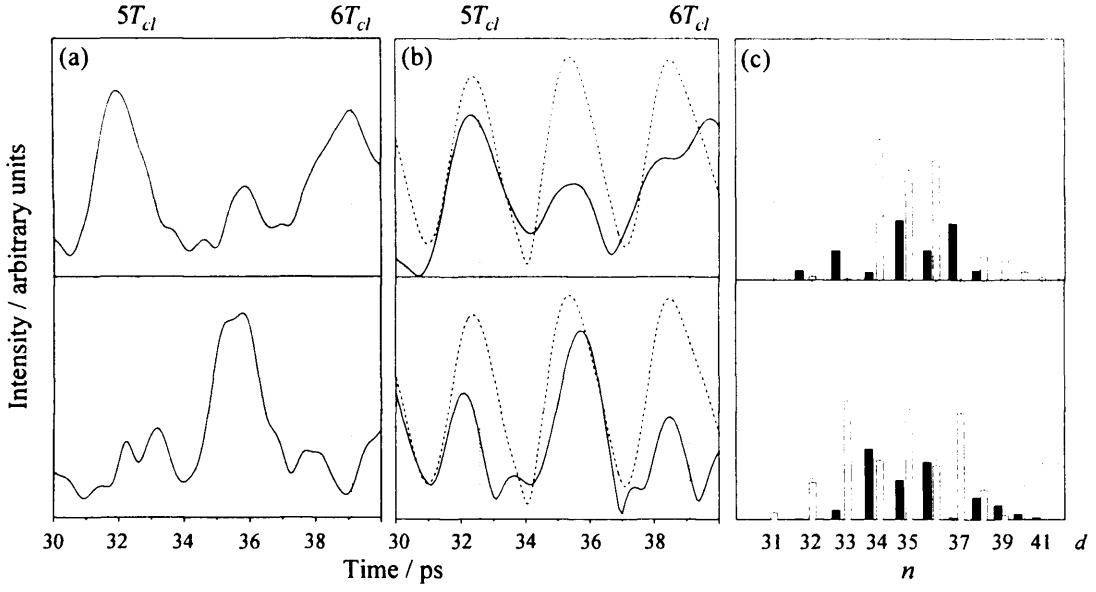

Figure 5.15 Experimental (a) and calculated (b) recurrence spectra for a wave packet excited around n = 35 in Na with a pair of 0.7 ps phase-locked laser pulses, separated by $t = 3T_{cl}/2 + t_{\phi}$. The upper plots represent the case where $\phi = \pi/2$, and the lower plots, $\phi = -\pi/2$. In (b), the solid line represents the calculated recurrence spectrum, whilst the dotted and dashed lines represent calculated spectrum of a wave packet excited using a single optical pulse to emphasise the second order partial revival. The vertical lines in plots (a) and (b) illustrate the classical orbit period. The population distributions of the s and d states in each wave packet are present in (c).

5.8 CONCLUSION

In summary, control of the angular momentum components of radial Rydberg wave packets in Na has been investigated experimentally and modelled using intuitive control schemes. The control schemes are based on the interference effects that occur when a pair of wave packets are excited, separated by a specifically engineered time delay. This delay is predetermined and takes into account the quantum defect between the s and d series in Na, and the inherent phase evolution of states within a wave packet.

The first case involved control of the s/d angular momentum ratio, in wave packets that had evolved for one orbit period. Using SSFI, separation of the angular momentum of one set of states in the superposition was clearly demonstrated, as was the phase evolution of angular momentum states in a wave packet. To date, this is the first experimentally resolved case of angular momentum evolution, and the separation of angular momentum states, in an atomic or molecular system.

The second case involved the localisation of s or d character at opposite ends of its classical orbit, which was monitored in the time domain using the optical Ramsey method. Using a pair of phase-locked pulses with a specially engineered time delay, interference effects between the two wave packets lead to the dephasing of one angular momentum component at one end of the orbit, and the other component at the opposite end of the orbit, leaving s and d character in separated locations in space.

The work in this chapter shows that knowledge of the phase evolution of wave packet states is an effective tool in the application of coherent control schemes. The schemes presented here are simple, logical and applicable to any system where the energy levels and excitation parameters are known.

5.9 REFERENCES

1. G. Alber and P. Zoller, *Phys. Reps.* **199** (5), 231 (1991).
2. G. Alber, H. Ritsch, and P. Zoller, *Phys. Rev. A* **34** (2), 34 (1986).
3. R. R. Jones and L. D. Noordam, *Adv. At. Mol. Opt. Phys.* **38**, 1 (1998).
4. L. D. Noordam, D. I. Duncan, and T. F. Gallagher, *Phys. Rev. A* **45** (7), 4734 (1992).
5. J. R. R. Verlet and H. H. Fielding, *Int. Rev. Phys. Chem.* **20** (3), 283 (2001).
6. T. C. Weinacht and P. H. Bucksbaum, *J. Opt. B-Quantum Semicl. Opt.* **4** (3), R35 (2002).
7. H. H. Fielding, *Ann. Rev. Phys. Chem.* **56**, 91 (2004).
8. L. E. E. de Araujo and I. A. Walmsley, *J. Opt. B-Quantum Semicl. Opt.* **5** (1), R27 (2003).
9. M. W. Noel and C. R. Stroud, *Phys. Rev. Lett.* **75** (7), 1252 (1995).
10. M. W. Noel and C. R. Stroud, *Phys. Rev. Lett.* **77** (10), 1913 (1996).
11. R. van Leeuwen, M. L. Bajema, and R. R. Jones, *Phys. Rev. Lett.* **82** (14), 2852 (1999).
12. R. van Leeuwen, K. Vijayalakshmi, and R. R. Jones, *Phys. Rev. A* **63** (3), 033403 (2001).
13. J. R. R. Verlet, V. G. Stavros, R. S. Minns, and H. H. Fielding, *Phys. Rev. Lett.* **89** (26), 263004 (2002).
14. J. R. R. Verlet, V. G. Stavros, R. S. Minns, and H. H. Fielding, *J. Phys. B-At. Mol. Opt. Phys.* **36** (17), 3683 (2003).
15. H. Wen, C. Rangan, and P. H. Bucksbaum, *Phys. Rev. A* **68** (5), 053405 (2003).
16. J. Ahn, T. C. Weinacht, and P. H. Bucksbaum, *Science* **287** (5452), 463 (2000).
17. J. Ahn, D. N. Hutchinson, C. Rangan, and P. H. Bucksbaum, *Phys. Rev. Lett.* **86** (7), 1179 (2001).
18. J. Ahn, C. Rangan, D. N. Hutchinson, and P. H. Bucksbaum, *Phys. Rev. A* **66** (2), 022312 (2002).

19. C. Rangan and P. H. Bucksbaum, *Phys. Rev. A* **6403** (3), 033417 (2001).
20. C. Rangan, J. Ahn, D. N. Hutchinson, and P. H. Bucksbaum, *J. Mod. Opt.* **49** (14-15), 2339 (2002).
21. T. C. Weinacht, J. Ahn, and P. H. Bucksbaum, *Science* **287**, 463 (2000).
22. R. S. Minns, J. R. R. Verlet, L. J. Watkins, and H. H. Fielding, *J. Chem. Phys.* **119** (12), 5842 (2003).
23. R. S. Minns, R. Patel, J. R. R. Verlet, and H. H. Fielding, *Phys. Rev. Lett.* **91** (24), 243601 (2003).
24. M. Renard, E. Hertz, B. Lavorel, and O. Faucher, *Phys. Rev. A.* **69** (4), 043401 (2004).
25. M. Spanner, E. A. Shapiro, and M. Ivanov, *Phys. Rev. Lett.* **92** (9), 093001 (2004).
26. J. B. Ballard, H. U. Stauffer, E. Mirowski, and S. R. Leone, *Phys. Rev. A* **66** (4), 043402 (2002).
27. M. Comstock, V. V. Lozovoy, and M. Dantus, *Chem. Phys. Lett.* **372**, 739 (2003).
28. M. Dantus and V. V. Lozovoy, *Chem. Rev.* **104** (4), 1813 (2004).
29. T. Brixner and G. Gerber, *ChemPhysChem* **4** (5), 418 (2003).
30. J. L. Herek, W. Wohlleben, R. J. Cogdell, D. Zeidler, and M. Motzkus, *Nature* **417** (6888), 533 (2002).
31. R. L. Liboff, *Introductory Quantum Mechanics*, 3rd ed. 1988.
32. T. F. Gallagher, *Rydberg Atoms*. Cambridge University Press, 1994.
33. J. Parker and C. R. Stroud, *Phys. Rev. Lett.* **56** (7), 716 (1986).
34. J. A. Yeazell, M. Mallalieu, and C. R. Stroud, *Phys. Rev. Lett.* **64** (17), 2007 (1990).
35. J. Parker and C. R. Stroud, *Physica Scripta* **T12**, 70 (1986).
36. G. Alber, H. Ritsch, and P. Zoller, *Phys. Rev. A* **34** (2), 1058 (1986).
37. L. D. Noordam, A. ten Wolde, A. Lagendijk, and H. B. van Linden van den Heuvell, *Phys. Rev. A* **40** (12), 6999 (1989).

38. A. ten Wolde, L. D. Noordam, A. Lagendijk, and H. B. van Linden van den Heuvell, *Phys. Rev. Lett.* **61** (18), 2099 (1988).

39. M. J. Seaton, *Rep. Prog. Phys.* **46**, 167 (1983).

40. M. J. Seaton, *Proc. Phys. Soc.* **88**, 801 (1966).

41. U. Fano, *Phys. Rev. A* **2**, 353 (1970).

42. B. N. Taylor and E. R. Cohen, *J. Res. NIST* **95**, 497 (1990).

43. M. Ciocca, C. E. Burkhardt, and J. J. Leventhal, *Phys. Rev. A* **45** (7), 4720 (1992).

44. J. M. Hollas, *Modern Spectroscopy*. John Wiley & Sons, 1997.

45. W. Demtroder, *Laser Spectroscopy*, 2nd ed. Springer-Verlag, Berlin, 1996.

46. J. R. R. Verlet, PhD Thesis, King's College London, 2003.

47. I. S. Averbukh and N. F. Perelman, *Phys. Lett. A* **139** (9), 449 (1989).

CHAPTER 6:

CONCLUSION AND OUTLOOK

The work presented in this thesis extends existing coherent control methodologies by focusing on simple atomic and molecular systems. The return to less complex systems was brought about in response to the increasing use of optimisation techniques to achieve the ultimate pulse shape / spectral phase for the required task. The resulting pulse is often so complex that it is exceedingly difficult to appreciate the physical mechanism behind the control. In this thesis, the aim was to gain an understanding of the physics of the system, and then use this knowledge in the design of logical control schemes. This was achieved by establishing a link between the wave packet phase, and the spectral phase of the laser pulse. The following chapter summarises the significant aspects of the thesis, and outlines any future directions the work is taking.

6.1 VIBRATIONAL WAVE PACKETS IN Na_2^+

In chapter 4, a logical coherent control scheme employing a train of phase-locked optical pulses to generate customised vibrational wave packets was described. Through the definition of the relationship between the phases of the vibrational eigenstates and the optical phase of the laser pulse, control over the time-dependent populations of the individual components of the wave packet was attained.

The impetus for modeling vibrational wave packets in the Na_2^+ system was to provide the theoretical basis for proposed wave packet control experiments on the Na_2^+ potential curve. Unfortunately, experimental verification of the theory has still not been achieved. As mentioned in chapter 3, preliminary frequency spectra have been obtained of, what we believe to be the $A(v'=9) \leftarrow X(v''=0)$ transition in Na_2. This is illustrated in figure 6.1.

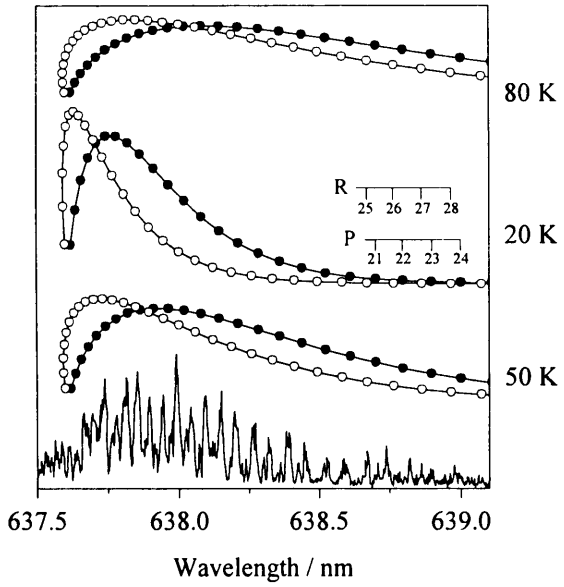

Figure 6.1 Experimental spectrum of the $A^1\Sigma_u^+ \leftarrow X^1\Sigma_g^+$ transition in Na2 recorded by 1+2 resonance-enhanced multiphoton ionisation (REMPI) using a Nd:YAG pumped dye laser operating at 10 Hz (CLF laser loan pool). Included in the figure are calculated line positions (open circles are R-branch lines and closed circles are P-branch lines). The intensity profile is calculated assuming molecular beam temperatures of 20 K, 50 K and 80 K. The spectrum is most closely simulated assuming a molecular beam temperature of around 50 K.

There is however a discrepancy of approximately 15 cm^{-1} in the line positions when compared to known literature values of experimental and theoretical line positions, and also our own calculations. As yet we have been unable to find an explanation for the discrepancy, as all the equipment was functioning within normal limits.

With regards to the Na_2 molecular beam, the major problem was lack of dimers in the interaction region. There were limits on the temperature the oven could be heated to before the diffusion pump stalled. In order to achieve higher temperatures, the sodium oven and chamber are in the process of being modified. The first modification is complete and involved the replacement of the middle flange (separating the diffusion and turbo sides of the chamber) with a "top-hat" flange, thereby shortening the distance between the oven and the interaction region resulting in a greater flux of Na_2 through the interaction region. The new arrangement is illustrated below:

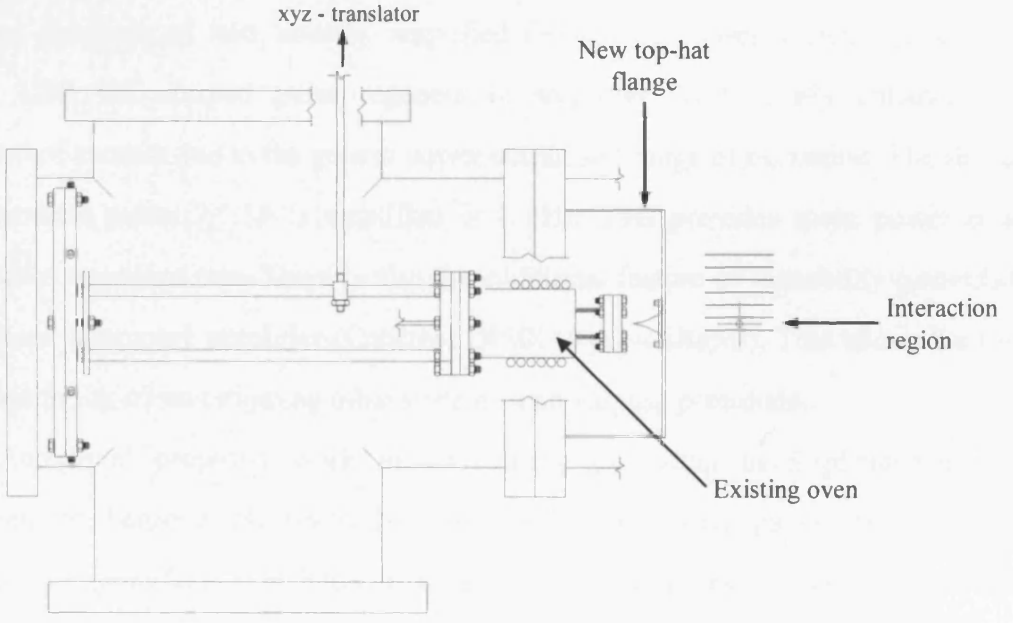

Figure 6.2 New arrangement of the oven in the vacuum chamber. A top-hat flange was made to replace the central flange of the chamber. The reasoning was that if the oven was in closer proximity to the interaction region, a greater throughput of sodium and higher signal intensity could be achieved.

The top-hat flange resulted in greater signal intensity in the Na beam but with the adverse effect of increasing the pressure in the source side of the chamber resulting in an increased pumping speed. There was no obvious effect on the intensity of the Na_2 beam. To counteract this increased pressure in the source side of the chamber, ongoing modifications are being made to the chamber and oven. The middle flange has been hollowed out to enable liquid nitrogen to be poured in to provide a cold wall to trap sodium from the oven. A cooling jacket for the oven is in the process of being manufactured, to minimise heat loss from the oven and to isolate the liquid nitrogen filled cold wall from the heat of the oven. Both of these improvements will enable higher temperatures to be reached in the oven (up to 800°C) without putting too much pressure on the pumps.

It is believed that these experiments, and maybe future experiments, will be successful if there is sufficient dimer density in the interaction region. In addition, the imminent purchase of two tunable, amplified femtosecond laser systems (Coherent Legend USP HE chirped pulse regenerative amplifier) will greatly enhance the likelihood of success due to the greater power output and range of excitation. The above lasers produce pulses of 30 fs amplified at 1 kHz. This provides more power at a manageable repetition rate. There is also the additional feature of tuneability (provided by a optical parametric amplifier (Coherent OPERA) pulse shaper). This allows for the added possibility of investigating other systems with varying potentials.

Additional proposed work includes using the setup in a photochemistry experiment on benzene. By controlling the shape of the wave packet on an exited potential energy surface, it is hoped that the ground state products can be probed by detecting the angular distributions of ejected photoelectrons through incorporation of an electron/ion imaging apparatus.

6.2 ELECTRONIC WAVE PACKETS IN Na

The work presented chapter 5 was an experimental and theoretical analysis of quantum interference between Rydberg wave packets in Na, achieved using pairs of phase-locked wave packets. Successful manipulation of the total orbital angular momentum in Na Rydberg atoms was achieved through exploitation of the difference between the quantum defects of the two series. The control took two forms: separation of the *s* and *d* angular momentum components in the resultant wave packet, and localisation of the angular momentum components on opposition ends of the electronic orbit. Both control schemes were theoretically predicted and experimentally verified. In addition, this work provides the first direct experimental observation of the angular momentum composition of a radial electron wave packet composed of more than one angular momentum component.

An ongoing modification to this control scheme involves the introduction of chirp to the laser pulse, to account for the significant anharmonicity of the Rydberg states. A chirped pulse describes a pulse whose frequency changes with time; if the frequency increases with time, this is known as positive chirp and decreasing with time is negative chirp. Referring back to the population plots in, for example, figure 5.12 it is apparent that the control is excellent for the central state in the wave packet, whilst the populations at the outer edges of the plot are not controlled as effectively. Note: the weaker anharmonicity of vibrational energy levels ensures that this problem does not arise in the control scheme involving vibrational wave packets. A chirped pulse would be able to counteract the effect of the first order dispersion of the Rydberg states, and generate an interference pattern in the spectral intensity profile with minima that coincide with either the *s* or the *d* components of the whole wave packet, not just the centre of the wave packet. This is ongoing work, which will be incorporated into the existing control scheme when perfected.

Further work is being carried out in molecular Rydberg series, specifically in nitric oxide (NO), using the SSFI setup. Molecular Rydberg series are far more complex

than atomic series, as in Na, so the separation of angular momentum using pulse sequences to be detected by SSFI is a definite goal. It is hoped that SSFI could become a spectroscopic tool to explore Rydberg series in other Rydberg molecules such as molecular hydrogen and boron hydride (BH).

APPENDIX 1

(a) Fortran 90 code for calculation of vibrational and rotational energy levels, transition energies and rotational energy distributions in Na_2 (chapter 4)

```
!*************************************************************************
!                          *PROGRAM dimer energies*
!                          ************************
!Program to calculate rotational and vibrational absolute energies and
!transitions from Dunham coefficients.
!You can also calculate the distribution of rotational energy levels !at
!different rotational temperatures.
!If you need to run the 'transition_energies' and 'rotational_intensity'
!subroutines, use !format statements 2+4.
!You'll need to comment out format statements 22, 23 and 24 (X state !loop)
!and 42, 43 and 44 (A state loop).
!*************************************************************************
program dimer_energies
implicit double precision (a-h, o-z)
integer::v,vx,va
real,dimension(0:6,0:4):: x_mat, a_mat
real,dimension(0:500):: energyx, energya, branch
real,parameter:: h=6.626E-34, c=2.998E10, boltz=1.380E-23
real:: b_lower, intensity, te
!DUNHAM COEFFICIENTS ARE READ IN MATRIX FORM
open(1,file='dimer_data.dat')
read(1,*)((x_mat(i,k),k=0,4,1),i=0,6,1)
read(1,*)((a_mat(i,k),k=0,4,1),i=0,6,1)
read(1,*)te
!VIBRATIONAL LEVEL OF X STATE
read(1,*)vx
!VIBRATIONAL LEVEL OF A STATE
read(1,*)va
!CALCULATE ENERGIES OF v''
v=0
!CALCULATE ROTATIONAL CONSTANT OF v'' (B'')
b_lower=x_mat(0,1)-x_mat(1,1)*(vx+0.5)+x_mat(2,1)*(vx+0.5)**2&
&+x_mat(3,1)*(vx+0.5)**3+x_mat(4,1)*(vx+0.5)**4
open(2,file='x_state.dat') !OUTPUT FILE
write(2,22)'X state ro-vibrational energies'
22 format (A31)
do v=0,20,1
!write (2,23)'v','j','E/cm-1'
!23 format (/,1x,a2,2x,a2,6x,a6,/)
      do j=0,50 !NO. OF ROTATIONAL STATES
      sum=0.0
            do i=0,6,1
                  do k=0,4,1
                  sum = sum+x_mat(i,k)*((vx+0.5)**i)&
                  &*(j*(j+1.0)-1.0)**k
                  end do
            end do
            write (2,24) v, j, sum
            24 format (1x, i2, 2x, i2, (f14.4))
            !write (2,2) sum
            !2 format (f10.4)
      end do
end do
!calculation of vib-rot levels of v'
open (2, file='a_state.dat')
write (2,42) 'A state ro-vibrational energies'
42 format (A31)
do va=0,60,1
write (2,43) 'v', 'j', 'E/cm-1'
43 format (/,1x, a2, 2x, a2, 5x, a6,/)
```

```
      do j=0,50
      sum=0.0
            do i=0,6,1
                  do k=0,4,1
                  sum=sum+A_mat(i,k)*((va+0.5)**i)*(j*(j+1.0)-1.0)**k
                  end do
            end do
            write (2,4) sum+te
      4     format (f10.4)
            write (2,44) va, j,(sum+te)
      44    format (1x, i2, 2x, i2, 1x, (f14.4))
      end do
end do
close (2)
!SUBROUTINES
call transition_energies
call rotational_intensity (b_lower)
end program dimer_energies
!*****************************************
!subroutine to calculate transition energies
!*****************************************
!If you run this subroutine you have to make sure the format
!statements are commented out when the files are opened above.
!You also have to make sure that energyx and energya contain
!the vibrational levels only
!i.e. comment out j part of do loop
subroutine transition_energies
implicit double precision (a-h, o-z)
real,dimension(0:20):: energyx, energya
integer:: vx, va
open (1, file='x_state.dat')
read (1,*) (energyx(vx), vx=0,20)
open (1, file='a_state.dat')
read (1,*)(energya(va), va=0,20)
open (2, file='transition_energies.dat')
do vx=0,20,1
      write (2,98) 'X (v=' , vx, ')', 'to A (v)'
      98 format (/,a5,i2,a1,1x,a8,/)
      do va=0,20,1
            sum=energya(va)-energyx(vx)
            write (2,99) va, sum, (1/sum)*1e7
            99 format (21(i2, 1x, 2(f10.4)))
      end do
end do
end subroutine transition_energies
!*****************************************************
!calculation of rotational state intensity distribution
!*****************************************************
!if you want to run this subroutine you have to make sure
!the j's are in the original calculation
subroutine rotational_intensity (b_lower)
implicit double precision (a-h, o-z)
real, dimension (0:500) :: energyx, energya, branch
real, parameter:: h=6.626E-34, c=2.998E10, boltz=1.380E-23
real:: b_lower, intensity
open (1, file='x_state.dat')
read (1,*) (energyx(i), i=0,100)
open (1, file='a_state.dat')
read (1,*)(energya(i), i=0,100)
open (1, file='temp.dat')
read (1,*), t
!EXPONENTIAL PART OF THE INTENSITY EQUATION
exp_bit=(h*c)/(boltz*t)
!THIS BIT CALCULATES THE P AND R BRANCHES
do m=-1,1
      do i=0,100    !NO. OF J LEVELS YOU WANT
      j=i+m
```

```
      !START IF LOOP
      if ((j<0).OR.(j>100)) goto 5
      branch(i)=energya(j)-energyx(i)
      intensity=branch(i)*(b_lower/t)*(j+i+1.0)&
      &*exp(-b_lower*i*(i+1)*exp_bit)
      if (m==-1) then
      open (2, file='p_branch.dat')
      !OUTPUT J, INTENSITY AND ENERGY
      write (2, 6) i, branch(i), (1/branch(i))*1e7, intensity
      6 format (i4, 3x, 3(f14.8,3x))
      else if (m==1) then
      open (2, file='r_branch.dat')
      write (2,7) i, branch(i), (1/branch(i))*1e7, intensity
      7 format (i4, 3x, 3(f14.8,3x))
      end if
      5 end do
end do
end subroutine rotational_intensity
```

(b) Fortran 77 code for calculation of the autocorrelation function for vibrational wave packets, the population distribution of vibrational states within the wave packet and the radial distribution function. Additional subroutines calculate the populations as a function of time, and the phase-shift required to depopulate the central state in a vibrational wave packet (chapter 4).

```
!-----------------------------------------------
!WAVE PACKET AND POPULATIONS PROGRAM FOR DIMERS
!-----------------------------------------------
program vib_population
implicit double precision (a-h, o-z)
dimension en(0:20), fc(0:20), gauss(0:20), trans_int(0:20), pop(0:20),
&delta(0:20), en1(0:20), popmat(0:20,0:43), &wf(0:20,0:336)
complex*16 a(0:20)
parameter c=2.99792458002d10, pi=3.141592654, ryd=109737.32, $wcon=8065.465,
freqcon=2.4179659d14
integer v
!READ IN INPUT FROM FILE
open(1,file='input.dat')
read(1,*) en, fc, av_en, en_int, fwhm_t, tmin, tmax, tstep, tcl, wtmin, wtmax,
wtstep, xtcl, xpi
open(2,file='wavefunctions.dat')
read(2,*)((wf(j,i),i=0,336,1),j=0,20,1)
!OUTPUT COMMENTS TO FILE
tpi=1.0d+12/(2*c*(av_en-en_int))
fwhm=(wcon/freqcon)*(0.441/(fwhm_t*1d-15))
pi_wn=(av_en-en_int)
pi_nm=(1/pi_wn)*1e7
open(4,file='comments.txt')
write(4,10) tcl,tpi,fwhm_t,fwhm,xtcl,(tcl*xtcl),pi_wn,pi_nm,xpi
10 format ('the classical vibration period = ',f10.6,' ps'
     &,//,'pi = ',e12.6,' ps'
     &,//,'for a ',f5.2,' fs pulse the fwhm = ',f11.6,' cm-1'
     &,//,'t2 = ',f5.2,' times tcl which =',f14.8,' ps'
     &,//,'this transition = ',f14.8,' cm-1 which is ',f12.8,' nm'
     &,//,'the added phase is',f5.2,' times pi')
!CALCULATE TRANSITION INTENSITIES
do v=0,20,1
      gauss(v)=sqrt(dexp((-4*(dlog(2.0d0))*(en(v)-av_en)**2)
    &  /(fwhm**2)))
      trans_int(v)=fc(v)*gauss(v)
      en1(v)=((en(v)-en_int)/(2*ryd))
end do
!CALL SUBROUTINES
call wp(en1,trans_int,tmin,tmax,tstep,tcl,xtcl,xpi,tpi)
```

```
call pops(tcl,xtcl,xpi,tpi,av_en,en_int,en1,trans_int,pi_wn,pop)
call wfs(en1,trans_int,wf,tcl,xtcl,wtmin,wtmax,wtstep,xpi,tpi)
call rdf(en1,trans_int,wf,tcl,xtcl,wtmin,wtmax,wtstep,xpi,tpi)
call pop_ps(tcl,xtcl,xpi,tpi,av_en,en_int,en1,trans_int,pi_wn, po
call population_min(pi_wn, tcl, xtcl)
end program vib_population
!************************
!SUBROUTINES START HERE
!************************
!------------
!WAVE PACKETS
!------------
subroutine wp(en1,trans_int,tmin,tmax,tstep,tcl,xtcl,xpi,tpi)
implicit double precision (a-h, o-z)
dimension en1(0:20),trans_int(0:20)
complex*16 sum1,sum2
real phase,phi,t2
integer v
parameter c=2.99792458002d10,ryd=109737.32
!OUTPUT TO FILE
open(3,file='wp_out.csv')
write (3,30)
30 format ('t,wp1,wp2,wpsum,re_wp1,re_wp2,re_wpsum')
t2=(tcl*xtcl)
phase=(tpi*xpi)
phi=t2+phase
do t=tmin,tmax,tstep
sum1=dcmplx((0.0,0.0))
sum2=dcmplx((0.0,0.0))
       do v=0,20,1
              sum1=sum1+dcmplx(trans_int(v)**2)
     & *(exp(-dcmplx((0.0,1.0))*
     & dcmplx(en1(v)*(t/2.4189d-05))))
              sum2=sum2+dcmplx(trans_int(v)**2)
     & *(exp(-dcmplx((0.0,1.0))*
     & dcmplx(en1(v)*((t+phi)/2.4189d-05))))
       end do
       wp1=(cdabs(sum1))**2
       wp2=(cdabs(sum2))**2
       wpsum=(cdabs(sum1+sum2))**2
       rabi1=dreal(sum1)
       rabi2=dreal(sum2)
       rabisum=dreal(sum1+sum2)
       write(3,32)t,wp1,wp2,wpsum,rabi1,rabi2,rabisum
32     format(f14.10,',',6(e14.8,','))
end do
end subroutine wp
!------------
!POPULTAIONS
!------------
subroutine pops(tcl,xtcl,xpi,tpi,av_en,en_int,en1,trans_int,pi_wn,pop)
implicit double precision (a-h,o-z)
dimension en1(0:20),trans_int(0:20),pop(0:20),delta(0:20)
!TO CHANGE THE INCREMENTS OF PI, CHANGE THE J VALUE OF THE MATRIX
dimension popmat(0:20,0:43)
complex*16 a(0:20)
parameter c=2.99792458002e10,ryd=109737.31,t_rev=38.7855465
integer v
real npi
!OUTPUT TO FILE AS MATRIX
open(2,file='pop_out.dat')
do v=0,21
write(2,20) v
20 format(1x,i3)
end do
do npi=-1.0,1.0,0.05
phase=tpi*npi
```

```
delay=tcl*xtcl
!TOTAL DELAY BEFORE 2ND PULSE(a.u.)
t2=(phase+delay)/2.4189d-05
write(2,21)npi
21 format(f5.2)
       do v=0,20,1
       a(v)=0.0d0
       pop(v)=0.0d0
       delta(v)=(pi_wn/(2*ryd))-en1(v)
       a(v)=dcmplx((0.0,-1.0))
     &*(1.0+(cdexp(dcmplx((0.0,-1.0))*dcmplx(delta(v)*t2))
     &*cdexp(dcmplx((0.0,1.0))
     &*dcmplx((pi_wn/(2*ryd))*t2))))*trans_int(v)
!TAKE ABSOLUTE SUM TO GET POPUALTIONS
       pop(v)=cdabs(a(v))**2
       write(2,22) pop(v)
22     format (f14.8)
       end do
end do
close(2)
open (2,file='pop_out.dat')
read (2,*)((popmat(i,j),j=0,43,1),i=0,20,1)
open(4,file='pop_mat.csv')
write(4,23)((popmat(i,j),j=0,43,1),i=0,20,1)
23 format (22(f14.8,',',1x))
end subroutine pops
!-------------------------------------------------------------
!subroutine to calculate wavepackets from the wavefunctions
!so that a 3d plot can be generated in mathematica
!-------------------------------------------------------------
subroutine wfs(en1,trans_int,wf,tcl,xtcl,wtmin,wtmax,wtstep,xpi,tpi)
implicit double precision (a-h, o-z)
dimension en1(0:20),trans_int(0:20)
dimension wf(0:20,0:336)
complex*16 sumwf
!OPEN OUTPUT FILE
open(5,file='wfs.csv')
t2=(tcl*xtcl)
phase=(tpi*xpi)
phi=t2+phase
!SUM OVER THE R COORDINATE IN 3D PLOT
step=4.0
!SUM OVER THE R COORDINATE IN WAVEFUNCTON
do i=0,336,1
       !SUM OVER TIME
       do t=wtmin,wtmax,wtstep
       sumwf=dcmplx((0.0,0.0))
              do j=0,20,1
              sumwf=sumwf+
              (dcmplx(trans_int(j))*dcmplx(wf(j,i))*dcmplx(step)
     & *(exp(-dcmplx(0.0,1.0)*dcmplx(en1(j)*(t/2.4189d-05)))
     & +exp(-dcmplx(0.0,1.0)*
     & dcmplx(en1(j)*((t+phi)/2.4189d-05)))))
              end do
              tdwf=(cdabs(sumwf))**2
              write(5,50)step,t,tdwf
50            format(2(f9.4,','),f14.8)
       end do
       step=step+0.2
end do
end
!---------------------------------------------------------------------
!subroutine to calculate the rdf at a single time (multiples of tcl)
!---------------------------------------------------------------------
subroutine rdf(en1,trans_int,wf,tcl,xtcl,wtmin,wtmax,wtstep,xpi,tpi)
implicit double precision (a-h, o-z)
dimension en1(0:20),trans_int(0:20)
```

```
dimension wf(0:20,0:336)
complex*16 sumwf
t2=(tcl*xtcl)
phase=(tpi*xpi)
phi=t2+phase
print*, 'enter t in units tcls'
read*, y
t=y*tcl
do i=0,336,1
sumwf=dcmplx((0.0,0.0))
      do j=0,20,1
            sumwf=sumwf+
            &(dcmplx(trans_int(j))*dcmplx(wf(j,i))
            &*(exp(-dcmplx(0.0,1.0)*dcmplx(en1(j)*(t/2.4189d-05)))
            &+exp(-dcmplx(0.0,1.0)*
            &dcmplx(en1(j)*((t+phi)/2.4189d-05)))))
      end do
      tdwf=(cdabs(sumwf))**2
      open(6,file='rdf.csv')
      write(6,60)i,tdwf
60    format(i3,',',f14.8)
end do
end
!---------------------------------------------------------------------
!subroutine to calulate the populations as a function of real time
!---------------------------------------------------------------------
subroutine pop_ps(tcl,xtcl,xpi,tpi,av_en,en_int,en1,trans_int,pi_wn, pop)
implicit double precision (a-h,o-z)
dimension en1(0:20),trans_int(0:20),pop(0:20),delta(0:20)
dimension pop1(0:20)
complex*16 a(0:20)
parameter c=2.99792458002e10,ryd=109737.31,t_rev=19.39277325
integer v
real npi
open(1,file='pop_realtime.csv')
do npi=-1,1,0.05
phase=tpi*npi
delay=tcl*xtcl
!TOTAL DELAY BEFORE SECOND PULSE (a.u.)
t2=(phase+delay)/2.4189d-05
t2sec=(phase+delay)
write(1,61)npi,phase,t2sec
61 format(f5.2,',',2(e14.8,','))
      do v=0,20,1
            a(v)=0.0d0
            pop1(v)=0.0d0
            delta(v)=(pi_wn-en1(v))/(2*ryd)
            a(v)=dcmplx((0.0,-1.0))
            &*(1.0+(cdexp(dcmplx((0.0,-1.0))*dcmplx(delta(v)*t2))
            &*cdexp(dcmplx((0.0,1.0))
            &*dcmplx((pi_wn/(2*ryd))*t2)))*trans_int(v)
            pop1(v)=cdabs(a(v))**2
            write(1,62) v,pop1(v)
62          format (i2,',',f14.8)
      end do
end do
end
!---------------------------------------------------------------------
!subroutine to calculate the minimum in the population for the
!central state - THE MAIN ANSWER!
!---------------------------------------------------------------------
subroutine population_min (pi_wn, tcl, xtcl)
implicit double precision (a-h, o-z)
parameter c=2.99792458002d10,pi=3.141592654,ryd=109737.32,&
&au_convert=2.4189e-5
!WE NEED TO FIND THE VALUE OF n THAT CORRESPONDS TO THE FRACTION OF !TCL THAT
WE USE
```

```
pi_au=pi_wn/(2*ryd)
t_2=(tcl*xtcl)/au_convert
n=(pi_au*t_2)/pi
pop_min=(n+1)-((t_2*pi_au)/pi)
pop_max=pop_min+1
open(1,file='max_pop.txt')
write(1,70) xtcl, pop_min
70 format('FOR THE POINT OF MINIMUM POPULATION, LAUNCH THE SECOND& PULSE AT TCL
TIMES', f4.2,//,'WITH AN ADDED PHASE OF',f8.6,'times the& optical cylce',//,)
end subroutine
```

(c) Fortran 77 code for calculation of the energy levels in Na and relevant transition energies and corresponding oscillator strengths. Additional subroutines calculate the autocorrelation function for electron wave packets, and the population distribution of the *s* and *d* states within the wave packet (chapter 5).

```
!-----------------------------------------------------------------------
!Program to calculate energy levels, wp dynamics and populations in Na
!-----------------------------------------------------------------------
program na
implicit double precision (a-h, o-z)
dimension s_en(1000),d_en(1000),s_trans(1000),d_trans(1000),
en(2,1000),trans(2,1000)
!READ IN DATA
open (1,file='input.txt')
read(1,*)n_av,wint,fwhm_t,nmin,nmax,nstep,tmin,tmax,tstep,wip,ryd,qds,qdd,xtcl,
xpi
!OPEN OUTPUT FILES
open(2,file='comments.txt')
open(3,file='senergy_output.dat')
open(7,file='denergy_output.dat')
open(4,file='wp_output.csv')
open(9,file='population_output.csv')
!CALCULATE FWHM OF PULSE
fwhm=((8065.465*0.441)/(241.79659*fwhm_t))
!subroutines
call energies(n_av,wip,wint,ryd,qds,qdd,fwhm_t,tcl,tpi,fwhm,xtcl,xpi,
&nmin,nmax,nstep,s_en,d_en,s_trans,d_trans,en,trans,av_en)
call wavepackets(tmin,tmax,tstep,s_trans,s_en,d_trans,d_en,tcl,xtcl,
&xpi,tpi,nmin,nmax,nstep)
call populations(tcl,xtcl,xpi,ryd,tpi,av_en,wint,nmin,nmax,nstep,en, &trans)
end
!-----------------------------------------------------------------------
!Subroutine to calculate energy of the s & d states relative to the
intermediate & corresponding oscillator strengths.The transition intensity is
then calculated and outputted, with the energies to 's_energy' and 'd_energy'
!-----------------------------------------------------------------------
subroutine energies(n_av,wip,wint,ryd,qds,qdd,fwhm_t,tcl,tpi,fwhm,
&xtcl,xpi,nmin,nmax,nstep,s_en,d_en,s_trans,d_trans,en,trans,av_en)
implicit double precision (a-h, o-z)
dimension s_en(1000),d_en(1000),s_intens(1000),d_intens(1000), &os(1000),
od(1000),s_trans(1000),d_trans(1000),en(2,1000), &trans(2,1000)
parameter c=2.99792458002e10,pi=3.141592654
!CALCULATE TCL, PI IN PS, REVIVAL TIME AND ENERGIES
tcl=2*pi*(n_av**3)*2.4188843d-5
av_en=wip-wint-(ryd/(n_av**2))
tpi=(1.0d12)/(2*c*av_en)
t_rev=(n_av*tcl)/3
!CALCULATE ADDITIONAL PHASE TERMS
au=0.5d0/109737.31568525d0
xn=dfloat(n_av)
omega=(wip-wint-Ryd/xn**2)*au
phasen=omega*xtcl*xn**3
print*,'actual phase',phasen
addphs=2.0d0*(idnint(phasen)-phasen)
```

```
print*,'additional phase',addphs
xpi=xpi+addphs
!OUTPUT TO COMMENTS
write(2,20)tcl,n_av,av_en,((1/av_en)*1e7),t_rev,(t_rev/2),xtcl,
(tcl*xtcl),xpi,fwhm_t,fwhm
20 format('tcl =',f8.4,' ps',//,
&'n = ',I2,' -->',f12.5,' cm-1 (',f7.3,' nm)',//,
&'T_rev =',f12.8,' ps',/,'so Trev/2 =',f12.8,' ps',//,
&'the delay before the 2nd pulse is',f5.2,' times tcl',/,
&'therefore t2 = ', f10.8,' ps',//,
&'the phase shift is',f6.2,' pi',//,
&'the pulse is ',f4.2,' ps with a fwhm of',f8.4,' cm-1')
!CALCULATE TRANSITION ENERGIES AND OSCILLATOR STRENGTHS
write(3,30)
30 format('n,s /cm-1,trans_s,d /cm-1,trans_d')
do 99 n=nmin,nmax,nstep
       s_en(n)=wip-wint-(ryd/((n-qds)**2))
       os(n)=(1.0d0*s_en(n))/(n**3)
       s_intens(n)=dexp((-4*(dlog(2.0d0))*(s_en(n)-av_en)**2)
     &/(fwhm**2))
       s_trans(n)=os(n)*s_intens(n)
       d_en(n)=wip-wint-(ryd/((n-qdd)**2))
       od(n)=(2.0d0*d_en(n))/(n**3)
       d_intens(n)=dexp((-4.0*dlog(2.0d0)*(d_en(n)-av_en)**2)
     &/(fwhm**2))
       d_trans(n)=od(n)*d_intens(n)
       write(3,*)s_en(n),s_trans(n)
       write(7,*)d_en(n),d_trans(n)
99 continue
close (3)
close (7)
open(3,file='senergy_output.dat')
open(7,file='denergy_output.dat')
do n=nmin,nmax,nstep
       read(3,*) en(1,n),trans(1,n)
       read(7,*) en(2,n),trans(2,n)
end do
end
!---------------------------------------------------------------------
!Subroutine to calculate wavepacket dynamics.
!The 1st wp is allowed to orbit for a time (units of tcl) before
!a 2nd wp is excited.
!The s and d wps and the wp sum are outputted to 'wp_output.csv'.
!---------------------------------------------------------------------
subroutine wavepackets (tmin,tmax,tstep,s_trans,s_en,d_trans,d_en,
&tcl,xtcl,xpi,tpi,nmin,nmax,nstep)
implicit double precision (a-h,o-z)
dimension s_en(1000),d_en(1000),s_trans(1000),d_trans(1000)
complex*16 sums, sumd
parameter c=2.99792458002e10,pi=3.141592654
write (4,40)
40 format ('t,wp_sd,wp_s,wp_d,sum_sd,,sums,,sumd')
write (4,41)
41 format (',,,,real,im,real,im,real,im')
!TIME LOOP FOR WAVE PACKETS
do 98 t=tmin,tmax,tstep
sums=dcmplx(0.0,0.0)
sumd=dcmplx(0.0,0.0)
       do 97 n=nmin,nmax,nstep
       sums=sums+dcmplx(s_trans(n),0)*(cdexp(dcmplx(0.0,-1.0)*
     &dcmplx(s_en(n)*t*2*c*pi*1d-12,0.0))+
     &cdexp(dcmplx(0.0,-1.0)*dcmplx(s_en(n)*(t+(tcl*xtcl)+
     &(xpi*tpi))*2*c*pi*1d-12,0.0)))
       sumd=sumd+dcmplx(d_trans(n),0)*(cdexp(dcmplx(0.0,-1.0)*
     &dcmplx(d_en(n)*t*2*c*pi*1d-12,0.0))+
     &cdexp(dcmplx(0.0,-1.0)*dcmplx(d_en(n)*(t+(tcl*xtcl)+
     &(xpi*tpi))*2*c*pi*1d-12,0.0)))
```

```
97      continue
        wp_sd=(cdabs(sums+sumd))
        wp_s=(cdabs(sums))
        wp_d=(cdabs(sumd))
        write (4,42) t,wp_sd,wp_s,wp_d,
     &real(sums+sumd),aimag(sums+sumd),
     &real(sums),aimag(sums),
     &real(sumd),aimag(sumd)
42      format(f14.10,',',e15.10,',',e15.10,',',e15.10,',',f15.7,
     &',',f15.7,',',f15.7,',',f15.7,',',f15.7,',',f15.10)
98      continue
end
!---------------------------------------------------------------------
!Subroutine to calculate the population of s and d states depending
!on the phase introduced to the wavepackets.
!phi=phase in units of pi,wL=av_en(a.u.),t2=total phase diff,
!Td=t2(a.u.), wg=wint(a.u.),wn=en(a.u.),an is the amplitude
!---------------------------------------------------------------------
subroutine populations(tcl,xtcl,xpi,ryd,tpi,av_en,wint,nmin,nmax,
&nstep,en,trans)
implicit double precision (a-h,o-z)
dimension en(2,1000),trans(2,1000),delta(2,1000),pop(2,1000)
&,wn(2,1000)
complex*16 an(2,1000)
c=2.99792458002d10
rydH=109737.31568525d0
write(9,60) xpi,xpi
60 format ('n-qd',',',f5.2,1x,'s',',','n',',',f5.2,1x,'d')
phi=(1.0d12/(2.0*c*(av_en)))*xpi
wL=av_en/(2*rydH)
t2=(xtcl*tcl)+phi
Td=t2/2.4188843d-5
wg=wint/(2*rydH)
do 96 i=1,2
      do 97 n=nmin,nmax,nstep
            an(i,n)=0.0d0
            pop(i,n)=0.0d0
            wn(i,n)=en(i,n)/(2*rydH)
            delta(i,n)=wL-wn(i,n)
            an(i,n)=dcmplx((0.0,-1.0))
     & *(1.0+(cdexp(dcmplx((0.0,-1.0))*dcmplx(delta(i,n)*Td))
     & *cdexp(dcmplx((0.0,1.0))*dcmplx(wL*Td))))
     &      *dsqrt(trans(i,n))
            pop(i,n)=(cdabs(an(i,n)))**2
97      continue
96 continue
do n=nmin,nmax,nstep
      write(9,90) (n-1.35),pop(1,n),n,pop(2,n)
90      format(f6.3,',',f14.8,',',i2,',',f14.8)
end do
end
```

APPENDIX 2

Derivation of equation (2.9)

Time-dependent perturbation theory in a weak field

The wavefunction is given by:

$$\Psi(r,t) = a_m(t)\psi_m(t)e^{-i\omega_m t} + a_n(t)\psi_n(t)e^{-i\omega_n t} \tag{A2.1}$$

and the Hamiltonian, H, is

$$H = H_0 + H'(t) \tag{A2.2}$$

The perturbation is a periodic function of time:

$$V = eE(t)z \text{ where } E(t) = E_0\cos(\omega t)$$
$$\therefore \quad H' = eE(t)z \tag{A2.3}$$

If the perturbation is applied to (A2.1), $\Psi(r,t) \Rightarrow (H_0 + H')\Psi(r,t) = H\Psi$,

$$\begin{aligned}\therefore (H_0 + H')\Psi(r,t) = {} & H_0 a_m(t)\psi_m(t)e^{-i\omega_m t} + H_0 a_n(t)\psi_n(t)e^{-i\omega_n t} \\ & + H'a_m(t)\psi_m(t)e^{-i\omega_m t} + H'a_n(t)\psi_n(t)e^{-i\omega_n t}\end{aligned} \tag{A2.4}$$

If $H\Psi = E\Psi$,

$$\begin{aligned}E\psi = {} & E_m a_m(t)\psi_m(t)e^{-i\omega_m t} + E_n a_n(t)\psi_n(t)e^{-i\omega_n t} \\ & + H'a_m(t)\psi_m(t)e^{-i\omega_m t} + H'a_n(t)\psi_n(t)e^{-i\omega_n t}\end{aligned} \tag{A2.5}$$

The general solution to time-dependent Schrödinger equation is given by $i\hbar\dfrac{\partial\Psi}{\partial t} = H\Psi$. Therefore, the left hand side of (A2.5) can be written as

$$\therefore i\hbar\frac{\partial}{\partial t}\left(a_m(t)\psi_m(t)e^{-i\omega_m t}+a_n(t)\psi_n(t)e^{-i\omega_n t}\right)=H\Psi$$
$$=i\hbar\left(\dot{a}_m(t)\psi_m(t)e^{-i\omega_m t}-a_m i\omega_m\psi_m(t)e^{-i\omega_m t}+\dot{a}_n(t)\psi_n(t)e^{-i\omega_n t}-a_n i\omega_n\psi_m(t)e^{-i\omega_g t}\right) \quad \text{(A2.6)}$$

To find coefficients a_n, multiply by complex conjugate $\psi_n(t)e^{i\omega_n t}$ and integrate over all space. Dropping the *(t)* from *a(t)* and $\psi(t)$ and applying the orthogonality conditions $\int_0^\infty \psi_n^*\psi_n d\tau = 1$ and $\int_0^\infty \psi_n^*\psi_m d\tau = 0$, (A2.5) becomes

$$=\int_0^\infty \psi_n(t)e^{i\omega_n t}\left(E_m a_m\psi_m e^{-i\omega_m t}+E_n a_n\psi_n e^{-i\omega_n t}+H'a_m\psi_m e^{-i\omega_m t}+H'a_n\psi_n e^{-i\omega_n t}\right)$$
$$=E_m a_m\int_0^\infty \psi_n\psi_m e^{i(\omega_n-\omega_m)t}dt+E_n a_n\int_0^\infty \psi_n\psi_n dt+a_m\int_0^\infty \psi_n H'\psi_m e^{i(\omega_n-\omega_m)t}+a_n\int_0^\infty \psi_n H'\psi_n dt$$
$$=0+E_n a_n+a_m\langle n|H'|m\rangle e^{i(\omega_n-\omega_m)t}+a_n\langle n|H'|n\rangle \quad \text{(A2.7)}$$

If it is assumed that the perturbation has no diagonal matrix elements, i.e. $\langle n|H'|n\rangle = 0$, (A2.7) can be reduced to

$$=E_n a_n+eE(t)a_m\langle n|z|m\rangle e^{i(\omega_n-\omega_m)t} \quad \text{(A2.8)}$$

Applying the same procedures to the right hand side of (A2.6) results in

$$i\hbar\int_0^\infty \psi_n(t)e^{i\omega_n t}\left(\dot{a}_m(t)\psi_m(t)e^{-i\omega_m t}-a_m i\omega_m\psi_m(t)e^{-i\omega_m t}+\dot{a}_n(t)\psi_n(t)e^{-i\omega_n t}-a_n i\omega_n\psi_m(t)e^{-i\omega_g t}\right)$$
$$=i\hbar\dot{a}_n+a_n\omega_n\hbar$$
$$=i\hbar\dot{a}_n+E_n a_n \quad \text{(A2.9)}$$

Equate (A2.8) and (A2.9) to give

$$E_n a_n+eE(t)a_m\langle n|z|m\rangle e^{i(\omega_n-\omega_m)t}=i\hbar\dot{a}_n+E_n a_n$$
$$\therefore \dot{a}_n=(i\hbar)^{-1}eE(t)\langle n|z|m\rangle e^{i(\omega_n-\omega_m)t}a_m \quad \text{(A2.10)}$$

If $E(t) = E_0 \cos(\omega t) f(t)$ and $\Omega_n = \dfrac{eE_0 \langle n|z|m\rangle}{\hbar}$,

$$\therefore \dot{a}_n = (i\hbar)^{-1} eE_0 \cos(\omega t) f(t) \langle n|z|m\rangle e^{i(\omega_n - \omega_m)t} a_m \tag{A2.11}$$

$$\Rightarrow \dot{a}_n = (i)^{-1} \Omega_n \cos(\omega t) e^{i(\omega_n - \omega_m)t} f(t) a_m \tag{A2.12}$$

Substitute $\cos(\omega t) = \dfrac{1}{2}\left(e^{i\omega t} + e^{-i\omega t}\right)$

$$\begin{aligned} \Rightarrow \dot{a}_n &= -\frac{i}{2}\Omega_n f(t)\left(e^{i\omega t + i(\omega_n - \omega_m)t} + e^{-i\omega t + i(\omega_n - \omega_m)t}\right) a_m \\ &= -\frac{i}{2}\Omega_n f(t)\left(e^{i(\omega + \omega_n - \omega_m)t} + e^{i(-\omega + \omega_n - \omega_m)t}\right) a_m \end{aligned} \tag{A2.13}$$

Let $\Delta_n = \omega_n - \omega_m - \omega$ and assume the RWA i.e. $e^{\pm i(\omega + \omega_n - \omega_m)t} \approx 0$. Also, this is a weak field approach so $a_m(t) = 1$.

$$\Rightarrow \dot{a}_n(t) = -\frac{i}{2}\Omega_n f(t) e^{i\Delta_n t} a_m(t) \tag{A2.14}$$

This is equation (2.9).

APPENDIX 3

Integration of equation (2.11)

The following derivation shows how the integration of eq. (2.11) follows from the definition of the Fourier transform of a Gaussian function.

Taken from reference [1], the Gaussian distribution in the normalised form can be written as

$$f(t) = \frac{1}{(2\pi)^{1/2}} \frac{1}{\tau} \exp\left(-\frac{t^2}{2\tau^2}\right), \qquad -\infty < t < \infty \tag{A3.1}$$

where $\tau = \Delta t$. To find its Fourier transform, the following is evaluated:

$$\begin{aligned} g(\omega) &= (2\pi\tau)^{-1} \int_{-\infty}^{\infty} \exp\left(-t^2/2\tau^2\right) \exp(-i\omega t)\, dt \\ &= (2\pi\tau)^{-1} \int_{-\infty}^{\infty} \exp\left\{-\frac{1}{2\tau^2}\left[t^2 + 2\tau^2 i\omega t + \left(\tau^2 i\omega\right)^2 - \left(\tau^2 i\omega\right)^2\right]\right\} dt \end{aligned} \tag{A3.2}$$

In (A3.2) the quantity $-\left(\tau^2 i\omega\right)^2/2\tau^2$ has been added and subtracted in the exponent in order to complete the square. Bringing the final *t*-dependent factor outside the integral gives:

$$g(\omega) = \frac{\exp\left(-\tau^2 \omega^2/2\right)}{(2\pi)^{1/2}} \frac{1}{(2\pi)^{1/2}\tau} \int_{-\infty}^{\infty} \exp\left[-\frac{\left(t + i\tau^2\omega\right)^2}{2\tau^2}\right] dt \tag{A3.3}$$

The last factor in (A3.3) is the normalisation integral for the Gaussian distribution and equals unity [1].

Therefore the result is

$$g(\omega)=\frac{1}{(2\pi)^{1/2}}\exp\left(-\frac{\tau^2\omega^2}{2}\right) \tag{A3.4}$$

Eq. (2.9) is given as

$$\dot{a}_n=-\frac{i}{2}\Omega_n\exp\left(-2\ln 2\left(t/\tau^p\right)^2\right)e^{i\Delta_n t} \tag{A3.5}$$

The aim is to express (A3.5) in the same form as (A3.2). Therefore, neglecting the normalisation factors,

$$\begin{aligned}\dot{a}_n &= \int_{-\infty}^{\infty}\exp\left(-2\ln 2\left(t/\tau_p\right)^2\right)\exp(i\Delta_n t)\\ &\equiv \int_{-\infty}^{\infty}\exp\left(-t^2/2\tau^2\right)\exp(-i\omega t)\mathrm{d}t\end{aligned} \tag{A3.6}$$

where

$$2\ln 2\left(\frac{t^2}{\tau_p{}^2}\right)=\frac{t^2}{2\tau^2}\Rightarrow\tau^2=\frac{\tau_p{}^2}{4\ln 2}\quad\text{and}\quad\Delta_n=-\omega, \tag{A3.7}$$

By substitution, the Fourier transform of (A3.5) can be written as

$$g(\omega)=\exp\left(-\frac{\tau^2\omega^2}{2}\right)\equiv\exp\left(-\frac{\Delta_n{}^2\tau_p{}^2}{8\ln 2}\right) \tag{A3.8}$$

Therefore, the integral of $\dot{a}_n$, equation 2.11, can be written as:

$$a_n(t)=-\frac{i}{2}\Omega_n e^{-\frac{(\Delta_n\tau_p)^2}{8\ln 2}}=-\frac{i}{2}\Omega_n g(\omega) \tag{A3.9}$$

APPENDIX 4

Derivation of equations (2.17) and (2.18)

A wave packet can be expressed as the sum of the individual energy eigenfunctions $\psi_n(x)$, with corresponding eigenvalues E_n, weighted by the laser pulse profile and transition probabilities, given by a_n:

$$\Psi(x,t) = \sum_{n=0}^{\infty} a_n \psi_n(x) e^{-iE_n t/\hbar} \tag{A4.1}$$

If the energy in the exponential is expanded around $\bar{n}$, letting $E_n = \hbar\omega$ where $\omega = 2\pi/T_{cl}$ gives

$$E_n = E_{\bar{n}} + \hbar\omega(n-\bar{n}) + \frac{\hbar^2}{2}\frac{\partial\omega}{\partial E_n}(n-\bar{n})^2\omega + \ldots, \tag{A4.2}$$

Neglecting the first term and substituting back into the exponential:

$$\begin{aligned} \exp\left(\frac{-iE_n t}{\hbar}\right) &= \exp\left[\frac{-it}{\hbar}\left(\hbar\frac{2\pi}{T_{cl}}(n-\bar{n}) + \frac{\hbar^2}{2}\frac{2\pi}{T_{cl}}(n-\bar{n})^2\frac{\partial\omega}{\partial E_n}\right)\right] \\ &= \exp\left[-2\pi i\left(\frac{kt}{T_{cl}} + \frac{\hbar k^2 t}{2T_{cl}}\frac{\partial\omega}{\partial E_n}\right)\right] \end{aligned} \tag{A4.3}$$

where $k = (n-\bar{n})$. The second term (A3.3) can be further simplified by letting

$$T_{rev} = \frac{2T_{cl}}{\hbar\left(\frac{\partial\omega}{\partial E_n}\right)} \tag{A4.4}$$

$$\therefore \exp(-iE_n t/\hbar) = \exp\left[-2\pi i\left(\frac{kt}{T_{cl}} + \frac{k^2 t}{T_{rev}}\right)\right] \tag{A4.5}$$

The forms of T_{cl} and T_{rev} in equation (2.18) are rearrangements of those above.

$$T_{cl} = \frac{2\pi\hbar}{E'(\bar{n})} = \frac{2\pi\hbar}{\hbar\omega} = \frac{2\pi}{\omega} \tag{A4.6}$$

and

$$T_{rev} = \frac{2\pi\hbar}{E''(\bar{n})} = \frac{2\pi\hbar}{\frac{\hbar}{2}\left(\frac{\partial\omega}{\partial E_n}\right)\omega} = \frac{2T_{cl}}{\hbar\left(\frac{\partial\omega}{\partial E_n}\right)} \tag{A4.7}$$

APPENDIX 5

Expansion of the E_n around $\bar{n}$ for Rydberg states in a wave packet

(reproduced in part from reference [2])

A quantitative description of revivals and partial revivals can be obtained by expanding the energy E_n in the in the exponential factor of the stationary wavefunction ψ_n around the average energy $E_{\bar{n}}$. A Taylor-series expansion results in the following expression fro the energy

$$E_n = -\frac{1}{2n^2} = -\frac{1}{2(\bar{n}-\delta n)^2}$$
$$= -\frac{1}{2\bar{n}^2}\left[1-2\left(\frac{\delta n}{\bar{n}}\right)+3\left(\frac{\delta n}{\bar{n}}\right)^2-4\left(\frac{\delta n}{\bar{n}}\right)^3+\ldots\right] \qquad \text{(A5.1)}$$

where $\delta n = n - \bar{n}$ and $\delta n \langle\langle \bar{n}$. The effect of the first three orders in (A5.1) on the position of the energy levels is illustrated in figure A1.

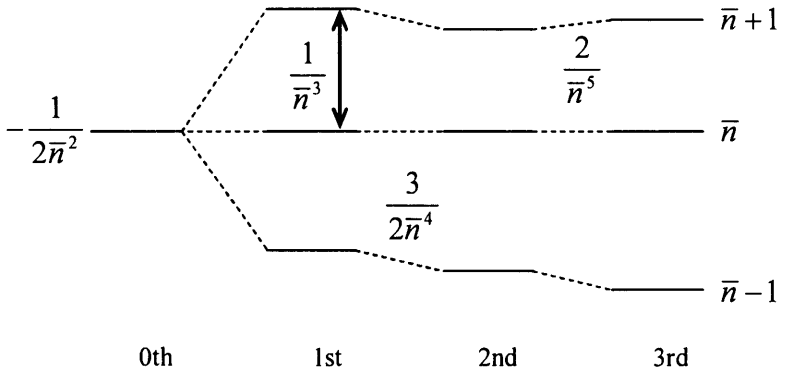

Figure A1 The effect on the energy levels of consecutive terms in the series expansion of the energy E_n around $\bar{n}$.The second order term removes the symmetry of the harmonic level spacing after the linear term. The third term introduces asymmetry into the revival pattern.

The first term within the brackets gives the total energy of the wave packet. The term linear in δn gives the harmonic energy level spacing $\Delta E = 1/\bar{n}^3$, resulting in dispersion-free motion with a classical period $T_{cl} = 2\pi\bar{n}^3$ (in atomic units). The non-linearity introduced by the term quadratic in δn shift all the energy levels in the same direction and removes the levels from being equidistant. This term is responsible for the spreading of the wave packet and accounts for the revivals and partial revivals. The revival time T_{rev} of the wave packet given by the first order dispersion is

$$T_2 = 2T_{rev} = \frac{4}{3}\pi\bar{n}^4 = \frac{2}{3}\bar{n}T_{cl} \qquad \text{(A5.2)}$$

Where T_2 is the revival time as defined by Averbukh and Perelman [3]. At T_{rev} the wave packet rephrases for the first time at the outer turning point of motion, whilst at T_2 the wave packet rephases for the second time, in this case at the inner turning point.

REFERENCES

1. K. F. Riley, *Mathematical Methods for the Physical Sciences*. Cambridge University Press, 1974.
2. J. Wals, H. H. Fielding, and H. B. V. Vandenheuvell, *Phys. Scr.* **T58**, 62 (1995).
3. I. S. Averbukh and N. F. Perelman, *Phys. Lett. A* **139** (9), 449 (1989).